Bridging length and time scales of plate motions and great earthquakes

Thesis by
Jiaqi Fang

In Partial Fulfillment of the Requirements for the
Degree of
Doctor of Philosophy

CALIFORNIA INSTITUTE OF TECHNOLOGY
Pasadena, California

2026
Defended April 28, 2026

© 2026

Jiaqi Fang
ORCID: 0000-0001-6369-4802

All rights reserved except where otherwise noted

ACKNOWLEDGEMENTS

I am deeply grateful for the opportunity to pursue my PhD at the Caltech Seismo Lab. This journey has been very meaningful and has shaped who I am today.

I would like to begin by expressing my sincere gratitude to my advisor, Mike, for his patience, guidance and support. His insight and dedication to science have guided and inspired me throughout this journey. I am also grateful to Nadia for her invaluable advice and thoughtful feedback, which has greatly enriched this work. Special thanks to Zhongwen for his generous support when I worked with him and understanding when my focus moved back to geodynamics. I would like to thank Jennifer for her time and service on my thesis committee and her helpful suggestions. I also wish to acknowledge Rob, Joann, Allen, Jean-Philippe, Zach, Mark, from whom I have learned a lot about the breadth and diversity of geophysical research. I am thankful to the Seismo Lab staff, particularly Donna, Kim, Priscilla, Ruth, Chelsea, for making everything related to travel and equipment easy for me.

Many thanks to my collaborators, Max, Johann, Georg and Rishav for their contributions and shared efforts that made this work possible. Particularly, I appreciate Max's dedication in implementing the code that underpins much of this research. Their expertise and perspectives have substantially strengthened both the depth and breadth of this work.

I feel fortunate to have met so many wonderful people at the Seismo Lab. I am especially grateful to Yida, who taught me so much in both life and research and made my transition at the beginning of my PhD remarkably smooth. I would like to thank my office mates: Eli, Auden, Qian, Linxuan, Erin; my cohort: Alex, Jack, Cijin; as well as other group members and friends at the Seismo Lab: Wei, Chenxi, Qian, Ojashvi, Leonid, Mo, Anna, Zhe, Zhichao, Ethan, Yan, Jimmy, Ettore, Weiqiang, Jiaxuan, Jiuxun, Han, Shun, Xiaozhuo, Qiushi, Caifeng, Valeria, Taiyi, Kai, Ben, Rajani and many others. I have benefited so much from interacting with them, and I regret I cannot name everyone here. The shared moments have made this journey productive and enjoyable.

My friends outside the Seismo Lab have also been an essential source of support. I would especially like to thank Zhouxing, Daoji, Kexin, Liangliang, Zhaowen, Zizhen, Yanshen, and Shihao for their support when I began my PhD remotely from Beijing. I also want to thank Hongkai, Yiheng, and Sihe, with whom I shared many

memorable days and nights in Pasadena.

My appreciation also extends to my previous advisors, Dr. Rhodri Davies and Dr. Wei Tian, who introduced me to geophysics and laid the foundation for my research.

I would like to thank Meichen for her companionship and encouragement through joyful and challenging times. Her belief in me has been a constant source of strength and motivation.

Finally, I would like to thank my parents for their unconditional love and unwavering support, which have meant more to me than words can express.

The past five and a half years have passed quickly, leaving me with countless cherished memories and so many people and moments to be grateful for. It is impossible to list them all in a few short paragraphs. I hope to carry this warmth forward, and pass it on to more places and to more people.

ABSTRACT

Tectonic plates move at a steady velocity of several centimeters per year, which is intermittently interrupted by great megathrust earthquakes with rapid slip up to tens of meters. These large rupture events are driven by the slow tectonic loading and can substantially alter the deformation rate and state of stress in adjacent regions. With advances in computational algorithms, we develop cross-scale finite-element models that self-consistently integrate long-term motion of entire plates and the intervening space-time evolution associated with great earthquakes. The objectives are two-fold: firstly, to gain insight into the occurrence and magnitude of great earthquakes and their relationship with large-scale tectonic processes, and secondly, to constrain rheological properties of the solid Earth with multi-scale geophysical observations.

We begin with formulating a generic subduction model that simultaneously resolves the dynamics of plate motions and megathrust seismic cycles (Chapter 2). Driven by internal buoyancy forces and governed by a nonlinear visco-elasto-plastic rheology, the predicted plate convergence and seismic cycle behavior align with observations in subduction zones. Using an efficient 2.5-dimensional approach, we show that the along-strike resistance arising from slip variations plays a key role in modulating the earthquake magnitude. In Chapter 3, the model is used to systematically investigate the influence of rupture dimensions, rheological properties and subduction characteristics on plate velocities and coseismic slip. The results provide a physical framework for understanding observed earthquake scaling relationships. In Chapter 4, we build a three-dimensional model tailored to the Chilean Subduction Zone, and reproduce both the long-term motion of the Nazca Plate and post-seismic deformation in the adjacent non-ruptured segment after the 2010 Maule earthquake (M_w = 8.8). Combining these multi-scale geodetic observations as constraints significantly improves the uniqueness of inferred mantle viscosity structure. Building on the previous work, we implement advanced computational models of plate motions and earthquakes using the highly scalable finite-element code *Rhea* (Chapter 5). The first model reproduce plate kinematics on a global scale while resolving great earthquakes at plate boundaries at a high resolution. The model adopts rheological properties derived from laboratory experiments and is constrained by both background plate motions and transient earthquake-related deformations. The second model incorporates a true free surface and enables direct coupling between plate

motions, surface topography and off-megathrust stress state to Earth's nonlinear rheology within a unified cross-scale model. Our work demonstrates the potential for assimilating multi-scale geophysical observations in unified, physics-based models to better characterize Earth's internal structure and assess seismic hazards.

PUBLISHED CONTENT AND CONTRIBUTIONS

Fang, Jiaqi, Michael Gurnis, and Rishav Mallick (2025). "Constraints on nonlinear mantle rheology from multi-scale geodetic observations of plate motion and post-seismic enhanced landward motion". In: *Earth and Planetary Science Letters* 669, p. 119566. DOI: 10.1016/j.epsl.2025.119566.
J.F. participated in the conception of the project, performed the computations, analyzed the data, and participated in the writing of the manuscript.

Fang, Jiaqi, Michael Gurnis, and Nadia Lapusta (2024). "Dynamic emergence of plate motions and great megathrust earthquakes across length and time scales". In: *Geophysical Research Letters* 51.22, e2024GL110821. DOI: 10.1029/2024GL110821.
J.F. participated in the conception of the project, performed the computations, analyzed the data, and participated in the writing of the manuscript.

TABLE OF CONTENTS

Acknowledgements . . . iii
Abstract . . . v
Published Content and Contributions . . . vii
Table of Contents . . . vii
List of Illustrations . . . ix
List of Tables . . . xvii
Chapter I: Introduction . . . 1
Chapter II: Dynamic emergence of plate motions and great megathrust earthquakes across length and time scales . . . 8
2.1 Introduction . . . 8
2.2 Methods . . . 10
2.3 Results . . . 13
2.4 Discussion . . . 16
2.5 Conclusions . . . 19
Chapter III: Multi-scale dynamics of subduction zones: From long-term plate motions to great megathrust earthquakes . . . 34
3.1 Introduction . . . 34
3.2 Methods . . . 37
3.3 Results . . . 42
3.4 Discussion . . . 51
3.5 Conclusions . . . 55
Chapter IV: Constraints on nonlinear mantle rheology from multi-scale geodetic observations of plate motion and post-seismic enhanced landward motion 67
4.1 Introduction . . . 68
4.2 Method . . . 70
4.3 Results . . . 74
4.4 Discussion . . . 79
4.5 Conclusions . . . 83
Chapter V: Advanced computational models of plate motions and great megathrust earthquakes . . . 99
5.1 Introduction . . . 99
5.2 Governing equations and rheology . . . 101
5.3 Global model of plate motions and the Tohoku-oki earthquake . . . 102
5.4 Proof-of-concept cross-section model with a true surface . . . 105
Chapter VI: Conclusions and future outlook . . . 114

LIST OF ILLUSTRATIONS

Number *Page*

1.1 Non-net-rotation long-term plate motions calculated from NNR-MORVEL56 (Argus, Gordon, and DeMets, 2011). The orange lines indicate plate boundaries. Regions close to plate boundaries are excluded from the calculation and masked. 2

1.2 Geodetic surface velocities before (blue) and after (red) the 2010 Maule earthquake (M_w = 8.8) (Melnick et al., 2017). The teeth line indicates the location of the trench, and the beachball marks the earthquake epicenter and focal mechanism. NZ and SA denote the Nazca Plate and South American Plate, respectively. 3

2.1 (A) Thermal structure of the model (see details in Text S2). x, z and T denote the horizontal length, depth and temperature. (B) Enlargement of the thermal structure near the megathrust with shear zone (width is 6 km, $\approx 5\times$ local element size) surrounded by silver dashed lines. (C) The temperature-dependent frictional parameters, μ_{st} and μ_{dyn}, in the shear zone. The top secondary axis shows the depth z corresponding to the temperature T. (D) Effective viscosity η initially for the model, from a viscously-dominated computation with a large time step size. 11

2.2 (A) The surface horizontal velocity, v_x, along a profile perpendicular to the trench at an interseismic time step (blue solid), at a coseismic time step (red solid), and averaged over the time span of 2000 years (black dashed). As the time step size is 5 years, coseismic velocities represent integrated coseismic displacements over a step of 5 years. (B) The slip velocity V at an interseismic time step (blue) and the slip U at a coseismic time step (red) in the shear zone versus the depth z. (C) The evolution of the mean slip velocity in the shear zone, V_{mean}, is depicted by the teal solid line. Each peak represents a rupture event. The cumulative displacement relative to the average plate motion, Δu_x, is plotted with magenta solid (at $x = -100$ km, on the incoming plate) and magenta dashed ($x = +100$ km, on the overriding plate) lines. (D) Space–time pattern of the relative stress change, $\Delta\tau_{II}$, in the shear zone. $\Delta\tau_{II}$ is calculated by subtracting the 2000-year mean of τ_{II} at each depth from the second invariant of the deviatoric stress τ_{II}. 15

2.3 (A) The coseismic surface displacement, u_x, along a profile perpendicular to the trench for cases with different rupture length scales $\tilde{L}$. (B) The coseismic slip U in the shear zone versus the depth z for the same cases. (C) Coseismic displacement near the trench in representative events with different values of $\tilde{L}$. Silver dashed lines show the location of the shear zone. 17

2.4 (A) The coseismic surface displacement of the incoming plate near the trench u_x and (B) the maximum coseismic slip in the shear zone U_{max} versus the rupture length scale $\tilde{L}$. The upper dashed lines represent u_x and U_{max} for a case without along-strike resistance ($\tilde{L} \to \infty$) and the respective quantity before the rupture event. 17

2.S1 Thermal structure of Model A1. 22

2.S2 Model outcomes of Model A1 (akin to Figure 2.2 in the manuscript). Symbols are the same as those in Figure 2.2. 22

2.S3 Thermal structure of Model A2. 22

2.S4 Model outcomes of Model A2 (akin to Figure 2.2 in the manuscript). Symbols are the same as those in Figure 2.2. 23

2.S5 Viscosities of Model A3. 24

2.S6 Model outcomes of Model A3 (akin to Figure 2.2 in the manuscript). Symbols are the same as those in Figure 2.2. 24

2.S7 Viscosities of Model A4. 24
2.S8 Model outcomes of Model A4 (akin to Figure 2 in the manuscript). Symbols are the same as those in Figure 2. 25
2.S9 Stress field near the megathrust after an interseismic time step. τ_{II} denotes the second invariant of the deviotoric stress tensor. Black bars indicate directions of principal compression axes. 25
2.S10 Stress field near the megathrust after a coseismic time step. τ_{II} denotes the second invariant of the deviatoric stress tensor. Black bars indicate directions of principal compression axes. 26
2.S11 Stress changes caused by a rupture event. 26
2.S12 Comparison of 2.5D models with different numbers of along-strike elements. Symbols are the same as those in Figure 2.4. 26
2.S13 Comparison of 2.5D models with different along-strike domain widths. Symbols are the same as those in Figure 2.4. 27
3.1 (a) Thermal structure of the model. The 2D model lies in the x–z plane. The 2.5D model expands the 2D domain by two elements to a thickness of 5 km. The 3D model for validation of the 2.5D approximation spans 640 km in the along-strike (y) direction, with along-strike variations neglected. (b) Enlargement of the thermal structure in the plate boundary area. (c) Friction parameters μ_s and μ_d versus depth along the megathrust shear zone. 39
3.2 (a) Comparison of coseismic slip along the megathrust shear zone in the 2.5D model and 3D models with different stress drop distributions shown in (b). (b) Along-strike distributions assumed in the 3D models. 41
3.3 (a) Interseismic velocities (blue solid), coseismic displacements (red solid), and long-term (black dashed) velocities along the surface, v_x. (b) Interseismic (blud solid) and long-term (black dashed) slip velocities, V, together with coseismic slip (red solid), U, along the megathrust. 43
3.4 Coseismic displacements near the plate boundary (a) and coseismic slip along the megathrust shear zone (b) for different along-dip rupture width (W). 44
3.5 Coseismic displacements near the plate boundary (a) and coseismic slip along the megathrust shear zone (b) for different along-strike rupture length (L). 45

3.6 The relationship between the magnitude and along-strike rupture length (L) of earthquakes. Each line assumes a fixed along-dip rupture width (W), and the dashed segments indicate less realistic cases in which $L < W$. Gray dots with error bars are estimates for large megathrust events, compiled by Thingbaijam, Mai, and Goda (2017). 46

3.7 Maximum coseismic slip, U_{max}, and estimated recurrence interval, T_r, versus long-term convergence rate, v_{pl}, for cases with varied rheological parameters. The circle where different lines intersect denote the reference case, and each line shows results when one single parameter is perturbed. Squares indicate results for smaller parameter values, and triangles indicate results for larger parameter values. The dot with error bars represents results from the SE model. 47

3.8 (a) Viscosity profile, (b) long-term horizontal velocitiy along the surface, and (c) coseismic slip along the megathrust shear zone when ω_{disl} is varied. Note that the viscosity is in log scale while the surface velocity is in linear scale. 48

3.9 (a) Second invariant of the deviatoric stress along the megathrust shear zone, (b) long-term horizontal velocitiy along the surface, and (c) coseismic slip along the megathrust shear zone when μ_s is perturbed. 49

3.10 Long-term velocity of the incoming plate (blue) and maximum coseismic slip (red) for cases with different seismogenic zone dip angles (a) or different incoming plate ages. 50

3.11 The relationship between the maximum earthquake magnitude that a subduction zone segment can host and (a) the dip angle or (b) the along-dip width of the seismogenic zone. Each line assumes a fixed along-strike rupture length (L). Gray dots with error bars are data for segments along major convergent plate boundaries, compiled by Lallemand and Heuret (2017). 51

3.S1 Coseismic horizontal displacements along the surface, u_x, predicted by the IE model (red solid), SE model (orange dashed), and Okada solution (purple dotted) Okada, 1985. 59

3.S2 (a) Long-term horizontal velocitiy along the surface and (b) coseismic slip along the megathrust shear zone when $\tau_{y,b}$ is varied. 60

3.S3 (a) Long-term horizontal velocitiy along the surface and (b) coseismic slip along the megathrust shear zone when G_b is varied. 60

3.S4 (a) Long-term horizontal velocitiy along the surface and (b) coseismic slip along the megathrust shear zone when G_{sz} is varied. 61
3.S5 (a) Long-term horizontal velocitiy along the surface and (b) coseismic slip along the megathrust shear zone when $\mu_{d,mid}$ is varied. 61
4.1 A map of the Chilean subduction zone with two types of geodetic observations: the long-time motion of the Nazca Plate and the enhanced landward motion (ELM) in the adjacent segment after the 2010 Maule earthquake. Purple arrows in the zoom-in plot show differences between the post-seismic and pre-seismic GNSS velocities, measured by Melnick et al., 2017. NZ and SA refer to the Nazca Plate (incoming) and South America Plate (overriding), respectively. 70
4.2 (a) Model setup with the temperature field. The model domain is 7580 km (x) × 2000 km (y) × 800 km (z). The white dashed line shows the location of the trench (x = 0 km and z = 0 km), and the focal mechanism shows the location of the earthquake epicenter (in the plane y = 0 km). (b) The imposed co-seismic friction change in the megathrust shear zone. The horizontal axis is the along-strike distance, and the vertical axis is the vertical depth. (c) Vertical viscosity profiles at the rupture center, averaged over x = 0–500 km at the pre-seismic stage. With a smaller weak factor ω (and a larger activation volume V), the viscosity η decreases at shallow depth and increases at deep depth. (d) The surface horizontal velocity v_x along a trench-perpendicular profile at the rupture center (y = 0 km), from the long-timescale computation (black dashed line) at the pre-seismic stage (blue solid line). The co-seismic displacements u_x along the same profile are shown in the red solid line. The velocities and co-seismic displacements are for ω = 1 but are similar for other cases with different mantle viscosity profiles (Fig. 4.S3). 72
4.3 Viscosity profiles in different regions of the incoming plate for ω = 1: (a) Averaged over x = [-2500, -2000] km, y = 0 km, within the ruptured segment and far from the trench; (b) x = [-500, 0] km, y = 0 km, within the ruptured segment and near the trench; (c) x = [-500, 0] km, y = 500 km, within the non-ruptured segment and near the trench. 76

4.4 Map view of post-seismic surface velocity changes for cases with different mantle viscosity profiles. The post-seismic velocities are averaged over 5 years following the earthquake. Velocity changes in the near-field section ($y \leq 400$ km) and the far-field section ($y > 400$ km) are plotted with different scales. 77

4.5 (a) Predicted horizontal velocity changes along trench-parallel profiles for computations with different mantle viscosity profiles (solid lines) and observed ELM at local GNSS stations (dots with error bars) during the 5-year post-seismic period. (b) The average ELM in the y = 500–700 km section measured by Melnick et al., 2017 (dotted purple) and predicted by different computations (solid purple), and the minimum viscosity in the asthenosphere pre-seismically (solid orange) and post-seismically (dashed orange). (c, d) Results from computations with a smaller earthquake. (e, f) Results for computations without the lateral spatial variation in shear modulus. 79

4.S1 Thermal structure zoomed in near the megathrust. 85

4.S2 Shear modulus structure used in the reference model in the section with x = [-1000, 1000] km. Outside this region, the shear modulus is 60 GPa in the upper mantle and 120 GPa in the lower mantle. 86

4.S3 Co-seismic stress changes in the megathrust shear zone. The horizontal axis is the along-strike distance, and the vertical axis is the vertical depth. 86

4.S4 For different weakness factors ω, the surface horizontal velocity v_x along a trench-perpendicular profile at the rupture center (y = 0 km), from the long-timescale computation (black dashed line) at the pre-seismic stage (blue solid line), and the co-seismic displacements u_x along the same profile are shown in the red solid line, akin to Fig. 4.2d. 87

4.S5 Computations with different pairs of the weakness factor ω and the activation volume V that can produce similar enhanced landward motion (ELM) patterns: (a) The surface horizontal velocity v_x along a trench-perpendicular profile at the rupture center (y = 0 km), from the long-timescale computation, akin to the black dashed line in Fig. 4.2d; (b) Viscosity profiles averaged over x = [-500, 0] km, y = 0 km, akin to the blue solid line in Fig. 4.3b; (c) Predicted horizontal velocity changes along trench-parallel profiles (solid lines) and observed ELM at local GNSS stations (dots with error bars) during the 5-year post-seismic period, akin to Fig. 4.5a. 88

4.S6 Values of the weakness factor ω and the activation volume V required for similar ELM (red dashed) and the 7 cm/year motion of the incoming plate (blue solid). Combining both observations provides tighter constraints on the parameter space. 89

4.S7 The force balance in the adjacent segment. The post-seismic deformation in the non-ruptured segment is modulated by the horizontal push from the accelerated incoming plate, the shear force from the seaward-rebounding ruptured segment and the underlying mantle. The bottom right plot shows changes in horizontal velocities near the megathrust in the segment (y = 500–700 km) at the post-seismic stage. The incoming plate experiences substantially faster deformation and provides the dominant force that produces ELM. 90

4.S8 (a) Average post-seismic slip velocity in the megathrust shear zone at the rupture center. (b, c) Distribution of average post-seismic slip velocity in the megathrust for different rates of friction increase. The computations use $\omega = 1$ and $V = 13.4$ cm^3·mol^{-1}, and the slip velocity is measured in the first year after the earthquake. 90

4.S9 Predicted horizontal velocity changes along trench-parallel profiles with different rates of friction increase (dashed lines) and observed ELM at local GNSS stations (dots with error bars) during the 5-year post-seismic period, akin to Fig. 4.5a. The computations use ω = 1 and V = 13.4 cm^3·mol^{-1}. The results show far-field post-seismic deformation in adjacent segments where plates remain coupled is largely insensitive to the fault healing and continued slip in the rupture zone, unless the rupture zone remains substantially weakened. 91

4.S10 Predicted horizontal velocity changes along trench-parallel profiles with different computational time steps (dashed lines) and observed ELM at local GNSS stations (dots with error bars) during the 5-year post-seismic period, akin to Fig. 4.5a. The computations use $\omega = 1$ and $V = 13.4$ cm^3·mol^{-1}. The consistency between predictions for different time step sizes confirms the robustness of the model. 92

5.1 Setup of the global-scale model showing the viscosity field on cross-section through the Tohoku-oki. The inset highlights the plate boundary region resolved at a high resolution. 103

5.2 The predicted long-term plate motions (red arrows) compared with data calculated from NNR-MORVEL56 (Argus, Gordon, and DeMets, 2011). The background color represents the logarithmic weakness factors $\log_{10} \omega$ within major convergent plate boundaries. 105

5.3 Coseismic surface velocity changes (a) across the Earth and (b) near the epicenter of the Tohoku-oki earthquake. 105

5.4 Surface velocity changes (a) across the Earth and (b) near the epicenter of the Tohoku-oki earthquake during a 1-year postseismic period. 106

5.5 (a) Temperature (T) and (b) resulting viscosity (η) in the cross-section model. 106

5.6 (a) Surface velocities computed by the preliminary viscoplastic solve with a free-slip top boundary. (b) The surface topography converted from normal stresses along the free-slip top boundary. (c) Surface velocities computed by the viscoplastic solve with a free surface. . . . 108

5.7 Surface velocities (a) 1 year before the earthquake, (b) during the earthquake and (c) 1 year after the earthquake. 109

LIST OF TABLES

Number *Page*

2.S1 Model parameters. 21
3.1 Parameters of the reference model. 42
4.S1 Dislocation and diffusion creep parameters. 85
5.1 Viscosity parameters in the global model. 102
5.2 Viscosity parameters in the global model. 107

Chapter 1

INTRODUCTION

Tectonic plates move continuously across Earth's surface at velocities of several centimeters per year (Fig. 1.1) (DeMets, Gordon, and Argus, 2010; Argus, Gordon, and DeMets, 2011), driven by buoyancy forces arising from density contrasts within the lithosphere and mantle. Although these viscously dominated motions appear steady on geological timescales, they are punctuated by episodic great megathrust earthquakes that accommodate a substantial fraction of plate convergence over short time intervals (e.g., Lay et al., 2005; Moreno, Rosenau, and Oncken, 2010; Ozawa et al., 2011). Characterized by rapid coseismic slip that can reach tens of meters, these events represent the abrupt release of elastic energy accumulated during prolonged interseismic loading from plate motions. Beyond their immediate coseismic impacts, great earthquakes induce long-lasting perturbations in stress and deformation within adjacent fault segments as well as the surrounding lithosphere and mantle (e.g., Fig. 1.2; Wang, Hu, and He, 2012; Melnick et al., 2017), influencing subsequent seismic activities and regional tectonic evolution. These processes are increasingly well resolved by the improved availability and precision of geodetic measurements, particularly through the dense Global Navigation Satellite System (GNSS) network (Kreemer, Blewitt, and Klein, 2014; Blewitt, Hammond, and Kreemer, 2018).

Despite their intrinsic physical link and complex interactions, these quasi-steady and transient processes are usually investigated in separate modeling frameworks focusing either on long-term geodynamics (e.g., Hager and O'Connell, 1981; Zhong and Gurnis, 1995; Stadler et al., 2010) or short-term seismic cycles (e.g., Lapusta and Liu, 2009; Barbot, Lapusta, and Avouac, 2012; Jiang et al., 2022). Several pioneering studies have attempted to bridge this gap by incorporating megathrust earthquakes into two-dimensional (2D) geodynamic models using one-way coupling approaches (e.g., Dinther et al., 2013; Sobolev and Muldashev, 2017; Yang et al., 2023). With tectonic loading from prescribed plate motions, these models reproduce key features of rapid coseismic deformation and shed light on the interplay between rupture processes and regional tectonics. However, the imposed plate kinematics may not be fully consistent the evolving rheology and force balance of the system. These 2D cross-section computations also fail to account for finite-length ruptures and along-strike variations in stress and slip along the plate boundary. On the other

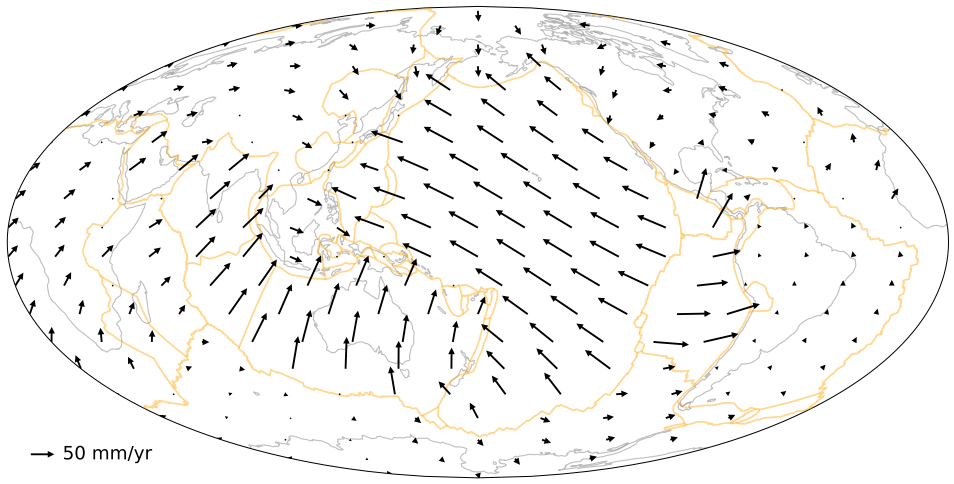

Figure 1.1: Non-net-rotation long-term plate motions calculated from NNR-MORVEL56 (Argus, Gordon, and DeMets, 2011). The orange lines indicate plate boundaries. Regions close to plate boundaries are excluded from the calculation and masked.

hand, it remains computationally challenging to compute full three-dimensional (3D) cross-scale models over realistic domains to simultaneously resolve large-scale mantle flow and localized megathrust rupture processes that span many orders of magnitude in space and time.

Recent advances in numerical methods and high-performance computing have made it possible to implement 2D and 3D models over complex geometries and self-consistently integrate the multi-scale behavior of the solid Earth. In this thesis, we develop cross-scale finite-element models that simultaneously resolve the dynamics of long-term plate motions and great megathrust earthquakes with a consistent non-linear visco-elasto-plastic rheology. The objectives of this work are two-fold. Firstly, we aim to investigate the physical mechanisms linking large-scale tectonic processes and the occurrence, size and variability of great megathrust earthquakes. Secondly, we seek to constrain the rheological properties in Earth's interior by assimilating geophysical observations across different length and time scales, including plate velocities, stress orientations, and coseismic and postseismic deformation.

Chapter 2 establishes the foundation by introducing a generic subduction zone model that generates both long-term plate motions and megathrust seismic cycles consistent with observations in subduction zones. The model allows plate convergence and interseismic stress accumulation to emerge self-consistently as a consequence of buoyancy forces in a visco-elasto-plastic system, and rupture events are triggered by

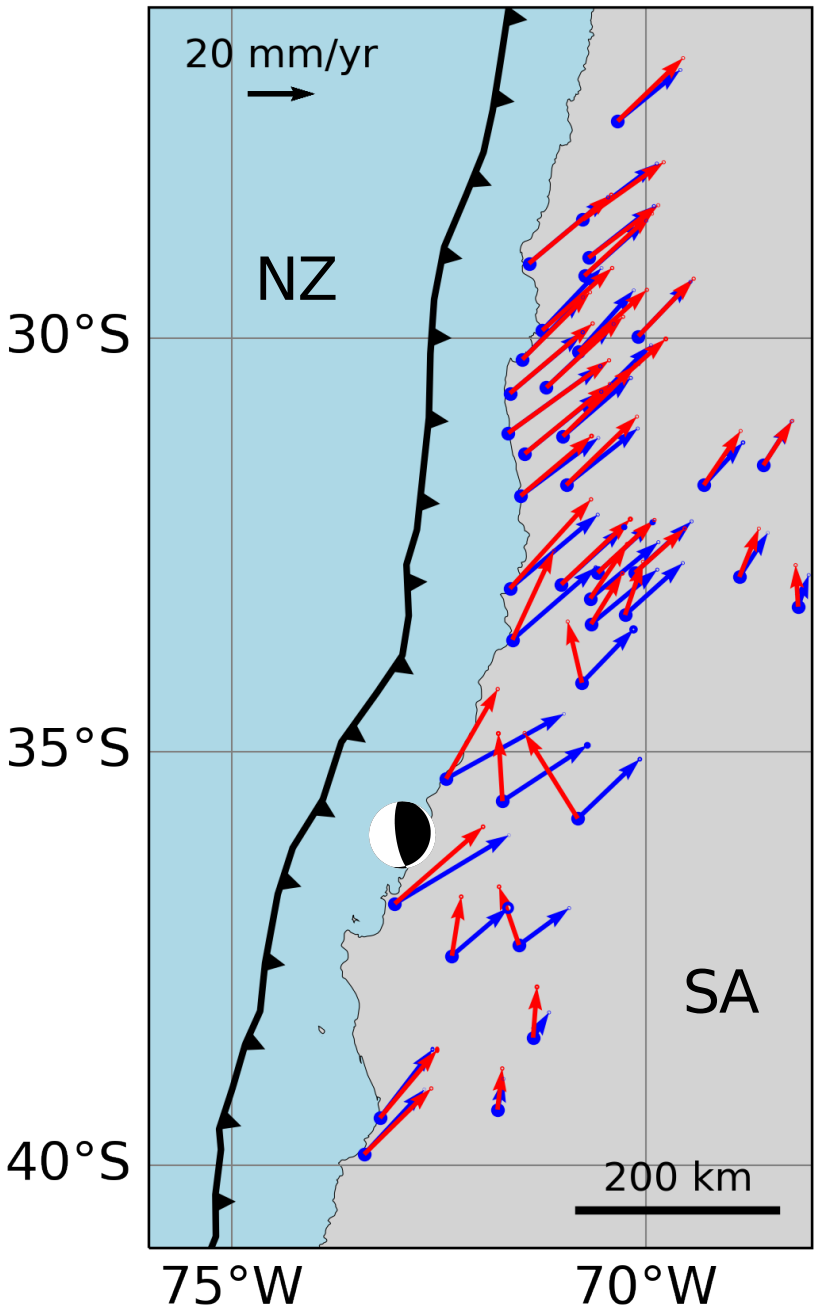

Figure 1.2: Geodetic surface velocities before (blue) and after (red) the 2010 Maule earthquake ($M_w = 8.8$) (Melnick et al., 2017). The teeth line indicates the location of the trench, and the beachball marks the earthquake epicenter and focal mechanism. NZ and SA denote the Nazca Plate and South American Plate, respectively.

spontaneous slip instability due to a rate-weakening friction within the megathrust shear zone. Along-strike resistance arising from slip variations is incorporated through an efficient 2.5-dimensional model setup to model more realistic finite-length ruptures, and the results show its important role in modulating the coseismic slip and earthquake magnitude.

Building upon this framework, Chapter 3 investigates the influence of rupture dimensions, rheological properties and subduction characteristics on the plate velocity, coseismic slip and earthquake recurrence interval. By systematically varying the related parameters, we demonstrate that the long-term and coseismic deformations are jointly modulated by multi-scale rheological and structural controls. The model also provides insight into the physical origin of observed earthquake scaling relationships.

Chapter 4 moves toward a three-dimensional model of the Chilean Subduction Zone that reconciles experimentally-derived olivine rheology, plate motions and postseismic deformation patterns. While multiple cases can match either the long-term velocity of the Nazca Plate or the enhanced landward motion (ELM) after the 2010 Maule earthquake (M_w = 8.8), only a narrow intersection of the parameter space satisfies both constraints. Combining these geodetic datasets across length and time scales significantly improve constraints on the nonlinear mantle rheology.

The first half of Chapter 5 extends the cross-scale model to the global scale and incorporates realistic plate geometry and thermal structures. The extreme-scale model computations are powered by the highly scalable finite-element code *Rhea* with advanced Newton's methods for viscoplastic and visco-elasto-plastic problems. The adaptive mesh refinement (AMR) resolves plate boundaries at a 1-km resolution in a global-scale model. The model integrates background plate kinematics with transient perturbations from giant earthquakes and reveals their sensitivity to different rheological properties in Earth's interior.

The second half of Chapter 5 further advances the modeling framework by implementing a true free surface and couples plate motions, surface topography, and off-megathrust stress state. We show a proof-of-concept model to illustrate the structural and rheological controls on diverse patterns in deformation and seismicity.

This work demonstrates the potential of unified, physics-based cross-scale models for integrating diverse geophysical observations within a consistent mechanical framework. By bridging the gap between long-term geodyanmics and transient

earthquake processes, these models provide valuable insight into their coupled dynamics, which improves constraints on Earth's rheological structure and advances our understanding of seismic hazards in subduction zones.

References

Argus, Donald F, Richard G Gordon, and Charles DeMets (2011). "Geologically current motion of 56 plates relative to the no-net-rotation reference frame". In: *Geochemistry, Geophysics, Geosystems* 12.11.

Barbot, Sylvain, Nadia Lapusta, and Jean-Philippe Avouac (2012). "Under the hood of the earthquake machine: Toward predictive modeling of the seismic cycle". In: *Science* 336.6082, pp. 707–710.

Blewitt, Geoffrey, William Hammond, and Corn Kreemer (2018). "Harnessing the GPS data explosion for interdisciplinary science". In: *Eos* 99.2, e2020943118.

DeMets, Charles, Richard G Gordon, and Donald F Argus (2010). "Geologically current plate motions". In: *Geophysical journal international* 181.1, pp. 1–80.

Dinther, Y van et al. (2013). "The seismic cycle at subduction thrusts: Insights from seismo-thermo-mechanical models". In: *Journal of Geophysical Research: Solid Earth* 118.12, pp. 6183–6202.

Hager, Bradford H and Richard J O'Connell (1981). "A simple global model of plate dynamics and mantle convection". In: *Journal of Geophysical Research: Solid Earth* 86.B6, pp. 4843–4867.

Jiang, Junle et al. (2022). "Community-driven code comparisons for three-dimensional dynamic modeling of sequences of earthquakes and aseismic slip". In: *Journal of Geophysical Research: Solid Earth* 127.3, e2021JB023519.

Kreemer, Corné, Geoffrey Blewitt, and Elliot C Klein (2014). "A geodetic plate motion and Global Strain Rate Model". In: *Geochemistry, Geophysics, Geosystems* 15.10, pp. 3849–3889.

Lapusta, Nadia and Yi Liu (2009). "Three-dimensional boundary integral modeling of spontaneous earthquake sequences and aseismic slip". In: *Journal of Geophysical Research: Solid Earth* 114.B9.

Lay, Thorne et al. (2005). "The great Sumatra-Andaman earthquake of 26 december 2004". In: *science* 308.5725, pp. 1127–1133.

Melnick, Daniel et al. (2017). "The super-interseismic phase of the megathrust earthquake cycle in Chile". In: *Geophysical Research Letters* 44.2, pp. 784–791.

Moreno, Marcos, Matthias Rosenau, and Onno Oncken (2010). "2010 Maule earthquake slip correlates with pre-seismic locking of Andean subduction zone". In: *Nature* 467.7312, pp. 198–202.

Ozawa, Shinzaburo et al. (2011). "Coseismic and postseismic slip of the 2011 magnitude-9 Tohoku-Oki earthquake". In: *Nature* 475.7356, pp. 373–376.

Sobolev, Stephan V and Iskander A Muldashev (2017). "Modeling seismic cycles of great megathrust earthquakes across the scales with focus at postseismic phase". In: *Geochemistry, Geophysics, Geosystems* 18.12, pp. 4387–4408.

Stadler, Georg et al. (2010). “The dynamics of plate tectonics and mantle flow: From local to global scales”. In: *Science* 329.5995, pp. 1033–1038.

Wang, Kelin, Yan Hu, and Jiangheng He (2012). “Deformation cycles of subduction earthquakes in a viscoelastic Earth”. In: *Nature* 484.7394, pp. 327–332.

Yang, Haibin et al. (2023). “Numerical Modeling of Earthquake Cycles Based On Navier-Stokes Equations With Viscoelastic-Plasticity Rheology”. In: *Geochemistry, Geophysics, Geosystems* 24.9, e2023GC010872.

Zhong, Shijie and Michael Gurnis (1995). “Mantle convection with plates and mobile, faulted plate margins”. In: *Science* 267.5199, pp. 838–843.

Chapter 2

DYNAMIC EMERGENCE OF PLATE MOTIONS AND GREAT MEGATHRUST EARTHQUAKES ACROSS LENGTH AND TIME SCALES

Fang, Jiaqi, Michael Gurnis, and Nadia Lapusta (2024). "Dynamic emergence of plate motions and great megathrust earthquakes across length and time scales". In: *Geophysical Research Letters* 51.22, e2024GL110821. DOI: 10.1029/2024GL110821.

Abstract

The slow motion of tectonic plates over thousands of kilometers is intermittently interrupted by great earthquakes with sudden slips localized near convergent plate boundaries. We developed a subduction model that self-consistently integrates buoyancy forces, diffusion and dislocation creep, and inter-plate friction. From the nonlinear dynamics emerge long-term plate motions that achieve velocities of ≈ 5 cm/year, effective viscosities of $\approx 10^{19}$ Pa·s below plates, and sudden slips up to ≈ 10 m repeating every several hundred years. Along-strike resistance arising from long-wavelength variation of coseismic slip is naturally incorporated with a rupture length scale, $\tilde{L}$. Computations with $\tilde{L} \sim 10^3$ km generate events with $M_w \approx 9$. When $\tilde{L}$ decreases, there is a commensurate decrease in the effective moment of rupture events. Predicted long-term plate velocities, mantle viscosities, cycles of stress loading and release, and rupture event size and magnitude all show good agreement with observations.

2.1 Introduction

Megathrust faults at convergent plate boundaries host the largest earthquakes with slips of meters that interrupt the regular several cm/year plate motions. Historical records of megathrust earthquakes show a complicated variability in space, time and source properties (Sykes and Quittmeyer, 1981; Thatcher, 1990; Ye, Kanamori, and Lay, 2018; Bilek and Lay, 2018). This variability is thought to be intimately linked to physical properties of the megathrust, e.g., the interface roughness, material composition, sediment thickness, fluid content and thermal structure, which directly influence rupture mechanics (Hyndman, Yamano, and Oleskevich, 1997; Heuret et al., 2012; Wang and Bilek, 2014; Li, Shillington, et al., 2018; Wirth et al., 2022).

Larger-scale geodynamic controls, such as subduction zone geometry and mantle rheology, also play a crucial role in shaping the complexity of megathrust earthquake occurrence, as they modulate the tectonic loading, material transport, and ultimately stresses delivered to the megathrust (Ruff and Kanamori, 1980; Wang, Hu, and He, 2012; Nishikawa and Ide, 2014; Dal Zilio, Dinther, et al., 2018; Wirth et al., 2022). Meanwhile, background plate motions, resulting from a balance between the driving slab pull and resisting forces, including the viscous shear in the asthenosphere, plate bending and plate boundary friction, are regulated by the same factors inside and outside the megathrust (Zhong, Gurnis, and Moresi, 1998; Conrad and Hager, 1999; Alisic et al., 2012; King, 2016; Behr et al., 2022; Li and Gurnis, 2023). Cycles of steady interseismic motions and sudden coseismic slip reflect an intricate interplay between tectonic structures and material properties.

As plate motions and earthquake ruptures span a large range of length and time scales and are thought to be governed by different constitutive relationships, it has been challenging to integrate them into a unified computational model. Models of long-term plate deformation (Zhong and Gurnis, 1995; Tackley, 2000; Stadler et al., 2010) and seismic cycles (Lapusta and Liu, 2009; Barbot, Lapusta, and Avouac, 2012; Li and Liu, 2021) are usually implemented separately. For subduction zones, there have been a few studies using 2D cross-sections with visco-elasto-plasticity that generate earthquake-like ruptures and seismic cycles consistent with observations (van Dinther et al., 2013, 2014; Herrendörfer et al., 2015; Sobolev & Muldashev, 2017; Oryan & Buck, 2020; Dal Zilio et al., 2022). They provide valuable insight into the interplay between tectonic loading, rapid rupture processes, lithosphere stress state and aftershock seismicity. Critically, the imposed loading velocity boundary conditions are not self-consistent with the rheology in the system and ignore the impact of great earthquakes on long-term plate motions and stress states. Being 2D, existing approaches miss along-strike slip variations. A great earthquake only ruptures a finite length along the plate boundary and displacements of the rupturing segment will be resisted by forces imposed by adjacent non-rupturing segments. Typically, the size in this third dimension governs how large a megathrust earthquake becomes (Kanamori, 1978; Scholz, 1982).

We formulated a visco-elasto-plastic subduction model that treats the dynamics of plate tectonics self-consistently with great megathrust earthquakes. The model is driven by negative buoyancy with a realistic thermal structure instead of imposed kinematics while employing experimentally-derived rheological parameters. The

model is capable of simultaneously predicting long-term plate motion and mantle convection as well as short-term slip and relaxation behaviors. Given the computational difficulties, instead of implementing a full 3D model, we efficiently incorporate the along-strike resistance by expanding the model into a small thickness and applying tractions proportional to the incremental displacements that occur during a megathrust rupture. The results highlight how the length scale of this along-strike resistance from long-wavelength slip variations modulates rupture behaviors.

2.2 Methods

The 2D model

The models are computed using Underworld2, open-source finite-element software that solves the conservation of mass and momentum for an incompressible medium (Moresi, Quenette, et al., 2007; Mansour et al., 2020). Originally tailored for long-time-scale mantle convection, Underworld2 has been adapted to shorter-time-scale problems with Maxwell viscoelastic and visco-elasto-plastic rheology (Moresi, Dufour, and Mühlhaus, 2002; Farrington, Moresi, and Capitanio, 2014). This computational method has expanded its applicability to earthquake-related problems (Yang et al., 2023), which has also been demonstrated with several other numerical implementations (Dinther et al., 2013; Sobolev and Muldashev, 2017; Dal Zilio, Lapusta, et al., 2022).

We set up a 2D model of a 4040×660 km^2 trench-normal section with the whole incoming plate (Figure 2.1A). The megathrust is approximated by a 6-km-wide shear zone between the incoming and overriding plates (Figure 2.1B). The domain boundaries are free-slip, and the deformation is driven entirely by internally generated forces. The system has initial conditions based on results of large-time-step computations, which reflect the long-term dynamics of this system, and progresses through multiple cycles of coseismic, postseismic and interseismic phases with a time step size of 5 years. Displacements and stress changes are averaged over each 5-year step and the inertia term is omitted. The mesh has 1024×256 linear elements and is refined in the area near the megathrust, with a minimum element size of 1.2 km.

The rheology of the lithosphere and mantle is a composite of creeping, elastic and plastic processes, with key parameters listed in Table 2.S1. The viscosity (Figure 2.1D) is determined by diffusion and dislocation creep (Karato and Wu, 1993; Ranalli, 1995). The shear modulus is 30 GPa for the shear zone, top 6 km of the

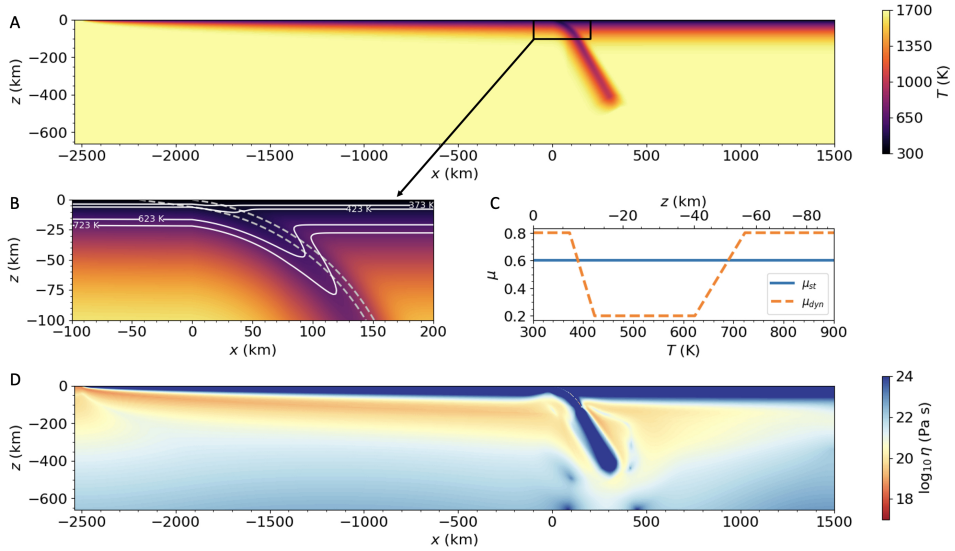

Figure 2.1: (A) Thermal structure of the model (see details in Text S2). x, z and T denote the horizontal length, depth and temperature. (B) Enlargement of the thermal structure near the megathrust with shear zone (width is 6 km, $\approx 5\times$ local element size) surrounded by silver dashed lines. (C) The temperature-dependent frictional parameters, μ_{st} and μ_{dyn}, in the shear zone. The top secondary axis shows the depth z corresponding to the temperature T. (D) Effective viscosity η initially for the model, from a viscously-dominated computation with a large time step size.

incoming plate and 20 km of the overriding plate, and 60 GPa for other parts of the bulk lithosphere and mantle throughout. Plastic yielding follows the Drucker-Prager criterion in which the second invariant of the deviatoric stress, τ_{II}, is limited by a yield stress defined as:

$$\tau_y = C + \mu P\,(1 - \lambda)\,, \tag{2.1}$$

where C is the cohesion, μ is the friction coefficient, P is the pressure, and λ is a pore pressure factor. Fluids in the megathrust are approximated with a fixed pore pressure factor $\lambda = 0.95$ in the shear zone shallower than 60 km and a linear transition from 0.95 to 0 from 60 to 80 km.

Rate-dependent friction coefficients from Dinther et al. (2013) are applied in the shear zone:

$$\mu = \mu_d + \frac{\mu_s - \mu_d}{1 + \frac{V}{V_{ref}}}, \tag{2.2}$$

where μ_s and μ_d are static and dynamic friction coefficients, V_{ref} is a reference slip velocity, and V is the local slip velocity, defined as twice the shear zone width

multiplying the second invariant of the strain rate (Dinther et al., 2013; Yang et al., 2023). The temperature dependence of frictional parameters in the shear zone (Figure 2.1C) is guided by previous studies (Liu and Rice, 2005; Den Hartog, Niemeijer, and Spiers, 2012). The top and bottom sections are rate-strengthening ($\mu_d > \mu_s$), favoring stable aseismic slip. The strong rate-weakening friction ($\mu_d < \mu_s$) allows spontaneous slip instability in the seismogenic zone at an intermediate depth. The modeling technique developed in this work will allow us to consider other laboratory-derived constitutive formulations for faults that have been shown to reproduce a number of earthquake source phenomena, such as rate-and-state friction and additional effects due to frictional shear heating, evolution of pore fluid pressure, and coupling between on-fault and off-fault deformation (Dieterich, 1979; Marone, 1998; Rice, 2006; Ampuero and Ben-Zion, 2008; Segall et al., 2010; Di Toro et al., 2011; Faulkner et al., 2011; Allison and Dunham, 2021; Lambert, Lapusta, and Perry, 2021).

The 2.5D model with along-strike resistance

Rapid slips in the rupturing segment will encounter resistance from neighboring non-rupturing segments during a great megathrust earthquake, an effect missing in 2D. While a full 3D model is computationally prohibitive, we compensate for the lack of along-strike resistance by expanding the domain in the x–z plane to two elements with a thickness of 5 km in the along-strike y direction and initializing with state variables from the step before the first rupture event. The thin 2.5D model is located at the center of the rupturing zone and a traction is imposed on the front wall, which is caused by the strain between the rapidly advancing segment in the model domain and distal segments with an interseismic velocity. The expected shear traction is proportional to a long-wavelength displacement difference and inversely proportional to an along-strike length scale, L:

$$\tau^e = -G\frac{u - u^{far}}{L} = -G\Delta t\frac{v - v^{far}}{L}, \tag{2.3}$$

where τ^e is the traction on the front wall, $u - u^{far}$ and $v - v^{far}$ denotes the displacement and velocity difference from a distal reference, τ^e_{xy} depends on $v_x - v_x^{far}$, τ^e_{zy} depends on $v_z - v_z^{far}$, and $\tau^e_{yy} = 0$. Equation 2.3 is essentially a Robin boundary condition that specifies a linear combination of velocity and stress on the front wall. With Robin boundary conditions not available in Underworld2, we developed an iterative approach using evolving Neumann boundary conditions within each step. The traction applied on the front wall is constantly updated in each iteration based

on Equation 2.3, until the misfit between the applied traction and expected traction calculated from the velocity solution is below 1%.

The parameter L reflects the gradient of slips at the front wall and describes a length scale of this along-strike resistance due to the long-wavelength displacement difference between the rupture center and non-rupturing distal segments. A small L indicates rupture confined to a narrow along-strike width, and conversely for a large L. Considering the nonlinear decay of slip in the along-strike direction, L scales with, but is usually larger than the actual along-strike size of an earthquake. If we take an analytical elastic crack model – an elliptical slip distribution along the strike with a maximum slip of U_0 at the rupture center and extending for a length of $2\tilde{L}$ (Scholz, 2019), our boundary condition translates into a slip gradient of $-\frac{U_0}{L}$ at a distance of the domain width ($D = 5$ km) from the rupture center. By equating the gradient in this analytical solution ($-\frac{U_0 D}{\tilde{L}\sqrt{\tilde{L}^2-D^2}} \approx -\frac{U_0 D}{\tilde{L}^2}$) with the boundary condition, we obtain:

$$\tilde{L} \approx \sqrt{LD}. \tag{2.4}$$

Despite uncertainties from geometric complexity and material heterogeneity, this relation converts the parameter L in Equation 2.3 to a rupture length scale $\tilde{L}$. In realistic scenarios, the rupture length can be controlled by the lithosphere thickness and the along-strike variability in the plate geometry, and investigation of these complications will require 3D models that incorporate such along-strike changes.

2.3 Results

With a realistic thermal structure derived from the cooling of plates and slabs (Figure 2.1A) and a set of experimentally-constrained creeping and frictional parameters (Table 2.S1), the slow motion of plates emerges but is disrupted by abrupt slips of 10 rupture events in 2000 years, with a period of ≈200 years (Figure 2.2). For the entire incoming plate, the average surface displacements over these seismic cycles has the incoming plate moving at a steady velocity of ≈5 cm/year, consistent with the initial thermal structure as well as the long-term plate velocity from viscously dominated computations with a large time step size. The surface velocity shows different patterns co- and inter-seismically (Figure 2.2A): Prior to a rupture event, the surface velocity on both incoming and overriding plates show in-plane compression, which quickly flips to tension during the event. On the incoming plate, the pace at locations near the trench is up to 1 cm/year slower than the average plate velocity between rupture events, but accelerates substantially in areas near the trench during

a coseismic phase, leading to a leap in meters of displacement (Figure 2.2C). The plate maintains slow velocities (equal to the long-term average) at a distance larger than 1500 km from the trench. The overriding plate is compressed by the advancing incoming plate and areas near the trench move slightly forward at 2-3 cm/year. During the rupture event, the overriding plate becomes decoupled and experiences rebound of more than 1 m in the opposite direction. Both the interseismic movement and coseismic rebound diminish with distance from the trench. The results generally align with the elastic rebound theory where the elastic strain is gradually built up by interseismic displacements and abruptly released by coseismic slips, despite non-negligible permanent viscous deformation on both incoming and overrding plates. Over the 2000 years of the model, the incoming plate shows an extension of 2 m (1 km/Myrs) and the overriding plate is compressed by 0.5 m (0.25 km/Myrs) at locations 100 km away from the trench, compared with the average plate motion (Figure 2.2C). Changes in far-field boundary conditions, rheological parameters and plate geometry do not influence first-order model outcomes, although the interseismic period and coseismic slip may vary when convergence rates are different (Figures 2.S1–2.S8).

The space–time variations of slip (Figure 2.2B) and stresses (Figure 2.2D) show cyclical patterns. The coseismic stress changes near the megathrust are further shown in Figures 2.S9–2.S11. In the interseismic phase, the megathrust remains locked in the section shallower than 30 km and the portion deeper than 40 km, where the temperature is higher, steadily creeps at a rate close to the plate velocity. The main thrust event is characterized by extensive slip triggered along the megathrust, with a maximum of $\approx$13 m at a depth of 10–30 km. The section at a depth of 8–40 km can be defined as the seismogenic zone, where stresses accumulate during the interseismic period and suddenly released by rupture. With high pore fluid pressure imposed, shear stresses in the seismogenic zone are 10–30 MPa and the maximum coseismic drop is 8 MPa (Figure 2.2D). Conversely, there is a prominent increase in deviatoric stress in the updip and downdip portions of the shear zone. Due to a rate-strengthening friction below 380 K (depth < 7 km), stresses in the stable-sliding updip section exhibits an increase of 0.6 MPa during rupture but drop immediately afterwards due to notable afterslip. The coseismic stress increase is 7 MPa at the downdip rupture tip and decays exponentially when the temperature increases with depth, although the rate-weakening parameter setting continues to a depth of 50 km (700 K). In this section, the loaded stresses gradually relax after the rupture. This depth variation underscores a brittle-to-ductile transition: While

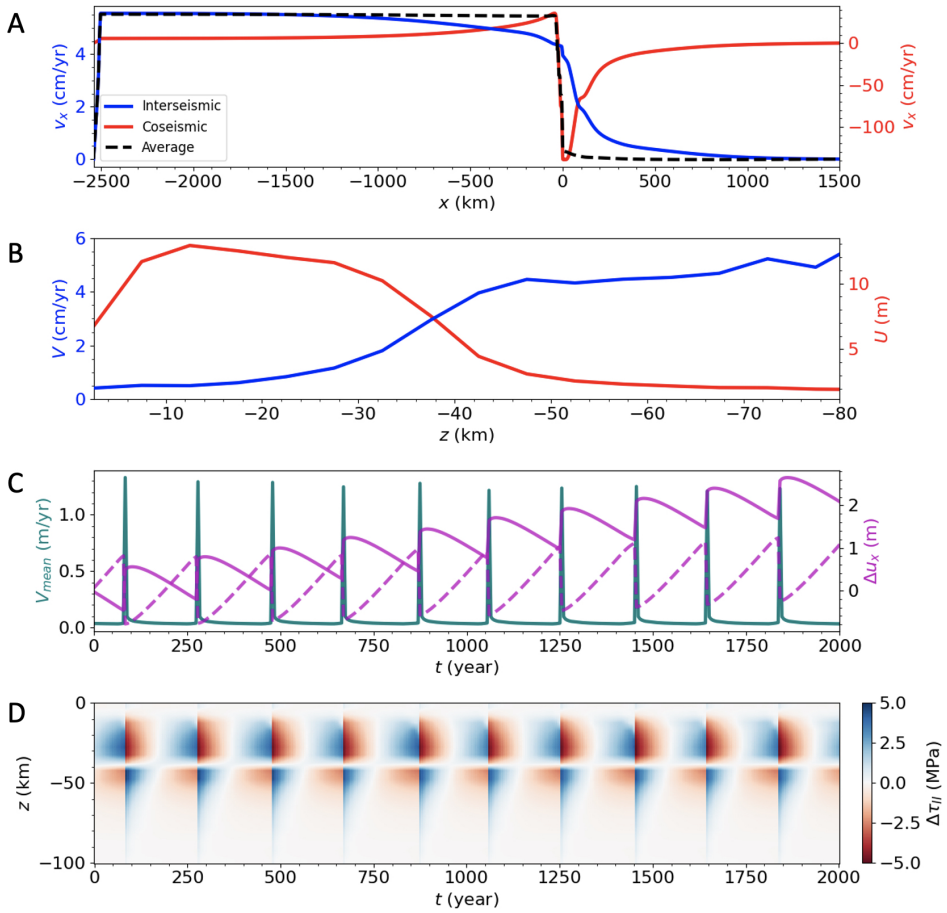

Figure 2.2: (A) The surface horizontal velocity, v_x, along a profile perpendicular to the trench at an interseismic time step (blue solid), at a coseismic time step (red solid), and averaged over the time span of 2000 years (black dashed). As the time step size is 5 years, coseismic velocities represent integrated coseismic displacements over a step of 5 years. (B) The slip velocity V at an interseismic time step (blue) and the slip U at a coseismic time step (red) in the shear zone versus the depth z. (C) The evolution of the mean slip velocity in the shear zone, V_{mean}, is depicted by the teal solid line. Each peak represents a rupture event. The cumulative displacement relative to the average plate motion, Δu_x, is plotted with magenta solid (at $x = -100$ km, on the incoming plate) and magenta dashed ($x = +100$ km, on the overriding plate) lines. (D) Space–time pattern of the relative stress change, $\Delta\tau_{II}$, in the shear zone. $\Delta\tau_{II}$ is calculated by subtracting the 2000-year mean of τ_{II} at each depth from the second invariant of the deviatoric stress τ_{II}.

plastic strength limits the stresses in the cold section, viscous strength regulates the shear zone deformation at temperatures above 620 K.

When a traction (proportional to the long-wavelength displacement difference between the rupture center and distal segments) is applied on the front wall, the rupture

length scale, $\tilde{L}$, modulates the size and magnitude of rupture (Figures 2.3–2.4). These results are generally insensitive to the number of elements and the domain width in the along-strike direction (see Figures 2.S12–2.S13). When $\tilde{L} \geq 1000$ km ($L \geq 2 \times 10^5$ km), the rupture behavior aligns with results in 2D (effectively $\tilde{L} = +\infty$), because the along-strike resistance associated with such a large scale is negligible. Under these conditions, plates can experience acceleration across spans greater than 1000 km from the trench, with coseismic slips reaching up to 13 m. As $\tilde{L}$ decreases, resisting forces become stronger, reducing slips along the entire megathrust, with the maximum slip dropping from 13 m to 4 m and near-surface displacements vanishing from 6 m to almost zero (Figure 2.3). The extent of plate acceleration narrows from a range of > 1000 km to a confined zone close to the trench. On the incoming plate, areas near the trench exhibit a coseismic displacement of 1.8 m for $\tilde{L} = 1000$ km ($L = 2 \times 10^5$ km), which converges to 0.2 m for $\tilde{L} = 32$ km ($L = 2 \times 10^2$ km), which is the interseismic movement over each computational step of 5 years. The coseismic rebound on the overriding plate reaches 7 m for $\tilde{L} = 1000$ km but gradually decreases for smaller along-strike length scales. When $\tilde{L} \leq 32$ km, these displacements towards the trench are eventually impeded at the surface, and ruptures are restricted near the shear zone at a depth of 8–40 km (380–620 K) with limited slip (Figure 2.3C). The reduction in both the incoming plate displacement and the maximum slip is most evident when $\tilde{L}$ decreases in the critical range between 700 and 20 km, which is mapped from Equation 2.4 for L decreasing from 10^5 to 10^2 km (Figure 2.4). This range represents a critical threshold for a pronounced influence of $\tilde{L}$ on the rupture behavior. The displacements at the surface tend to converge to pre-rupture values for such a small along-strike length scale but the maximum slip exceeds the interseismic level, indicating slips still occur despite the locked shallow section.

2.4 Discussion

The model produces both long-term plate motions and states of stress, as well as their short-term changes in seismic cycles. Both are governed by complex interactions between conditions inside the megathrust and characteristics of the surrounding lithosphere and mantle. The long-time-scale movement of the incoming plate at 5 cm/year is an outcome of the force balance within the subduction zone. The slab pull, the dominant driving force for plate motion, competes with the resistance from mantle viscous shear, plate bending, and interplate friction – processes that are regulated by mantle viscosity, lithosphere yield stress, and inter-plate friction (Conrad

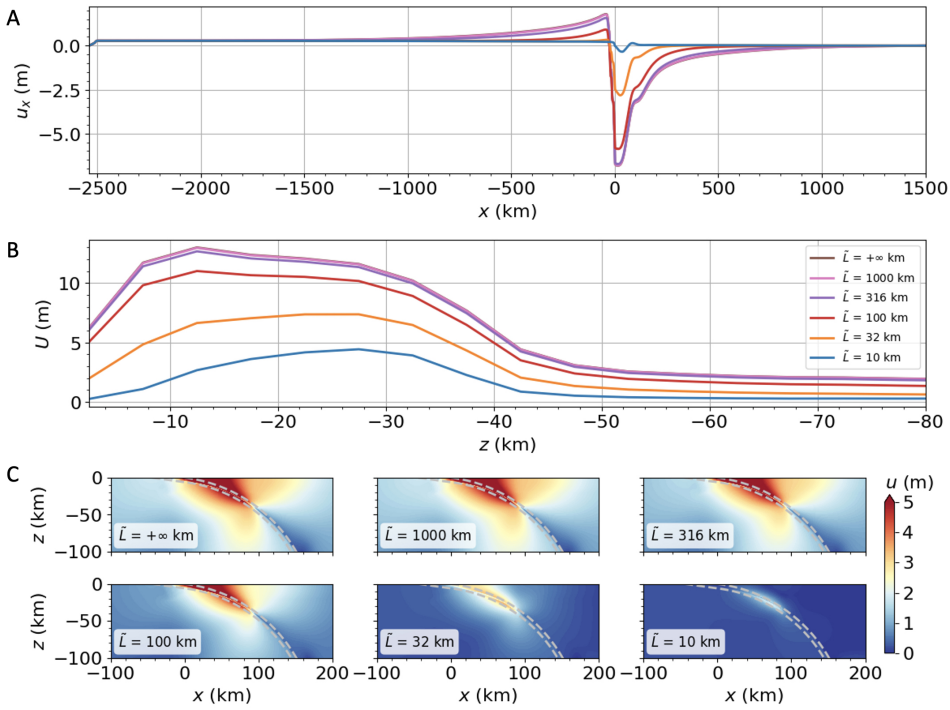

Figure 2.3: (A) The coseismic surface displacement, u_x, along a profile perpendicular to the trench for cases with different rupture length scales $\tilde{L}$. (B) The coseismic slip U in the shear zone versus the depth z for the same cases. (C) Coseismic displacement near the trench in representative events with different values of $\tilde{L}$. Silver dashed lines show the location of the shear zone.

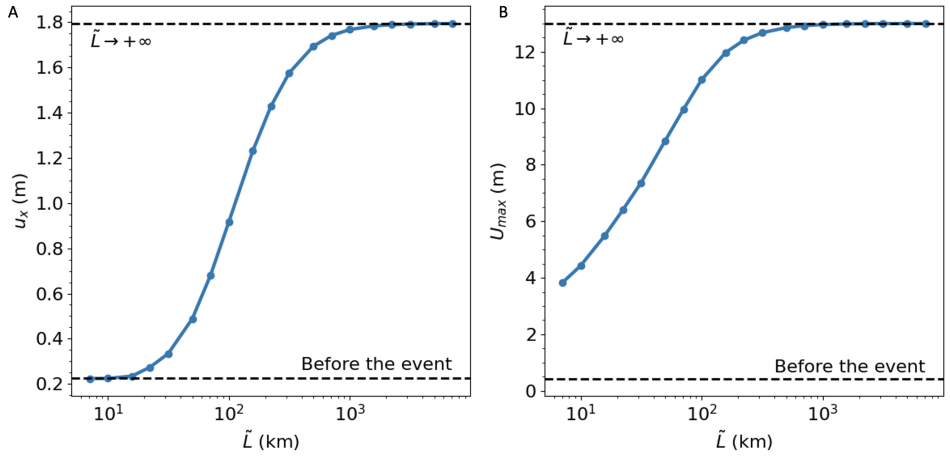

Figure 2.4: (A) The coseismic surface displacement of the incoming plate near the trench u_x and (B) the maximum coseismic slip in the shear zone U_{max} versus the rupture length scale $\tilde{L}$. The upper dashed lines represent u_x and U_{max} for a case without along-strike resistance ($\tilde{L} \to \infty$) and the respective quantity before the rupture event.

and Hager, 1999; Alisic et al., 2012; King, 2016; Behr et al., 2022). The viscosity decreases from 10^{24} Pa·s in the lithosphere to 10^{19} Pa·s in the asthenosphere below tectonic plates due to higher temperatures and non-Newtonian strain-rate weakening (Figure 2.1D), which aligns with postseismic relaxation estimates beneath the Indian Plate (Hu et al., 2016). When the incoming plate slides beneath the overriding plate, bending of the plate causes considerable deformation and energy dissipation in the hinge zone limited by plastic yielding. As another important resisting force, the effective interplate friction is substantially reduced with fluids in the megathrust lubricating the plate interface and counteracting the lithostatic pressure. The long-term plate motion is dominated by visco-plastic deformations and the elastic properties of materials have a minimal influence on it.

On top of the background motions, rupture events emerge spontaneously by frictional slip instabilities and are shaped by the same factors that simultaneously regulate the long-term behavior. Mechanical properties of the megathrust, such as the shear modulus and friction coefficient, and processes that directly modify them significantly affect space–time patterns of megathrust earthquakes (Bilek and Lay, 2018; Ulrich, Gabriel, and Madden, 2022). High pore fluid pressures caused by various fluid-producing processes and slow diffusion in the megathrust can weaken the effective fault strength and allow earthquake occurrence (Saffer and Tobin, 2011). The impact of fluid content on slip behavior variations is substantiated by seismic coupling and earthquake observations in Alaska (Li, Shillington, et al., 2018; Wang, Wei, et al., 2024). Large-scale geodynamic controls influence the plate convergence that delivers stresses to the megathrust. Faster subduction can elongate the along-dip range where the slab temperature remains below the brittle-to-ductile threshold and make the seismogenic zone extend deeper (Hyndman, Yamano, and Oleskevich, 1997). Subduction zones with larger convergence rates may also experience faster tectonic loading and more frequent megathrust ruptures (Corbi et al., 2017; Wirth et al., 2022). The slip deficit in the locked section at depths of 8–40 km (380–620 K) builds up at 5 cm/year over an interseismic period of $\approx$ 200 years and then is released by rapid slips of $\approx$ 10 m. In contrast to elastic rebound theory, there is non-negligible permanent deformation in each cycle, with 0.2 m of extension on the incoming plate and 0.05 m of compression on the overriding plate associated with long-term motions. Although the model has an overriding plate in compression, we would expect that the state of stress to change with different factors such as convergence rate, slab geometry and inter-plate friction, as found empirically (Heuret et al., 2012).

In addition to processes within the cross-section, forces arising from slip variations in the along-strike direction are crucial for rupture behavior. A pronounced correlation between average slip and rupture length is supported by both observations and physical models (Sykes and Quittmeyer, 1981; Scholz, 1982; Kim and Sanderson, 2005). The 2D model, effectively with an infinite rupture length scale $\tilde{L}$, experiences large rupture events with extensive slips along the megathrust. With the actual rupture length $2\tilde{L}$ decreasing from 700 to 20 km in our 2.5D model, in accord with a smaller earthquake size in the along-strike direction, coseismic slips and earthquake magnitude diminish. For great earthquakes, the along-strike rupture length $2\tilde{L}$ dominates their sizes (Scholz, 1982). For an event rupturing 1400 km with an elliptical slip distribution in the along-strike direction and average slip of 10 m at an along-dip length of 100 km, the estimated seismic moment is $\approx 4 \times 10^{22}$ N·m, corresponding to a moment magnitude $M_w \approx 9$ (Hanks and Kanamori, 1979). This estimate is commensurate with some of the largest earthquakes in modern records, e.g., the 2004 Sumatra earthquake (Ammon, Ji, et al., 2005) and the 2011 Tohoku-oki earthquake (Ammon, Lay, et al., 2011). As $\tilde{L}$ drops from 1400 km to tens of kilometers, the model yields rupture events with M_w decreasing from 9 to 7, which roughly coincide with empirical relationships proposed by Wells and Coppersmith (1994) and Thingbaijam, Mai, and Goda (2017). However, since the along-dip rupture width in our 2.5D models is between 50 and 100 km, a rupture length beyond this lower limit might not represent realistic scenarios and is mainly for a conceptual understanding of along-strike resistance.

2.5 Conclusions

The subduction model generates seismic cycles self-consistent with plate tectonics and simultaneously replicates behaviors at different length and time scales. The plate motion in subduction zones is characterized by episodes of slow interseismic movements of 5 cm/year interrupted by rapid coseismic ruptures up to 13 meters during short time intervals. Strains and stresses are loaded by the steady movement of plates and then released by rapid slip, with a maximum stress drop of 6 MPa in the 2D model. These slow and fast episodes are shaped by both conditions within the plate interface and bulk properties of the surroundings that modulate the deformation and stress state in the megathrust. Converted from the boundary condition parameter L in Equation 2.3, the rupture length scale $\tilde{L}$ plays a critical role governing along-strike resistance in influencing the magnitude of rupture events. While $M_w \approx 9$ events with extensive slips emerge for large along-strike sizes ($\sim 10^3$

km), small along-strike sizes ($\sim$ 10 km) confine reduced slips to a narrow zone near the megathrust with the surface remaining locked. The efficient computations shed light on the critical importance of the along-strike length scale in the interaction between tectonic loading and megathrust rupture processes.

Supplementary material

Text S1. Dislocation and diffusion creep laws

Viscosities in the model are governed by a composite creep law with both dislocation and diffusion creep, which is parametrized as:

$$\eta_{disl/diff} = A^{-\frac{1}{n}} \dot{\epsilon}_{II}^{\frac{1-n}{n}} \exp\left(\frac{E + PV}{nRT}\right), \tag{2.S1}$$

where $\eta_{disl/diff}$ are viscosities determined by dislocation or diffusion creep law, A is a prefactor, n is the stress exponent, R is the gas constant, E is the activation energy, V is the activation volumn, $\dot{\epsilon}_{II}$ is the second invariant of the strain rate tensor, P is the pressure, and T is the temperature. The values of parameters are listed in Table 2.S1. The dislocation creep parameters are based on values for dry olivine-rich rocks for the bulk mantle and lithosphere and wet quartzites for the shear zone (Ranalli, 1995). The diffusion creep parameters are calculated based on values for dry olivine assuming a grain size of 1.5 mm (Karato and Wu, 1993). The model viscosities are calculated as:

$$\eta = \left(\frac{1}{\eta_{disl}} + \frac{1}{\eta_{diff}}\right)^{-1}, \tag{2.S2}$$

Text S2. Thermal structure

Temperatures of the incoming plate from ridge to trench and the underlying mantle are calculated using the half-space cooling model assuming a plate velocity of 5 cm/yr (consistent with the actual plate velocity), a plate age of 50 Myrs at the trench, a thermal diffusivity of 10^{-6} m^2/s, and a mantle potential temperature of 1700 K. Temperatures for each vertical profile on and below the overriding plate are calculated based on half-space cooling at a cooling age of 80 Myrs. The slab interface is assumed to be straight at depths between 100 and 400 km, with the slope equal to that at the depth of 100 km. For each profile perpendicular to the slab interface, temperatures are calculated based on the 1D thermal diffusion starting from the reference profile before subduction, i.e., the vertical temperature profile of the incoming plate at the trench (50 Myrs old). The diffusivity is 10^{-6} m^2/s and the diffusion time is equal to the along-dip distance divided by a plate velocity of 5

Table 2.S1: Model parameters.

Quantity	Symbol	Unit	Bulk value	Shear zone value
Dislocation creep[a]				
Exponent	n	—	3.5	2.3
Prefactor	A	$\mathrm{Pa}^{-n}\cdot\mathrm{s}^{-1}$	2.83×10^{-16}	3.13×10^{-17}
Activation energy	E	$\mathrm{J}\cdot\mathrm{mol}^{-1}$	5.32×10^{6}	1.54×10^{6}
Activation volume	V	$\mathrm{m}^3\cdot\mathrm{mol}^{-1}$	1.10×10^{-5}	0
Diffusion creep[b]				
Exponent	n	—	1.0	—
Prefactor	A	$\mathrm{Pa}^{-n}\cdot\mathrm{s}^{-1}$	1.40×10^{-11}	—
Activation energy	E	$\mathrm{J}\cdot\mathrm{mol}^{-1}$	3.00×10^{6}	—
Activation volume	V	$\mathrm{m}^3\cdot\mathrm{mol}^{-1}$	6.00×10^{-6}	—
Elasticity				
Shear modulus	G	GPa	30 – 60	30
Plastic yielding				
Cohesion	C	MPa	100	10
Static friction	μ_s	—	0.6	0.6
Dynamic friction	μ_d	—	0.6	0.2 – 0.8
Reference slip velocity	V_{ref}	cm/year	2.1	2.1
Pore pressure factor	λ	—	0	0 – 0.95
Maximum yield stress	τ_{max}	MPa	200	200

[a]Ranalli (1995). [b]Karato and Wu (1993).

cm/yr. Linear smoothing is applied in the buffer zone surrounding the slab, with a size that is twice the width of the zone where temperatures are below 1630 K. The temperature data are available on CaltechDATA at doi: 10.22002/awg6a-x3t07.

Text S3. Additional 2D models

In order to demonstrate the ability to simultaneously model long-term plate motions and rapid earthquake ruptures, we have computed several additional models with minor modifications on the original model. The model temperatures or viscosities, as well as their outcomes (akin to Figure 2 in the manuscript), are shown in Figures 2.S1–2.S8.

1. **Model A1** (Figures 2.S1–2.S2): The distance of the right boundary to the trench is extended from the original 1500 km to 2885 km. In both Model A1 and the original model, the surface horizontal velocity tapers to zero at distances < 1500 km to the trench. The plate velocities, interseismic period and coseismic slips all align closely, indicating that the free-slip boundary condition on the right wall has minimal influence on model behavior.

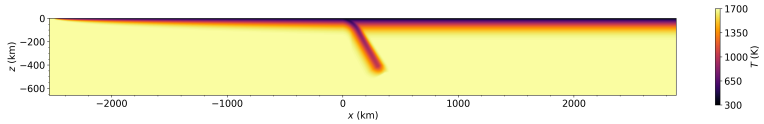

Figure 2.S1: Thermal structure of Model A1.

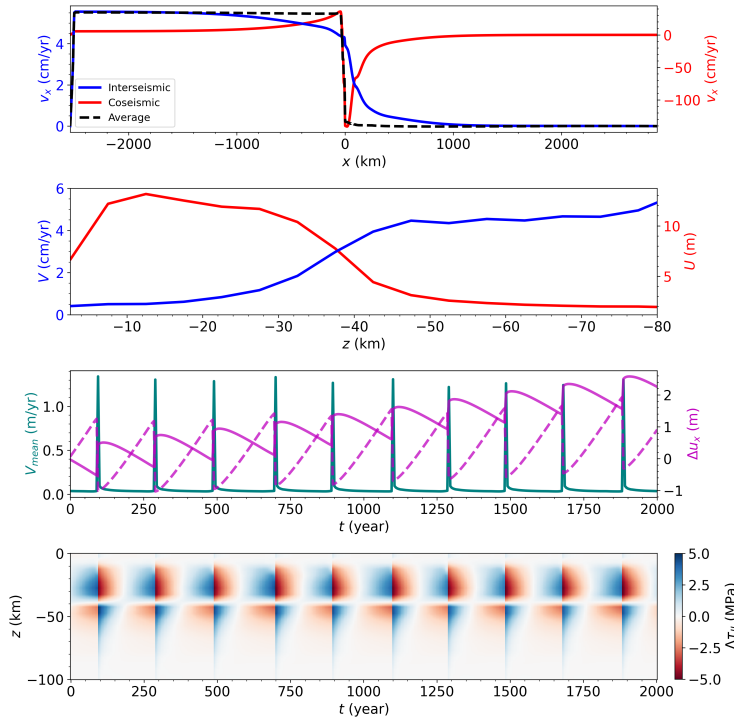

Figure 2.S2: Model outcomes of Model A1 (akin to Figure 2.2 in the manuscript). Symbols are the same as those in Figure 2.2.

2. **Model A2** (Figures 2.S3–2.S4): A 40-km-wide buffer zone is introduced to detach the overriding plate from the right boundary. The overriding plate is thus without direct pinning at the boundary of the domain. Although the overriding plate can move slightly leftward due to underlying mantle flow, all model behavior shows remarkable consistency with the original model.

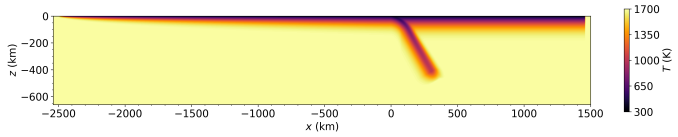

Figure 2.S3: Thermal structure of Model A2.

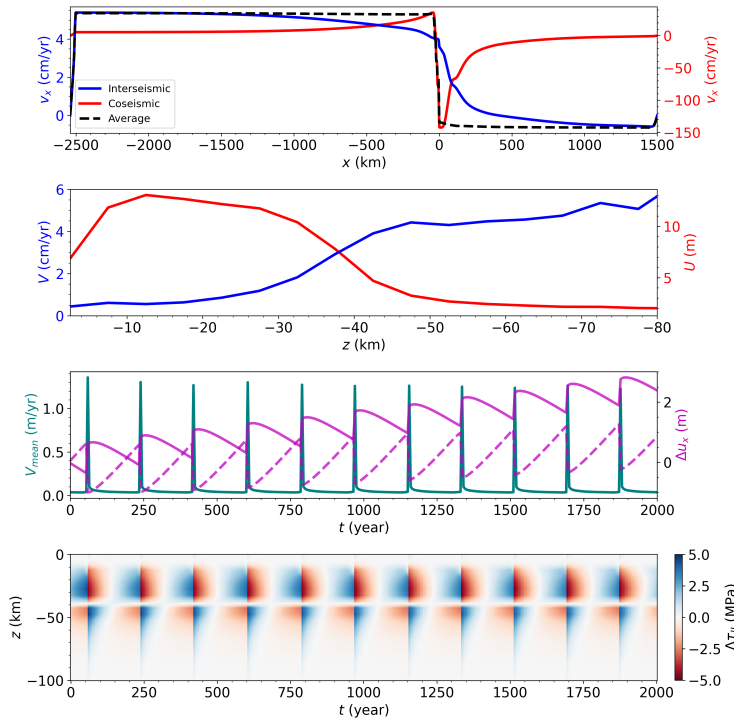

Figure 2.S4: Model outcomes of Model A2 (akin to Figure 2.2 in the manuscript). Symbols are the same as those in Figure 2.2.

3. **Model A3** (Figures 2.S5–2.S6): The model includes the lower mantle with a maximum depth of 1500 km and a subducting slab that reaches the 660-km interface. The lower mantle viscosities are governed by diffusion creep and the values of rheological parameters are adopted from Behr et al. (2022), and an adiabatic temperature gradient of 0.3 K/km is added following Behr et al. (2022). Under this configuration, the convergence rate is reduced to ≈ 3 cm/yr, which results in longer interseismic period, but all first-order long-term and short-term behaviors are preserved, including the steady interseismic plate motions, rapid coseismic slips and stress changes with reasonable values.

4. **Model A4** (Figures 2.S7–2.S8): Wet olivine rheology in Ranalli (1995) is used in the entire upper mantle, and the lithosphere yield stress is increased from 200 MPa to 300 MPa to maintain a reasonable plate velocity. In this extreme case, the asthenosphere viscosity is reduced and the plate velocity accelerates substantially ($\approx$ 10 cm/yr). The evolving interseismic and coseismic patterns of megathrust slips, surface displacements and megathrust stresses, remain clear, despite the shorter period due to faster loading.

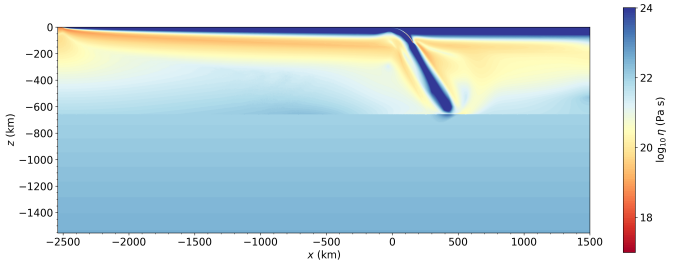

Figure 2.S5: Viscosities of Model A3.

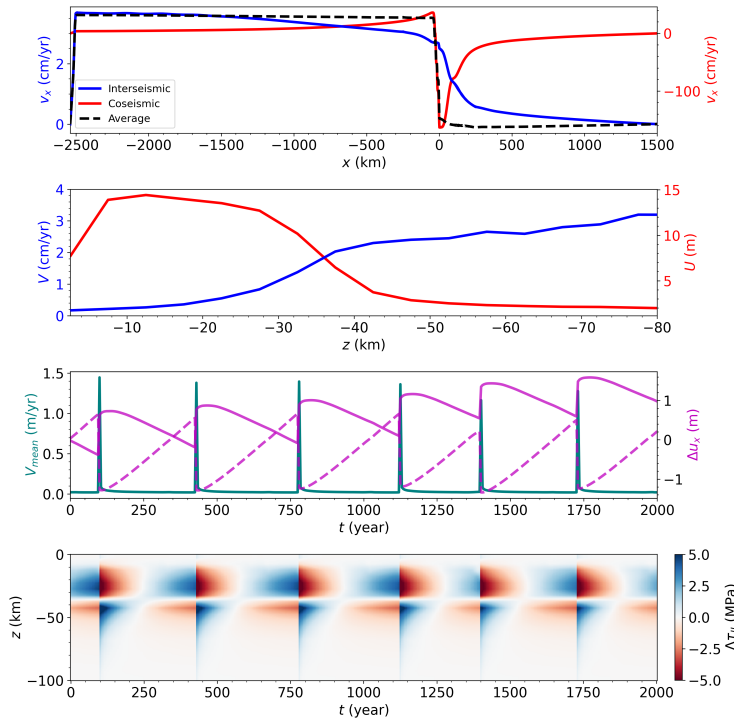

Figure 2.S6: Model outcomes of Model A3 (akin to Figure 2.2 in the manuscript). Symbols are the same as those in Figure 2.2.

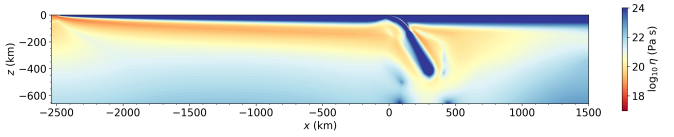

Figure 2.S7: Viscosities of Model A4.

Text S4. Additional 2.5D models

In the original model, the 2.5D models are expanded for 2 elements with a total width of 5 km in the third dimension. To verify the robustness of 2.5D models, we

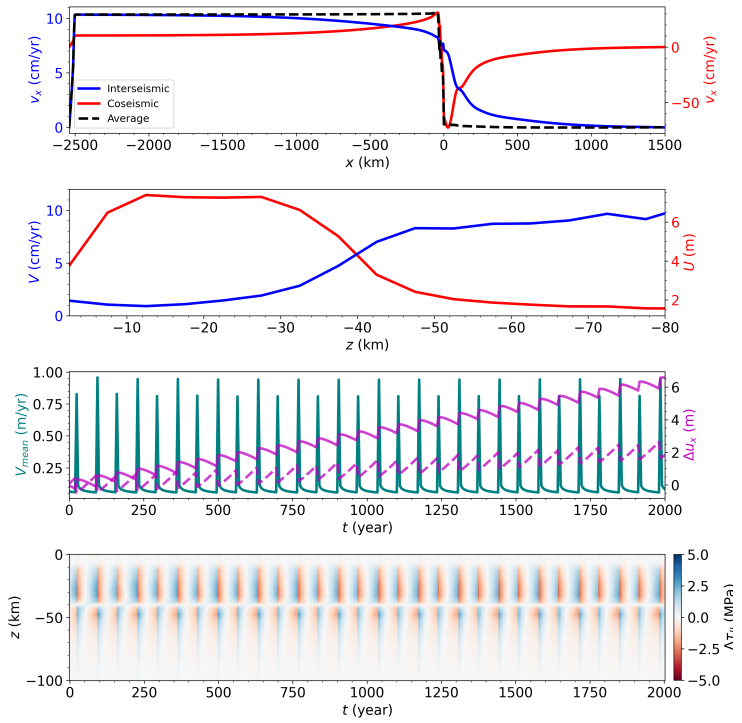

Figure 2.S8: Model outcomes of Model A4 (akin to Figure 2 in the manuscript). Symbols are the same as those in Figure 2.

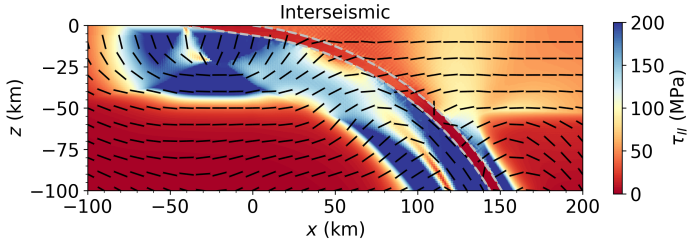

Figure 2.S9: Stress field near the megathrust after an interseismic time step. τ_{II} denotes the second invariant of the deviotoric stress tensor. Black bars indicate directions of principal compression axes.

conducted additional computations: (1) 4 along-strike elements with a total width of 5 km; (2) 2 along-strike elements with a total width of 5 km. The results (akin to Figure 4 in the manuscript) are shown in Figures 2.S12 and 2.S13, respectively. The curves of surface displacements and megathrust slips versus the along-strike length scale $\tilde{L}$ are identical for different numbers of along-strike elements and model widths, suggesting that these factors do not affect their relationship.

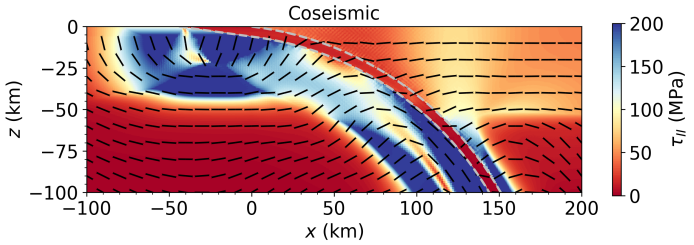

Figure 2.S10: Stress field near the megathrust after a coseismic time step. τ_{II} denotes the second invariant of the deviatoric stress tensor. Black bars indicate directions of principal compression axes.

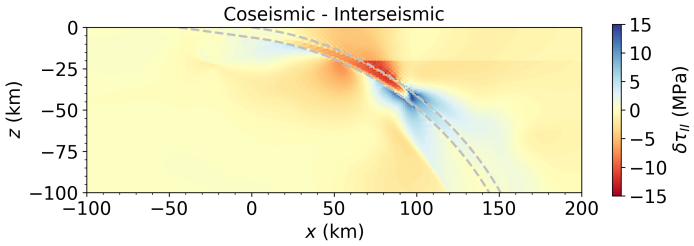

Figure 2.S11: Stress changes caused by a rupture event.

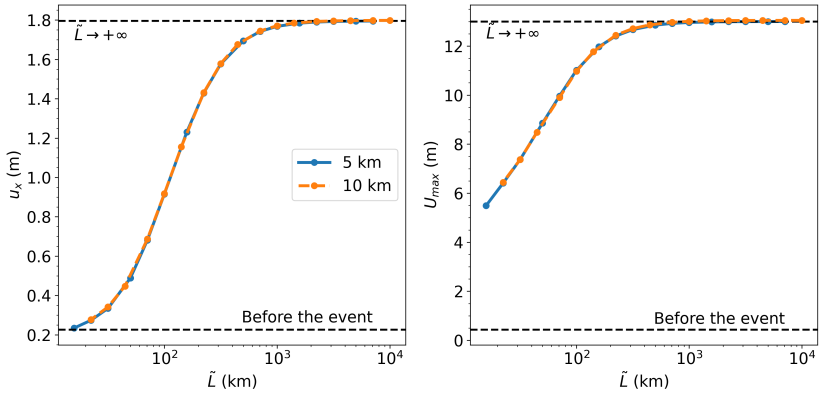

Figure 2.S12: Comparison of 2.5D models with different numbers of along-strike elements. Symbols are the same as those in Figure 2.4.

Text S5. Evolving boundary condition in the 2.5D model

Since Robin boundary conditions are not implemented in Underworld2, we developed an iterative framework as an alternative using an evolving Neumann boundary condition. For one step, the traction is imposed continuously on the front wall based on the solved velocity from the previous iteration:

$$\tau^a_{n+1} = \phi\tau^e_n + (1-\phi)\tau^a_n, \tag{2.S3}$$

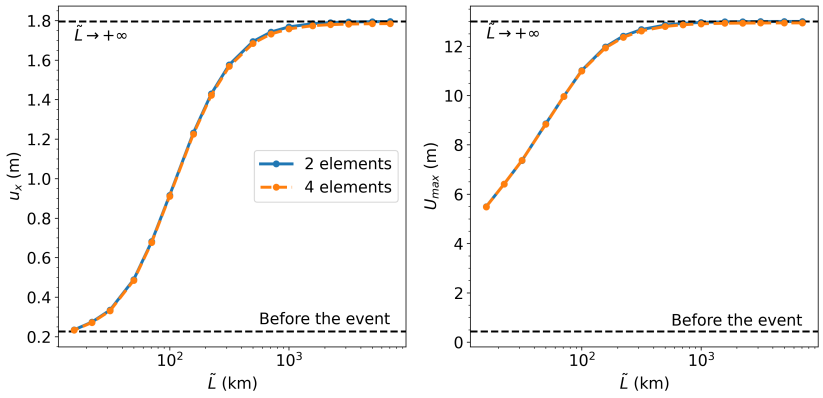

Figure 2.S13: Comparison of 2.5D models with different along-strike domain widths. Symbols are the same as those in Figure 2.4.

where τ_i^a is the applied traction in the i-th iteration, τ_i^e is the traction expected from the velocity field solved in the i-th iteration, and ϕ is a weighting coefficient. The coefficient ϕ smooths the spatially heterogeneous change of traction between iterations and stabilizes the update of this boundary condition, with $\phi = \min(\frac{L}{L_0}, 0.5)$, where $L_0 = 10^4$ km. The iteration terminates when the misfit between the applied traction and the expected traction calculated from the resulting velocity field is below 1%.

Text S6. Estimation of the rupture length scale

In elastic crack models where a crack in an elastic body is subjected to uniform stress changes, the relative displacements for all the crack modes follow elliptical distributions (Scholz, 2019). We use this analytical solution to approximate the slip distribution in the y direction along the strike of the plate boundary. The slip U as a function of y is given by:

$$U = \frac{U_0}{\tilde{L}}(\tilde{L}^2 - y^2)^{\frac{1}{2}}. \tag{2.S4}$$

U_0 is the maximum slip occurring at the center of the rupture where $y = 0$, and $\tilde{L}$: Half the rupture length, from the center to the tip where $U = 0$.

The gradient of slip U with respect to y is:

$$\frac{\mathrm{d}U}{\mathrm{d}y} = -\frac{U_0 y}{\tilde{L}(\tilde{L}^2 - y^2)^{\frac{1}{2}}}. \tag{2.S5}$$

Under the approximation that $y << \tilde{L}$, which is reasonable near the rupture center

($y \approx 0$), Equation 2.S5 simplifies to:

$$\frac{dU}{dy} \approx -\frac{U_0 y}{\tilde{L}^2}. \tag{2.S6}$$

In the model, a Robin boundary condition is imposed at $y = D$, where D is the domain width and $D << \tilde{L}$. It models the slip gradient as the difference between the slip at $y = D$ and the far-field slip (negligible compared with U_0 and assumed to be zero), divided by a length scale parameter L:

$$\left.\frac{dU}{dy}\right|_{y=D} = -\frac{U_0 D}{\tilde{L}^2} \approx -\frac{U_0}{L} \tag{2.S7}$$

This leads to the scaling relation between $\tilde{L}$ and L:

$$\tilde{L} = \sqrt{LD}. \tag{2.S8}$$

References

Alisic, Laura et al. (2012). "Multi-scale dynamics and rheology of mantle flow with plates". In: *Journal of Geophysical Research: Solid Earth* 117.B10.

Allison, Kali L and Eric M Dunham (2021). "Influence of shear heating and thermo-mechanical coupling on earthquake sequences and the brittle-ductile transition". In: *Journal of Geophysical Research: Solid Earth* 126.6, e2020JB021394.

Ammon, Charles J, Chen Ji, et al. (2005). "Rupture process of the 2004 Sumatra-Andaman earthquake". In: *science* 308.5725, pp. 1133–1139.

Ammon, Charles J, Thorne Lay, et al. (2011). "A rupture model of the 2011 off the Pacific coast of Tohoku Earthquake". In: *Earth, Planets and Space* 63, pp. 693–696.

Ampuero, J-P and Y Ben-Zion (2008). "Cracks, pulses and macroscopic asymmetry of dynamic rupture on a bimaterial interface with velocity-weakening friction". In: *Geophysical Journal International* 173.2, pp. 674–692.

Barbot, Sylvain, Nadia Lapusta, and Jean-Philippe Avouac (2012). "Under the hood of the earthquake machine: Toward predictive modeling of the seismic cycle". In: *Science* 336.6082, pp. 707–710.

Behr, Whitney M et al. (2022). "The effects of plate interface rheology on subduction kinematics and dynamics". In: *Geophysical Journal International* 230.2, pp. 796–812.

Bilek, Susan L and Thorne Lay (2018). "Subduction zone megathrust earthquakes". In: *Geosphere* 14.4, pp. 1468–1500.

Conrad, Clinton P and Bradford H Hager (1999). "Effects of plate bending and fault strength at subduction zones on plate dynamics". In: *Journal of Geophysical Research: Solid Earth* 104.B8, pp. 17551–17571.

Corbi, Fabio et al. (2017). "Controls of seismogenic zone width and subduction velocity on interplate seismicity: Insights from analog and numerical models". In: *Geophysical Research Letters* 44.12, pp. 6082–6091.

Dal Zilio, Luca, Ylona van Dinther, et al. (2018). "Seismic behaviour of mountain belts controlled by plate convergence rate". In: *Earth and Planetary Science Letters* 482, pp. 81–92.

Dal Zilio, Luca, Nadia Lapusta, et al. (2022). "Subduction earthquake sequences in a non-linear visco-elasto-plastic megathrust". In: *Geophysical Journal International* 229.2, pp. 1098–1121.

Den Hartog, SAM, AR Niemeijer, and Christopher J Spiers (2012). "New constraints on megathrust slip stability under subduction zone P–T conditions". In: *Earth and Planetary Science Letters* 353, pp. 240–252.

Di Toro, Giulio et al. (2011). "Fault lubrication during earthquakes". In: *Nature* 471.7339, pp. 494–498.

Dieterich, James H (1979). “Modeling of rock friction: 1. Experimental results and constitutive equations”. In: *Journal of Geophysical Research: Solid Earth* 84.B5, pp. 2161–2168.

Dinther, Y van et al. (2013). “The seismic cycle at subduction thrusts: Insights from seismo-thermo-mechanical models”. In: *Journal of Geophysical Research: Solid Earth* 118.12, pp. 6183–6202.

Farrington, RJ, L-N Moresi, and Fabio Antonio Capitanio (2014). “The role of viscoelasticity in subducting plates”. In: *Geochemistry, Geophysics, Geosystems* 15.11, pp. 4291–4304.

Faulkner, DR et al. (2011). “Stuck in the mud? Earthquake nucleation and propagation through accretionary forearcs”. In: *Geophysical Research Letters* 38.18.

Hanks, Thomas C and Hiroo Kanamori (1979). “A moment magnitude scale”. In: *Journal of Geophysical Research: Solid Earth* 84.B5, pp. 2348–2350.

Heuret, Arnauld et al. (2012). “Relation between subduction megathrust earthquakes, trench sediment thickness and upper plate strain”. In: *Geophysical Research Letters* 39.5.

Hu, Yan et al. (2016). “Asthenosphere rheology inferred from observations of the 2012 Indian Ocean earthquake”. In: *Nature* 538.7625, pp. 368–372.

Hyndman, Roy D, Makoto Yamano, and Dan A Oleskevich (1997). “The seismogenic zone of subduction thrust faults”. In: *Island Arc* 6.3, pp. 244–260.

Kanamori, Hiroo (1978). “Quantification of earthquakes”. In: *Nature* 271.5644, pp. 411–414.

Karato, Shun-ichiro and Patrick Wu (1993). “Rheology of the upper mantle: A synthesis”. In: *Science* 260.5109, pp. 771–778.

Kim, Young-Seog and David J Sanderson (2005). “The relationship between displacement and length of faults: a review”. In: *Earth-Science Reviews* 68.3-4, pp. 317–334.

King, Scott D (2016). “Reconciling laboratory and observational models of mantle rheology in geodynamic modelling”. In: *Journal of Geodynamics* 100, pp. 33–50.

Lambert, Valère, Nadia Lapusta, and Stephen Perry (2021). “Propagation of large earthquakes as self-healing pulses or mild cracks”. In: *Nature* 591.7849, pp. 252–258.

Lapusta, Nadia and Yi Liu (2009). “Three-dimensional boundary integral modeling of spontaneous earthquake sequences and aseismic slip”. In: *Journal of Geophysical Research: Solid Earth* 114.B9.

Li, Duo and Yajing Liu (2021). “Cascadia megathrust earthquake rupture model constrained by geodetic fault locking”. In: *Philosophical Transactions of the Royal Society A* 379.2196, p. 20200135.

Li, Jiyao, Donna J Shillington, et al. (2018). "Connections between subducted sediment, pore-fluid pressure, and earthquake behavior along the Alaska megathrust". In: *Geology* 46.4, pp. 299–302.

Li, Yida and Michael Gurnis (2023). "A simple force balance model of subduction initiation". In: *Geophysical Journal International* 232.1, pp. 128–146.

Liu, Yajing and James R Rice (2005). "Aseismic slip transients emerge spontaneously in three-dimensional rate and state modeling of subduction earthquake sequences". In: *Journal of Geophysical Research: Solid Earth* 110.B8.

Mansour, John A et al. (2020). "Underworld2: Python geodynamics modelling for desktop, HPC and cloud". In: *Journal of Open Source Software*.

Marone, Chris (1998). "Laboratory-derived friction laws and their application to seismic faulting". In: *Annual Review of Earth and Planetary Sciences* 26.1, pp. 643–696.

Moresi, L, Steve Quenette, et al. (2007). "Computational approaches to studying nonlinear dynamics of the crust and mantle". In: *Physics of the Earth and Planetary Interiors* 163.1-4, pp. 69–82.

Moresi, Louis, Frédéric Dufour, and H-B Mühlhaus (2002). "Mantle convection modeling with viscoelastic/brittle lithosphere: Numerical methodology and plate tectonic modeling". In: *Pure and applied Geophysics* 159, pp. 2335–2356.

Nishikawa, Tomoaki and Satoshi Ide (2014). "Earthquake size distribution in subduction zones linked to slab buoyancy". In: *Nature Geoscience* 7.12, pp. 904–908.

Ranalli, Giorgio (1995). *Rheology of the Earth*. Springer Science & Business Media.

Rice, James R (2006). "Heating and weakening of faults during earthquake slip". In: *Journal of Geophysical Research: Solid Earth* 111.B5.

Ruff, Larry J and Hiroo Kanamori (1980). "Seismicity and the subduction process". In: *Physics of the Earth and Planetary interiors* 23.3, pp. 240–252.

Saffer, Demian M and Harold J Tobin (2011). "Hydrogeology and mechanics of subduction zone forearcs: Fluid flow and pore pressure". In: *Annual Review of Earth and Planetary Sciences* 39, pp. 157–186.

Scholz, Christopher H (1982). "Scaling laws for large earthquakes: consequences for physical models". In: *Bulletin of the Seismological Society of America* 72.1, pp. 1–14.

– (2019). *The Mechanics of Earthquakes and Faulting*. Cambridge University Press.

Segall, Paul et al. (2010). "Dilatant strengthening as a mechanism for slow slip events". In: *Journal of Geophysical Research: Solid Earth* 115.B12.

Sobolev, Stephan V and Iskander A Muldashev (2017). "Modeling seismic cycles of great megathrust earthquakes across the scales with focus at postseismic phase". In: *Geochemistry, Geophysics, Geosystems* 18.12, pp. 4387–4408.

Stadler, Georg et al. (2010). “The dynamics of plate tectonics and mantle flow: From local to global scales”. In: *Science* 329.5995, pp. 1033–1038.

Sykes, Lynn R and Richard C Quittmeyer (1981). “Repeat times of great earthquakes along simple plate boundaries”. In: *Earthquake Prediction: An International Review* 4, pp. 217–247.

Tackley, Paul J (2000). “Self-consistent generation of tectonic plates in time-dependent, three-dimensional mantle convection simulations”. In: *Geochemistry, Geophysics, Geosystems* 1.8.

Thatcher, Wayne (1990). “Order and diversity in the modes of circum-Pacific earthquake recurrence”. In: *Journal of Geophysical Research: Solid Earth* 95.B3, pp. 2609–2623.

Thingbaijam, Kiran Kumar S, P Martin Mai, and Katsuichiro Goda (2017). “New empirical earthquake source-scaling laws”. In: *Bulletin of the Seismological Society of America* 107.5, pp. 2225–2246.

Ulrich, Thomas, Alice-Agnes Gabriel, and Elizabeth H Madden (2022). “Stress, rigidity and sediment strength control megathrust earthquake and tsunami dynamics”. In: *Nature Geoscience* 15.1, pp. 67–73.

Wang, Fan, S Shawn Wei, et al. (2024). “Fluids control along-strike variations in the Alaska megathrust slip”. In: *Earth and Planetary Science Letters* 633, p. 118655.

Wang, Kelin and Susan L Bilek (2014). “Invited review paper: Fault creep caused by subduction of rough seafloor relief”. In: *Tectonophysics* 610, pp. 1–24.

Wang, Kelin, Yan Hu, and Jiangheng He (2012). “Deformation cycles of subduction earthquakes in a viscoelastic Earth”. In: *Nature* 484.7394, pp. 327–332.

Wells, Donald L and Kevin J Coppersmith (1994). “New empirical relationships among magnitude, rupture length, rupture width, rupture area, and surface displacement”. In: *Bulletin of the seismological Society of America* 84.4, pp. 974–1002.

Wirth, Erin A et al. (2022). “The occurrence and hazards of great subduction zone earthquakes”. In: *Nature Reviews Earth & Environment* 3.2, pp. 125–140.

Yang, Haibin et al. (2023). “Numerical Modeling of Earthquake Cycles Based On Navier-Stokes Equations With Viscoelastic-Plasticity Rheology”. In: *Geochemistry, Geophysics, Geosystems* 24.9, e2023GC010872.

Ye, Lingling, Hiroo Kanamori, and Thorne Lay (2018). “Global variations of large megathrust earthquake rupture characteristics”. In: *Science advances* 4.3, eaao4915.

Zhong, Shijie and Michael Gurnis (1995). “Mantle convection with plates and mobile, faulted plate margins”. In: *Science* 267.5199, pp. 838–843.

Zhong, Shijie, Michael Gurnis, and Louis Moresi (1998). “Role of faults, nonlinear rheology, and viscosity structure in generating plates from instantaneous mantle flow models”. In: *Journal of Geophysical Research: Solid Earth* 103.B7, pp. 15255–15268.

Chapter 3

MULTI-SCALE DYNAMICS OF SUBDUCTION ZONES: FROM LONG-TERM PLATE MOTIONS TO GREAT MEGATHRUST EARTHQUAKES

Abstract

Understanding the link between background plate motions and great earthquake occurrence is fundamental to constraining Earth's rheological properties and assessing seismic hazards. We developed a cross-scale subduction model that integrates tectonic forces with a nonlinear visco-elasto-plastic rheology and self-consistently generates long-term plate convergence and rapid coseismic slip. Nominally, the computed long-term plate velocity of several cm/yr, asthenosphere viscosity of $\sim 10^{19}$ Pa·s, coseismic slip of $\sim$ 25 m coseismic slip, and recurrence intervals of several hundred years, are consistent with observational constraints. The relationship between earthquake magnitude and dimension is determined by varying along-strike (L) and along-dip (W) rupture sizes in computations. We find that while magnitudes of smaller events are jointly controlled by along-dip and along-strike rupture sizes, magnitudes of the largest megathrusts are dominantly controlled by the along-strike rupture length. By systematically varying rheological and structural parameters, we examine their influence on plate motions and coseismic displacements. Megathrust friction, the incoming plate age and the seismogenic zone dip angle play a dual role in modulating both long- and short-term deformation. We show that the recurrence and magnitude of great megathrust earthquakes are the result of an intricate interaction between slab buoyancy, plate geometry and rheological structures.

3.1 Introduction

Despite their vastly different spatial and temporal scales, plate motions and great earthquakes are both surface expressions of Earth's internal dynamics and together provide constraints on the underlying rheological structure. Slow motions of large tectonic plates are viscously dominated and arise from a balance between driving forces, primarily the negative buoyancy of subducting slabs, and resisting forces such as mantle viscous shear, plate bending, and inter-plate friction (Behr et al., 2022; Buffett, 2006; Conrad and Hager, 1999; Garel et al., 2014; Scholz and Campos, 2012; Zhong, Gurnis, and Moresi, 1998). These forces are regulated by

constitutive properties that vary with depth, temperature, composition and strain rate in Earth's interior (Alisic et al., 2012; Li and Gurnis, 2023; Turcotte and Schubert, 2002). In contrast, seismic cycles characterized by gradual interseismic loading and rapid coseismic slip of earthquakes are classically explained by the elastic rebound theory (Reid, 1910). The largest events ($M_w > 8$) generally occur on subduction zone megathrust faults and many of them recur quasi-periodically on time scales of centuries (Bilek and Lay, 2018; Kanamori, 2014; Moernaut et al., 2018; Philibosian and Meltzner, 2020). Recurrence intervals and magnitudes of these great megathrust earthquakes are modulated by tectonic loading that delivers stresses as well as megathrust properties that directly influence the fault strength, including material heterogeneity, asperity distribution, fluid content and thermal structure (Heuret et al., 2012; Hyndman, Yamano, and Oleskevich, 1997; Scholz and Campos, 2012; Wang and Bilek, 2014; Wirth et al., 2022).

Subduction zones simultaneously accommodate quasi-steady plate convergence and host Earth's largest earthquakes, and these multi-scale processes are fundamentally interconnected (Bilek and Lay, 2018; Wirth et al., 2022). The accumulation of stress along plate boundaries is ultimately driven by plate motions due to slab pull. To date, observational records do not support a simple correlation between earthquake recurrence and key characteristics of subduction zones including plate age, convergence rate, megathrust geometry or inter-plate coupling (Wirth et al., 2022). The influence of subduction parameters on the space–time variability of great earthquake occurrence can be complicated by local structural and thermomechanical controls as well as local megathrust conditions. Great earthquakes occur when the stress stored on the megathrust reaches a threshold and is suddenly released, which in turn causes abrupt changes in plate motions over a broad scale (Graham, Loveless, and Meade, 2018; Tregoning et al., 2013; Wang and Shen, 2020). Triggered temporal variations are superimposed onto the background deformation and stress and evolve throughout seismic cycles (Wang, Hu, and He, 2012). The background and transient deformation patterns are governed by a visco-elasto-plastic constitutive relationship across multiple spatial and temporal scales and can show different sensitivities to specific rheological parameters (Fang, Gurnis, and Mallick, 2025; Hu et al., 2024; Sun, Wang, and He, 2024). However, they are commonly treated in separate geophysical models for either plate motions (e.g., Hager and O'Connell (1981), Zhong and Gurnis (1995), and Stadler et al. (2010)) or earthquakes (e.g., Lapusta and Liu (2009), Barbot, Lapusta, and Avouac (2012), and Jiang et al. (2022)). A unified cross-scale framework is required to explicitly draw the link

between these processes and rheological properties that control them.

Bridging the time-scale gap remains a central challenge in self-consistent computation of large-scale plate motions and great earthquakes within a single unified model. Previous studies have incorporated megathrust earthquakes into two-dimensional (2D) geodynamic models using one-way coupling approaches (e.g., Dinther et al. (2013), Sobolev and Muldashev (2017), and Yang et al. (2023)). With imposed plate velocities, these models capture the main features of rapid coseismic deformation and provide valuable insight into the interplay between rupture processes and regional tectonics. However, the prescribed velocity boundary conditions may not be fully consistent with the rheology of the system. This limitation is overcome with an improved subduction model driven by internal buoyancy forces that simultaneously produces both long-term plate motions and short-term perturbations from great megathrust earthquakes (Fang, Gurnis, and Lapusta, 2024). The 2D cross-section computations cannot adequately capture finite-length ruptures along the plate boundary, while full three-dimensional (3D) cross-scale models over realistic domains remain computationally expensive for resolving both plate-motion and seismic-cycle timescales over realistic domains. We further introduce a 2.5-dimensional (2.5D) approach with a Robin boundary condition that represents the resistance on the modeled ruptured segment from adjacent non-ruptured segments, and reveals the influence of along-strike rupture size on coseismic slip behavior.

We apply this cross-scale approach to a generic subduction model that self-consistently integrates internal buoyancy forces, nonlinear visco-elasto-plastic rheology of the lithosphere and mantle, and friction along the megathrust. With the 2.5D approach, we efficiently investigate the relationship between rupture dimensions and earthquake magnitudes. By systematically varying rheological parameters, megathrust geometry and thermal structure, we quantify how these factors jointly regulate both quasi-steady background motion and transient coseismic deformation within a unified framework. We demonstrate that the long-term and coseismic deformation patterns are modulated by multi-scale rheological and structural factors. These findings provide a physically consistent framework for interpreting both long-term plate velocities and coseismic displacements.

3.2 Methods

Governing equations and constitutive relationship

We solve the incompressible Stokes equations for velocity, v, and pressure, p, using the open-source finite-element code Underworld2 (Mansour et al., 2020). Under the Boussinesq approximation, the system includes the conservation of mass

$$\nabla \cdot v = 0 \tag{3.1}$$

and momentum

$$\nabla \cdot \tau - \nabla p = \mathrm{Ra} T e_z, \tag{3.2}$$

where τ is the deviatoric stress tensor, Ra is the Rayleigh number, T is temperature, and e_z is the unit vector in the vertical direction. The deviatoric stress is related to velocity and strain rate ($\dot{\varepsilon} = \frac{1}{2}[\nabla v + (\nabla v)^T]$) through the constitutive relationship of the medium. For viscous flow with viscosity η, the relationship is given by $\tau = 2\eta\dot{\varepsilon}$, and the equation of motion (Eq. 3.2) becomes:

$$\nabla \cdot (2\eta\dot{\varepsilon}) - \nabla p = \mathrm{Ra} T e_z. \tag{3.3}$$

The lithosphere and mantle are viscously dominated over long time scales while showing an elastic response over short time-scales. This dual behavior can be approximated by a Maxwell visco-elastic material

$$\dot{\varepsilon} = \dot{\varepsilon}_v + \dot{\varepsilon}_e = \frac{\tau}{2\eta} + \frac{\dot{\tau}}{2G}, \tag{3.4}$$

in which the strain rate, $\dot{\varepsilon}$, is the sum of a viscous component, $\dot{\varepsilon}_v$, and an elastic component, $\dot{\varepsilon}_e$. G is the shear modulus and $\dot{\tau}$ is the stress rate, approximated by a backward difference

$$\dot{\tau} \approx \frac{\tau - \check{\tau}}{\Delta t}, \tag{3.5}$$

where τ is the deviatoric stress at the current time step (t), Δt is the time step size, and $\check{\tau}$ is the deviatoric stress at the last time step ($t - \Delta t$). Equation 3.4 can therefore be transformed into:

$$\tau = 2\eta_{ve}\dot{\varepsilon}_{ve}, \tag{3.6}$$

where $\eta_{ve} = (\eta G \Delta t)/(\eta + G\Delta t)$ and $\dot{\varepsilon}_{ve} = \dot{\varepsilon} + \check{\tau}/(2G\Delta t)$.

Plastic yielding is incorporated to approximate the megathrust behavior as well as plastic failure in the bulk. The second invariant of the deviatoric stress tensor, τ_{II}, is limited by an assumed yield stress, τ_y ($\tau_{II} \leq \tau_y$), which modifies Equation 3.6 to

$$\tau = 2\eta_{vep}\dot{\varepsilon}_{ve}, \tag{3.7}$$

with an effective visco-elasto-plastic viscosity

$$\eta_{vep} = \min\left(\eta_{ve}, \frac{\tau_y}{2(\dot{\varepsilon}_{ve})_{II}}\right) = \min\left(\frac{\eta G\Delta t}{\eta + G\Delta t}, \frac{\tau_y}{2(\dot{\varepsilon}_{ve})_{II}}\right). \tag{3.8}$$

Substituting Equation 3.7 into Equation 3.2 leads to:

$$\nabla \cdot (2\eta_{vep}\dot{\varepsilon}) - \nabla p = \mathrm{Ra}Te_z - \nabla \cdot (\eta_{vep}\frac{\check{\tau}}{G\Delta t}), \tag{3.9}$$

which can be computed with the original solver infrastructure for Equation 3.3 without major modifications (Farrington, Moresi, and Capitanio, 2014; Yang et al., 2023).

Model setup and rheology

We begin with a 2D subduction model that lies in the x-z plane, perpendicular to the plate boundary and includes the entire incoming plate from ridge to trench. The domain has dimensions of 4040 km × 660 km (Fig. 3.1a) and is discretized with 1024×256 quadrilateral, bilinear elements. The mesh resolution is 1.2 km near the 6-km-wide megathrust shear zone and 5 km in the far field. All domain boundaries are free-slip, and the deformation is primarily driven by the negative buoyancy of the slab. The thermal structure is prescribed following Fang, Gurnis, and Lapusta (2024) (Fig. 3.1a).

The rheology is jointly governed by creeping, elastic and plastic processes, with key parameters listed in Table 1. The viscosity is determined by a composite creep law with both dislocation and diffusion creep (Karato and Wu, 1993; Ranalli, 1995), both parameterized as:

$$\eta_{disl,diff} = \omega A^{-\frac{1}{n}}\dot{\epsilon}_{II}^{\frac{1-n}{n}} \exp\left(\frac{E + PV}{nRT}\right), \tag{3.10}$$

where $\eta_{disl,diff}$ denotes dislocation or diffusion creep viscosity, ω is a weakness factor along the megathrust, A is a prefactor, n is the stress exponent (3.5 for dislocation creep and 1 for diffusion creep), R is the gas constant, E is the activation energy, V is the activation volume, and P is approximated by the lithostatic stress.

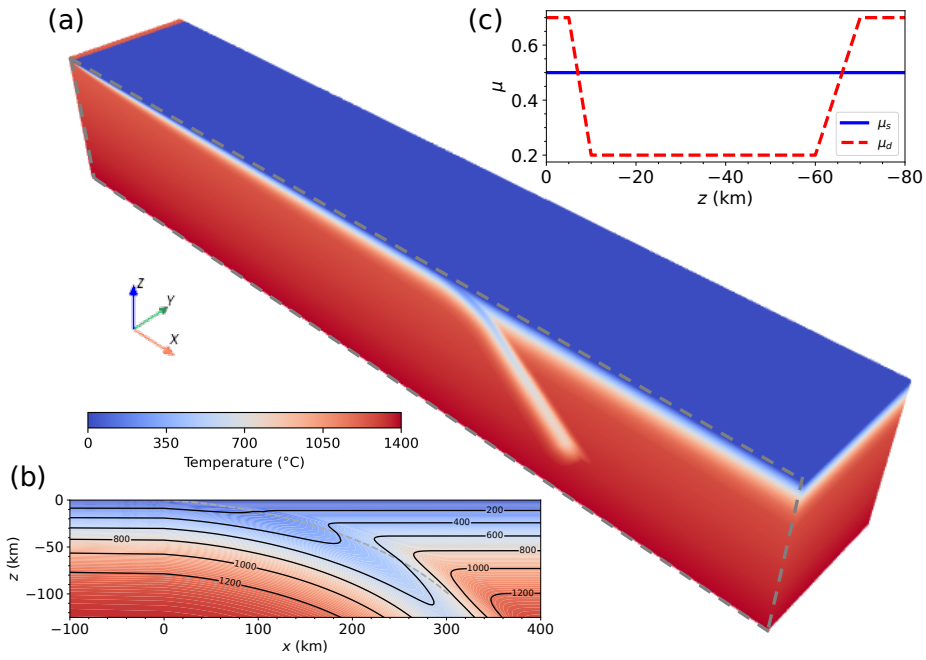

Figure 3.1: (a) Thermal structure of the model. The 2D model lies in the x–z plane. The 2.5D model expands the 2D domain by two elements to a thickness of 5 km. The 3D model for validation of the 2.5D approximation spans 640 km in the along-strike (y) direction, with along-strike variations neglected. (b) Enlargement of the thermal structure in the plate boundary area. (c) Friction parameters μ_s and μ_d versus depth along the megathrust shear zone.

The shear modulus is 30 GPa for the shear zone, top 6 km of the incoming plate and 20 km of the overriding plate, consistent with typical crustal values (Brocher, 2005), and 60 GPa for the bulk upper mantle. Plastic yielding follows the Drucker-Prager criterion, in which the second invariant of the deviatoric stress, τ_{II}, is limited by a yield stress given by:

$$\tau_y = C + \mu P \left(1 - \lambda_p\right), \tag{3.11}$$

where C is the cohesion, μ is the friction coefficient, and λ_p is a pore pressure factor. Fluid overpressure in the megathrust is approximated with a fixed pore pressure factor $\lambda_p = 0.95$ within the shear zone shallower than 60 km, which decreases linearly from 0.95 to 0 from 60 to 80 km.

Imposed earthquake and 2.5-dimensional (2.5D) approach

Earthquakes are imposed by reducing the friction in a portion of the megathrust shear zone, which is defined as the seismogenic zone. We first set the friction

coefficient to the interseismic friction, μ_s, throughout the megathrust shear zone and solve the Stokes system with a large time step size of 4×10^4 years until a steady state is reached, representing the long-term plate motion. With the initial stress computed from the long-term behavior, the model is transitioned to short-timescale computations with a reduced time step size of 1 year. The friction coefficient is slightly increased in the megathrust shear zone to create a critical pre-seismic state and subsequently dropped to the coseismic friction μ_d ($\mu_d < \mu_s$ in the seismogenic zone) to generate a rupture event (an "earthquake"). The friction coefficient in updip and downdip portions is simultaneously increased ($\mu_d > \mu_s$).

To account for along-strike resistance from adjacent non-ruptured segments during an earthquake, the 2D model domain is expanded in the along-strike (y) direction by 2 elements, forming a thin 2.5D model with a thickness of 5 km (Fang, Gurnis, and Lapusta, 2024). Assuming the 2.5D model domain is located at the rupture center, a shear traction is applied to the front wall to represent the resistance due to the shear strain between the rupture zone and the non-ruptured distal segment outside the domain. The expected shear traction is proportional to the difference in co-seismic displacements and inversely proportional to an along-strike length scale λ:

$$\tau^e = -2G\varepsilon^{bc} = -G\frac{u - u^{far}}{\lambda} = -G\Delta t\frac{v - v^{far}}{\lambda}, \tag{3.12}$$

where τ^e is the traction on the front wall, G is the shear modulus, ε^{bc} is the shear strain, $u - u^{far}$ and $v - v^{far}$ denotes the displacement and velocity difference from the distal reference, τ^e_{xy} depends on $v_x - v_x^{far}$, τ^e_{zy} depends on $v_z - v_z^{far}$, and $\tau^e_{yy} = 0$. The detailed implementation of this boundary condition is described in Text S1.

The parameter λ controls the gradient of displacements at the front wall and ultimately the effective along-strike resistance. Its value is usually smaller than half of the real rupture length because slip decays nonlinearly in the along-strike direction. If we take an elliptical slip distribution along strike (Scholz, 2019), the real rupture length L can be approximated by:

$$L \approx 2\sqrt{\lambda D}, \tag{3.13}$$

where D is the thickness of the 2.5D domain (D = 5 km). The derivation is shown in Text S2.

The 2.5D approach substantially reduces the computational cost while still effectively capturing the influence of rupture dimensions on slip behavior. We have also

conducted a set of full 3D computations to validate the proposed 2.5D approach, in which the model domain extends 640 km in the along-strike (y) direction with 256 elements and the rupture length L is directly controlled. The 3D computations assume different along-strike distributions of stress drop, ranging from constant (rectangular), constant near the center with linear decay toward the edge (trapezoid), to fully linearly decaying (triangular), and the megathrust slip is positively correlated with the integrated stress drop over the ruptured area. When L is varied, the megathrust slip predicted by the 2.5D model falls between 3D results obtained for the rectangular, trapezoid and triangular stress drop distributions (Fig. 3.2). The conversion between L and λ in the 2.5D approximation assumes uniform stress drop in a homogeneous medium, which does not fully align with material heterogeneity and finite rupture width in a subduction zone. Although deviations arise from this complexity, the broad consistency of the results confirms that the implementation of the 2.5D model provides an efficient representation of the influence of L and resulting along-strike resistance.

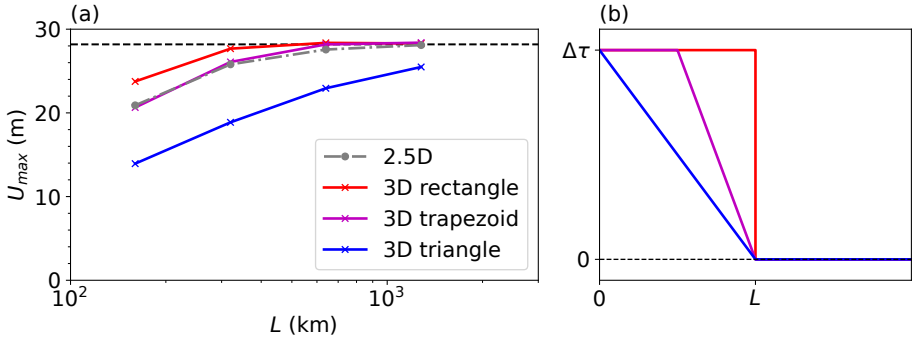

Figure 3.2: (a) Comparison of coseismic slip along the megathrust shear zone in the 2.5D model and 3D models with different stress drop distributions shown in (b). (b) Along-strike distributions assumed in the 3D models.

Varied parameters

For computations in the 2.5D setup, we first focus on the influence of rupture dimensions and vary: (1) the parameter λ in Equation 3.12, which can be converted to the rupture length L; (2) the downdip limit depth of the rate-weakening portion of the megathrust, h, which determines the rupture width W. We then investigate the sensitivity of multi-scale model behavior to rheological properties and vary the following parameters: (1) ω_{disl}, weakness factor of the dislocation creep law in the bulk upper mantle; (2) $\tau_{y,max}$, maximum yield stress, representing the yield stress

of most of the upper mantle, except the shallowest portion; (3) G_b, shear modulus of the bulk upper mantle; (4) G_{sz}, shear modulus of the megathrust shear zone; (5) $\mu_{d,mid}$, dynamic friction in the rate-weakening portion of the megathrust shear zone; (6) μ_s, static friction in the megathrust shear zone. In each case, only one parameter is perturbed relative to the reference model, and the rupture dimension parameters λ and h are kept fixed. Finally, we examine the influence of structural controls on plate velocities and coseismic displacements by varying the age of the incoming plate, A_i, and the average dip angle of the seismogenic zone, Θ.

Table 3.1: Parameters of the reference model.

Quantity	Symbol	Unit	Bulk value	Shear zone value
Dislocation creep				
Exponent	n	—	3.5	2.3
Weakness factor	ω	—	1	1
Prefactor	A	$\mathrm{Pa}^{-n}\cdot\mathrm{s}^{-1}$	2.83×10^{-16}	3.13×10^{-17}
Activation energy	E	$\mathrm{J}\cdot\mathrm{mol}^{-1}$	5.32×10^{6}	1.54×10^{6}
Activation volume	V	$\mathrm{m}^3\cdot\mathrm{mol}^{-1}$	1.06×10^{-5}	0
Diffusion creep				
Exponent	n	—	1.0	—
Weakness factor	ω	—	1	—
Prefactor	A	$\mathrm{Pa}^{-n}\cdot\mathrm{s}^{-1}$	1.40×10^{-11}	—
Activation energy	E	$\mathrm{J}\cdot\mathrm{mol}^{-1}$	3.00×10^{6}	—
Activation volume	V	$\mathrm{m}^3\cdot\mathrm{mol}^{-1}$	6.00×10^{-6}	—
Elasticity				
Shear modulus	G	GPa	60	25
Plastic yielding				
Cohesion	C	MPa	100	10
Interseismic friction	μ_s	—	0.6	0.6
Coseismic friction	μ_d	—	0.6	0.2 – 0.7
Pore pressure factor	λ	—	0	0 – 0.95
Maximum yield stress	τ_{max}	MPa	200	200

3.3 Results

Reference model

In the 2.5D reference model with λ = 5120 km (L = 320 km), the long-term surface velocity is nearly uniform at $\approx$ 5 cm/yr across the incoming plate, and the long-term slip rate along the megathrust shear zone matches the convergence rate at all depths. When the model transitions to the short-term stage with a reduced time step size, elastic deformation becomes increasingly prominent. Prior to a rupture event, surface velocities on both the incoming and overriding plates are horizontally

compressive. Near the trench, the landward motion is up to 0.5 cm/yr lower than the average plate velocity on the incoming plate, while the overriding plate shows substantial landward motion of > 1 cm/yr within ~300 km of the trench. The megathrust is locked at shallow depth but creeps at the convergence rate in the deeper portion with higher temperature. When an earthquake occurs, the compressive velocity pattern rapidly switches to extension in the vicinity of the plate boundary, as accumulated strain in the locked zone is released and produces abrupt coseismic slip up to 26 m. The resulting coseismic displacements are validated through comparison with analytical solutions based on the Okada formulation Okada, 1985 as well as models with spontaneous slip instabilities (Text S3 and Fig. S1). All other cases with different parameters show broadly similar long-term, pre-seismic and co-seismic deformation patterns to the reference model (Fig. 3.3).

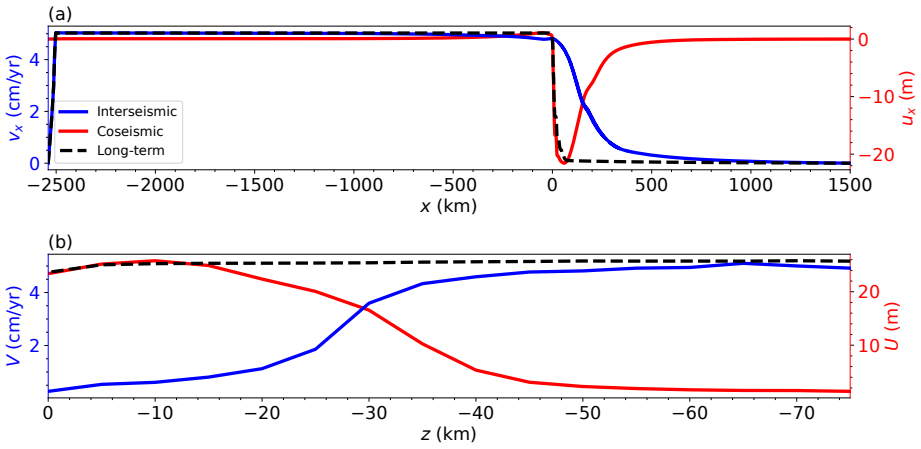

Figure 3.3: (a) Interseismic velocities (blue solid), coseismic displacements (red solid), and long-term (black dashed) velocities along the surface, v_x. (b) Interseismic (blud solid) and long-term (black dashed) slip velocities, V, together with coseismic slip (red solid), U, along the megathrust.

Influence of rupture dimensions

Rupture dimensions in both the along-dip and along-strike directions are key factors modulating the earthquake magnitude and slip behavior. The influence of along-dip rupture width W is examined by varying the downdip limit depth, h, in the 2.5D model while keeping the parameter $\lambda = 5120$ km ($L = 320$ km) fixed (Fig. 3.4). In cases with $h \geq 46$ km, rupture extends to a maximum along-dip width of 150 km, which is determined by brittle-ductile transition instead of the transition between rate-weakening and rate-strengthening friction at the depth of h. In the deeper

and warmer downdip portion of the megathrust, stresses are primarily governed by viscous flow and remain below the yield stress throughout the seismic cycle. Consequently, expanding coseismic friction weakening zone below the transition depth does not trigger additional stress drop in downdip areas or further enhance coseismic deformation. These results indicate that thermal structure of the megathrust interface places a primary constraint on the maximum along-dip rupture width, although the downdip limit may be influenced by other processes such as mantle serpentinization before the critical temperature is reached (Hyndman, Yamano, and Oleskevich, 1997; Oleskevich, Hyndman, and Wang, 1999). Rupture during an earthquake may also involve only a smaller asperity in the friction weakening regime rather than the entire seismogenic zone. Decreasing h from 46 km to 16 km, corresponding to a decrease in W from 150 km to 49 km, reduces the maximum coseismic slip from 28 m to 5 m and also results in smaller and less extensive coseismic displacements near the megathrust (Fig. 3.4).

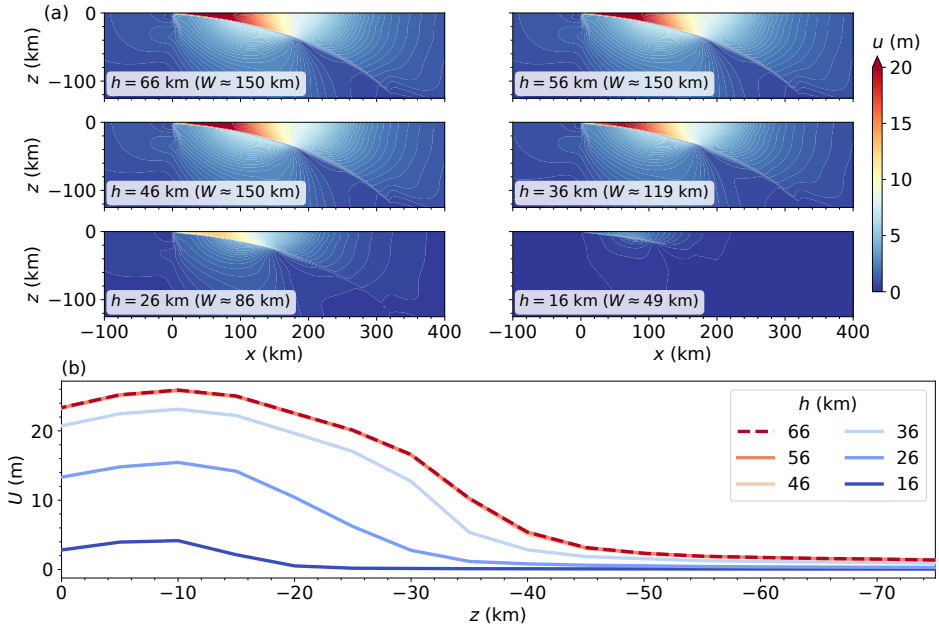

Figure 3.4: Coseismic displacements near the plate boundary (a) and coseismic slip along the megathrust shear zone (b) for different along-dip rupture width (W).

Adjusting the parameter λ in the boundary condition effectively modifies the along-strike rupture length L. The results show a clear decrease in coseismic displacements near the plate boundary as L decreases (Fig. 3.5a). When L greatly exceeds the maximum along-dip rupture width of $\sim$ 150 km in the reference model, the megathrust slip distribution converges to the 2D results corresponding to an infinite rupture

length (Fig. 3.5b). When we fix h = 66 km to allow for the largest W, decreasing L leads to reduced coseismic slip at all depths, with the maximum slip decreasing from 28 m for L = 1280 km to < 10 m for L = 40 km. When the along-dip rupture width W is smaller, the critical range of L over which coseismic slip significantly changes shifts to smaller values. Cases with $L << W$ serve to illustrate the conceptual understanding of the influence of rupture dimensions, as in realistic rupture events the along-strike and along-dip rupture dimensions tend to scale more proportionally when the seismogenic zone is not fully saturated.

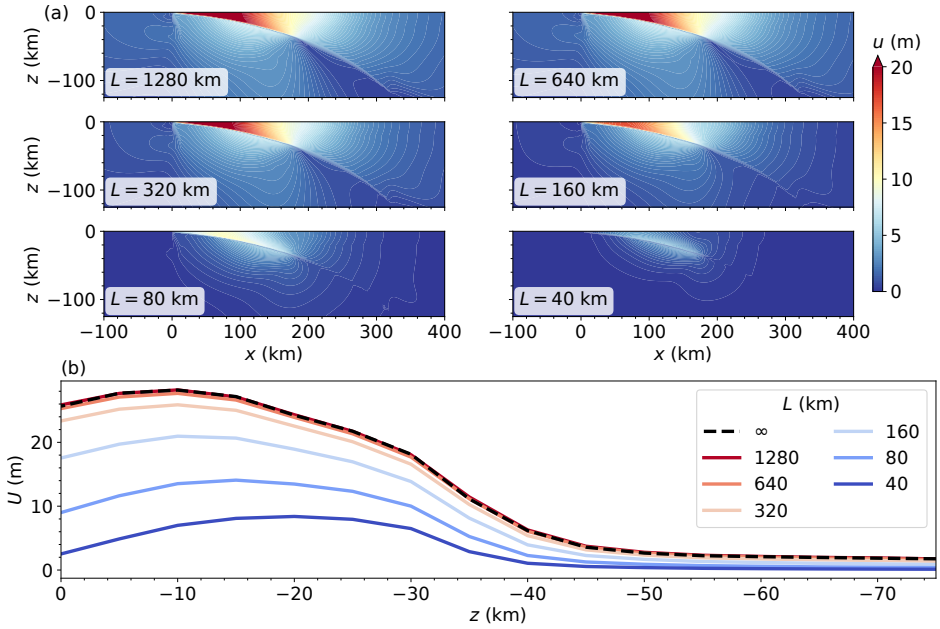

Figure 3.5: Coseismic displacements near the plate boundary (a) and coseismic slip along the megathrust shear zone (b) for different along-strike rupture length (L).

The earthquake magnitude is jointly determined by rupture dimensions and coseismic slip along the megathrust (Fig. 3.6). As either L or W increases, there is a commensurate increase in the effective seismic moment and corresponding magnitude. For smaller earthquakes that do not rupture the full width of the seismogenic zone, the increase in moment magnitude results from the combined effects of larger rupture sizes and coseismic slip controlled by both L and W. When W saturates at 150 km and the entire seismogenic width is ruptured, the coseismic slip approaches the 2D results and no longer increases significantly with L. In this regime, the along-strike rupture length L becomes the dominant factor that controls earthquaake magnitude. Although we have not considered the heterogeneous structural and rheological controls, the scaling relationship between earthquakes moment

magnitude and along-strike rupture length predicted by this model is largely consistent with observations of megathrust events compiled by Thingbaijam, Mai, and Goda (2017) (Fig. 3.6).

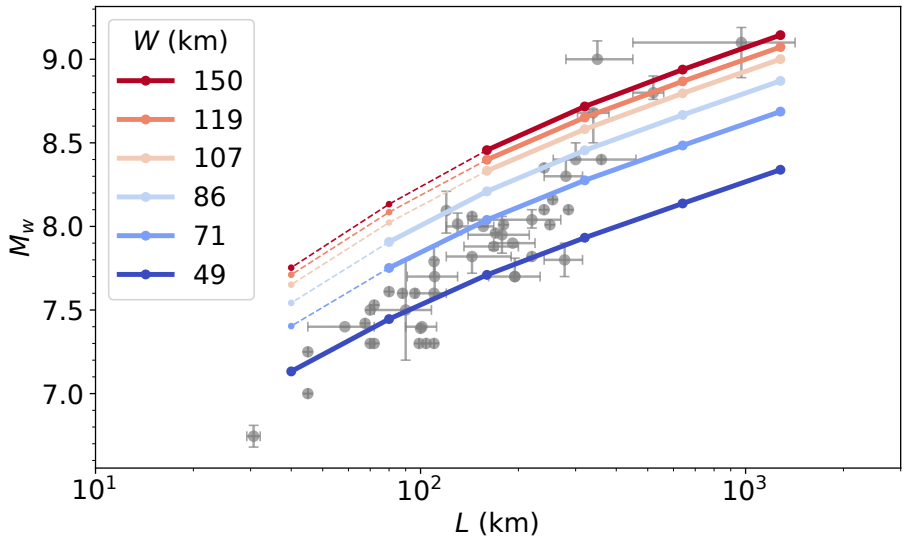

Figure 3.6: The relationship between the magnitude and along-strike rupture length (L) of earthquakes. Each line assumes a fixed along-dip rupture width (W), and the dashed segments indicate less realistic cases in which $L < W$. Gray dots with error bars are estimates for large megathrust events, compiled by Thingbaijam, Mai, and Goda (2017).

Influence of rheological properties

When creep, elastic and frictional parameters are varied relative to the reference model, the long-term plate velocity and coseismic slip respond differently (Fig. 3.7a). Assuming the elastic strain stored in the seismogenic zone is fully released during an earthquake, the recurrence interval of megathrust earthquakes can be approximated by dividing the average coseismic slip by the long-term velocity. This assumption is supported by our previous model with spontaneously generated great earthquakes (Fang, Gurnis, and Lapusta, 2024) and additional computations shown in Text S1 and Fig. 3.S1. Because both long-term plate motion and coseismic deformation depend on the rheological properties of the system, the recurrence interval is also influenced by these parameters in different ways (Fig. 3.7b).

The weakness factor of the dislocation creep law, ω_{disl}, and the maximum yield stress, $\tau_{y,max}$, strongly influence the long-term plate velocity (Figs. 3.8 and 3.S2). These parameters determine the magnitude of the important resisting forces that

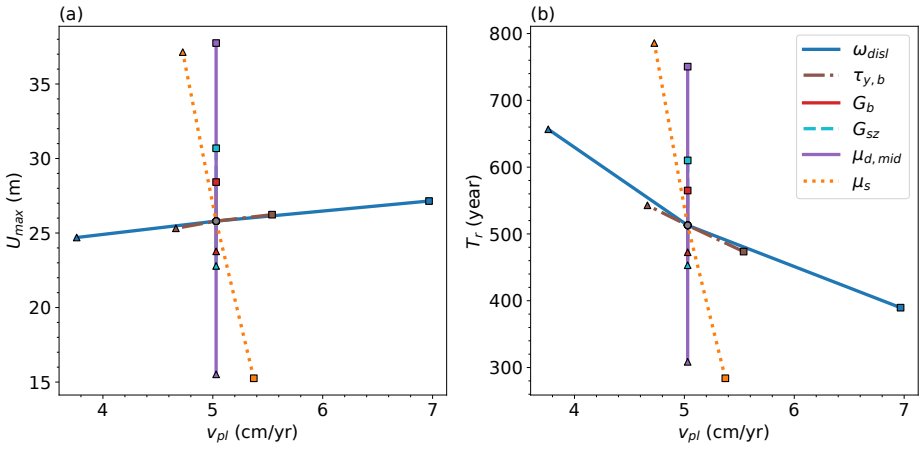

Figure 3.7: Maximum coseismic slip, U_{max}, and estimated recurrence interval, T_r, versus long-term convergence rate, v_{pl}, for cases with varied rheological parameters. The circle where different lines intersect denote the reference case, and each line shows results when one single parameter is perturbed. Squares indicate results for smaller parameter values, and triangles indicate results for larger parameter values. The dot with error bars represents results from the SE model.

oppose plate motions in the mantle below tectonic plates and within the hinge zone (i.e., where the plate bends). In the reference case with $\omega_{disl} = 1$ and $\tau_{y,max} = 200$ MPa, the incoming plate advances at a velocity of 5 cm/yr. Perturbations in ω_{disl} shift the upper mantle viscosity (Fig. 3.8a) and significantly affect the plate motion (Fig. 3.8b), as expected in a highly nonlinear system. Increasing ω_{disl} to 1.1 broadly raises the mantle viscosity and slows the plate to 3.8 cm/yr, while decreasing ω_{disl} to 0.9 reduces mantle viscosity and accelerates the plate to 7 cm/yr. The parameter $\tau_{y,max}$ modulates the plate motion by influencing the viscous dissipation in the hinge zone of the incoming plate. When the weakness factor ω_{disl} remains unchanged at 1, the plate velocity is 4.6 cm/yr for a higher $\tau_{y,max}$ of 240 MPa and 5.6 cm/yr for a lower $\tau_{y,max}$ of 160 MPa. Despite variations in viscosity, coseismic deformation remains largely similar across these cases with variations in ω_{disl} and $\tau_{y,max}$. The maximum coseismic slip in the megathrust shear zone increases slightly when ω_{disl} or $\tau_{y,max}$ is reduced, and vice versa, which possibly reflects postseismic deformation averaged into the 1-year coseismic step. The estimated recurrence interval of great earthquakes is thus approximately inversely proportional to the long-term plate velocity.

By varying elastic properties (Figs. 3.S3 and 3.S4), we find that the shear modulus of the megathrust shear zone (G_{sz}) or the bulk upper mantle (G_b) strongly regulates

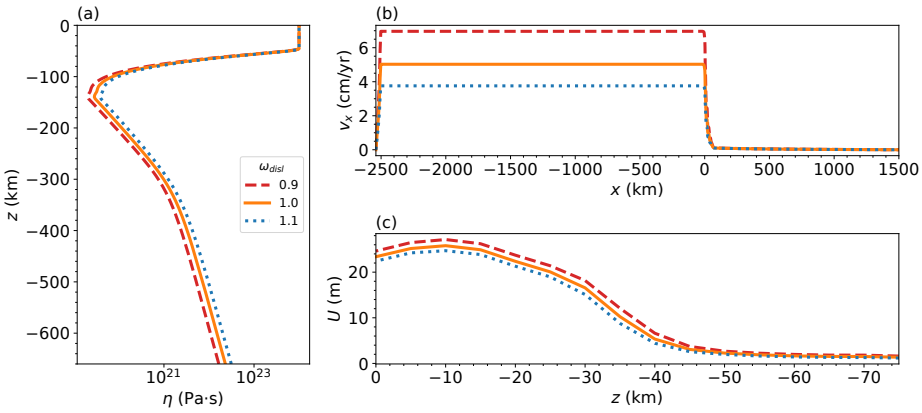

Figure 3.8: (a) Viscosity profile, (b) long-term horizontal velocitiy along the surface, and (c) coseismic slip along the megathrust shear zone when ω_{disl} is varied. Note that the viscosity is in log scale while the surface velocity is in linear scale.

coseismic displacements while having a negligible effect on long-term plate motions. For a fixed stress drop, larger coseismic displacements arise with lower rigidity of tectonic plates. The maximum coseismic slip decreases to 24 m as G_b increases to 70 GPa and increases to 29 m when G_b is reduced to 50 GPa. The amplitude of surface displacement scales in proportion to the megathrust slip. Similarly, the maximum coseismic slip is 22 m for G_{sz} = 40 GPa and 31 m for G_{sz} = 20 GPa. However, the long-term velocity field in both the lithospheric plates and mantle flow remains nearly identical for different shear modulus structures, as the long-term deformation is dominated by a viscous rheology.

Megathrust friction plays a dual role in modulating the long-term motion and coseismic response of the lithosphere and underlying mantle (Figs. 3.9 and 3.S5). During most of the seismic cycle, slip velocities along the megathrust remain low, and the interseismic friction coefficient thus dominates the inter-plate frictional resistance over a long time scale. The plate convergence rate decreases to 4.8 cm/yr for μ_s = 0.4 and increases to 5.2 cm/yr for μ_s = 0.6. Coseismic displacements are governed by the stress drop on the megathrust, which depends on the difference between the interseismic and coseismic friction coefficients. In the reference case, the difference $\mu_s - \mu_d$ is 0.3 in the seismogenic zone, resulting in an average stress drop of 9 MPa and a maximum coseismic slip of 26 m. When $\mu_s - \mu_d = 0.2$, the average stress drop decreases proportionally to 6 MPa, and the maximum coseismic slip is reduced to 16 m. Conversely, increasing the difference $\mu_s - \mu_d$ to 0.4 raises the average stress drop to 12 MPa and the maximum coseismic slip to 34 m.

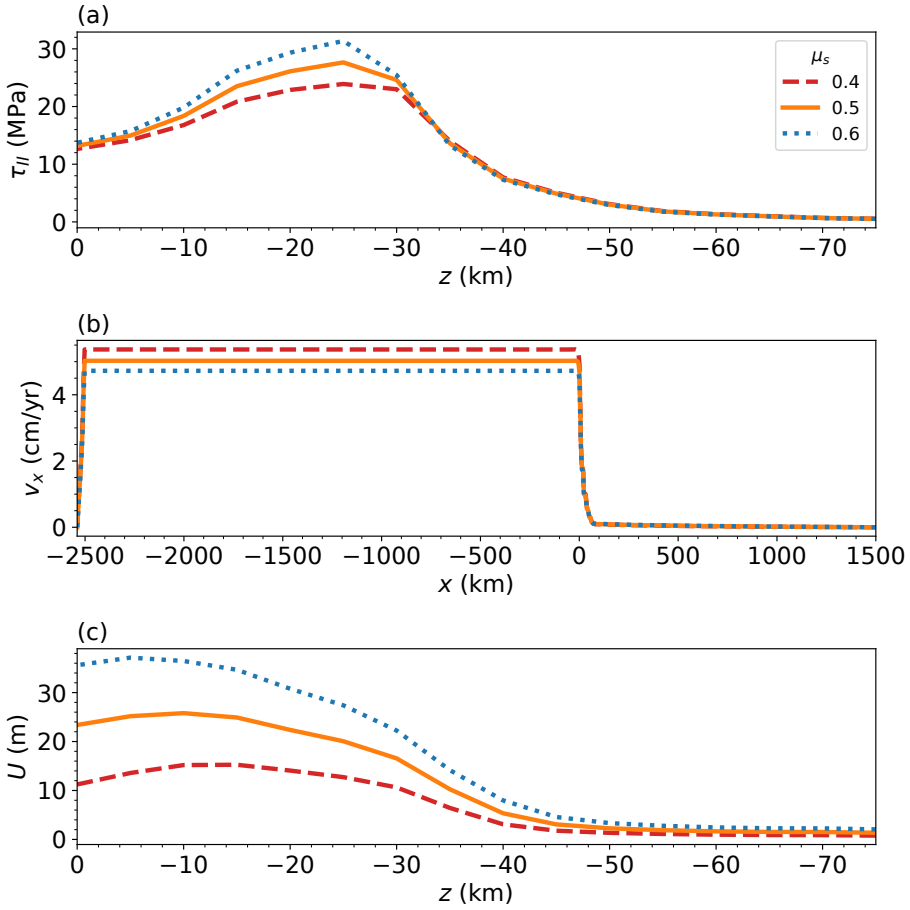

Figure 3.9: (a) Second invariant of the deviatoric stress along the megathrust shear zone, (b) long-term horizontal velocitiy along the surface, and (c) coseismic slip along the megathrust shear zone when μ_s is perturbed.

Influence of subduction structural characteristics

The selected subduction parameters, the age of the incoming plate, A_i, and the average dip angle of the seismogenic zone, Θ, exert a substantial influence on both long-term plate velocity and coseismic slip on the megathrust (Fig. 3.10). We set the parameter h to 66 km so that the rupture reaches the downdip limit of the seismogenic zone determined by brittle-ductile transition. In this scenario, the maximum along-dip rupture width is primarily controlled by the megathrust geometry and thermal structure. For a fixed megathrust geometry, increasing the incoming plate age from 20 to 110 Myr leads to a steady increase in the plate velocity from 2.8 cm/yr to a peak of 7.2 cm/yr, with the increased negative buoyancy of the older and colder plate. However, when the plate age further increases to 140 Myr, the plate velocity decreases slightly to 6.6 cm/yr, as the increase in driving forces is eventually

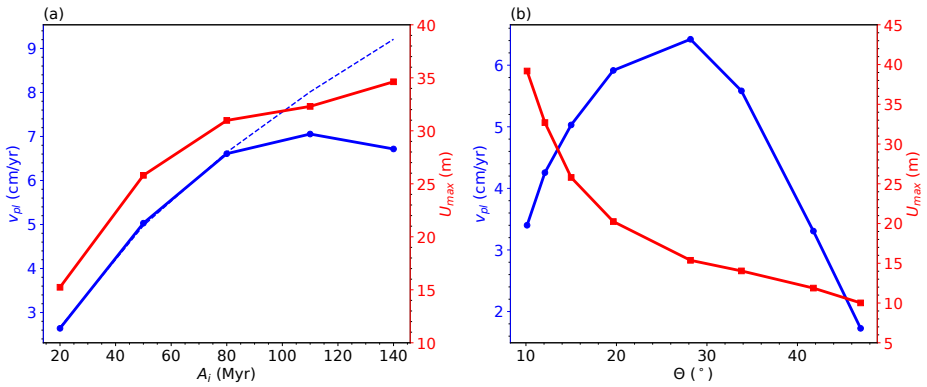

Figure 3.10: Long-term velocity of the incoming plate (blue) and maximum coseismic slip (red) for cases with different seismogenic zone dip angles (a) or different incoming plate ages.

offset by stronger resistance and dissipative processes associated with the colder and thicker plate, including larger inter-plate friction and bending resistance. In contrast, coseismic slip increases monotonically from 15 m to 35 m as the incoming plate age increases from 20 Myr to 140 Myr. Older plates produce larger slip amplitudes and longer rupture extents, consistent with the widening of the seismogenic zone in the along-dip direction.

Megathrust geometry also causes systematic variations in long-term motions and coseismic response of plates (Fig. 3.10b). For cases with small dip angles ($\Theta < 30°$), the plate velocity increases progressively with the dip angle and reaches a maximum of 6.4 cm/yr when $\Theta = 30°$. For a steeper dip angle of 47°, velocities decreases significantly, which indicates a nonlinear dependence with a peak at intermediate dip angles. Intermediate dip angles produce the highest plate velocities, as they optimize the transmission of slab pull into horizontal plate motions and simultaneously keep resistance from inter-plate friction and plate bending relatively moderate. Coseismic slip shows an opposite trend with the dip angle. Smaller dip angles produce greater peak slip and larger rupture dimensions. Increasing the dip angle from 10° to 47° leads to a monotonic decrease in coseismic slip, reflecting the narrowing of the seismogenic zone in the along-dip direction. Steeper megathrust geometries restrict the downdip rupture width and consequently limit the achievable slip and potential earthquake magnitude. In contrast, smaller dip angles usually produce a wider seismogenic zone in the along-dip direction, allowing a rupture event to extend over a larger fault area and accumulate greater coseismic slip and seismic moment.

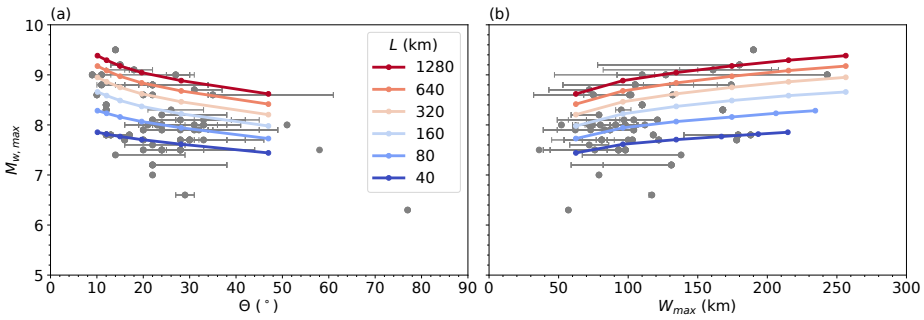

Figure 3.11: The relationship between the maximum earthquake magnitude that a subduction zone segment can host and (a) the dip angle or (b) the along-dip width of the seismogenic zone. Each line assumes a fixed along-strike rupture length (L). Gray dots with error bars are data for segments along major convergent plate boundaries, compiled by Lallemand and Heuret (2017).

For these cases with different megathrust geometries, we further impose earthquakes with along-strike rupture lengths L and compare the resulting earthquake magnitude with the maximum earthquake magnitudes observed within different segments of global subduction zones (Lallemand and Heuret, 2017) (Fig. 3.11). Analysis of these observations of large events indicates that the maximum earthquake magnitude tends to decrease with dip angles and increase with the seismogenic zone width, and the largest events only occur in segments with small dip angles and elongated seismogenic zones (Wirth et al., 2022). The trend is confirmed by computational outcomes. Particularly, for cases with large along-strike rupture lengths ($L > 500$ km), the predicted maximum earthquake magnitudes are consistent with the largest events observed in segments with similar dip angles or seismogenic zone widths. Earthquakes with $M_w > 9$ only occur for $\Theta < 20°$ and $W_{max} > 150$ km when we assume a reasonable along-strike rupture length (~ 1000 km).

3.4 Discussion

The cross-scale model applies a unified rheological formulation to control both plate motions and coseismic slip and simultaneously captures long-term and short-term behaviors. The results highlight the direct physical connection between tectonic loading driven by slab buoyancy and the episodic release of accumulated strain in great megathrust earthquakes. Megathrust seismic cycles complicate deformation patterns near plate boundaries, which is typically neglected in previous large-scale geodynamic models and potentially leads to misintepretation of geodetic observations (Graham, Loveless, and Meade, 2018; Tregoning et al., 2013). Conversely,

seismic cycle models often ignore the temporal evolution of tectonic loading rates and the impact of great earthquakes on deformation in the surrounding lithosphere. While the resulting perturbations in plate motion may be modest, reconciling the rheology governing deformation across time scales is only feasible within a unified framework. The modeling technique can also be extended to incorporate other laboratory-derived friction laws, shear heating, fluid migration, and material heterogeneity and provide additional insight into earthquake source phenomena (Dieterich, 1979; Faulkner et al., 2011; Marone, 1998; Rice, 2006).

The joint control of L and W for smaller earthquakes and primary control of L for larger ones explain the trend in observed scaling relationships (Kanamori and Anderson, 1975; Scholz, 1982). Magnitudes of smaller earthquakes are governed by rupture dimensions in both along-strike and along-dip directions and modulated by stress drop, which shows agreement with empirical self-similar scaling laws. Deviations occur for the largest megathrust earthquakes when rupture is restricted by thermal or frictional downdip limits and propagates for a long distance along strike. Subduction parameters, including convergence rate and plate age, influence the thermal structure and ultimately the depth of the brittle-ductile transition at 350–450 °C (Hyndman, Yamano, and Oleskevich, 1997; Fisher and Hirth, 2024). The downdip limit may also be shallower due to other processes altering the friction, such as fluid migration and mantle serpentinization. The along-strike rupture extent may be constrained by geometric or tectonic barriers, and the rupture dimensions are also influenced by variations in accumulated stress and inter-plate coupling, as well as dynamic rupture processes.

Variations in ω_{disl} and $\tau_{y,max}$ modify the net resistance contributed by the underlying mantle and the plate bending, respectively (Buffett, 2006; Li and Gurnis, 2023; Zhong, Gurnis, and Moresi, 1998). These parameters influence the force balance in subduction zones and exert strong control on long-term plate velocities. Geodetic observations of the current plate motion are thus diagnostic of these rheological properties of the lithosphere and mantle (Becker and O'Connell, 2001; Forte, Peltier, and Dziewonski, 1991; Hu et al., 2024; Rudi, Gurnis, and Stadler, 2022; Wu et al., 2008). While values of dislocation creep parameters in this study agree with those derived from laboratory experiments, perturbations in them likely reflect differences in composition, grain size, fluid content or melt fraction (Hirth and Kohlstedt, 2003; Karato and Wu, 1993; Ranalli, 1995). In contrast, the mantle viscosity and plate bending yield stress show minimal influence on coseismic slip,

and related variations in plate convergence rates may simply change the recurrence frequency of great earthquakes (Corbi et al., 2017). Earlier hypotheses suggesting a correlation between the maximum magnitude of megathrust earthquakes and convergence rate Ruff and Kanamori, 1980 may have been biased by the limited instrumental records. Despite the low convergence rate, the megathrust offshore Sumatra-Andaman experienced a giant event (M_w = 9.1) in 2004 Lay, Kanamori, Ammon, Nettles, et al., 2005. In a subduction system, the occurrence of great earthquakes is governed by a combination of factors, and the convergence rate can show nonlinear relationships with subduction zone characteristics that also control earthquake behavior.

The interseismic friction coefficient, μ_s, on the megathrust controls long-term plate velocity by regulating inter-plate resistance, while the difference between interseismic and coseismic friction coefficients ($\mu_s - \mu_d$) in the seismogenic zone determines the local stress drop and coseismic slip. The dual role of megathrust friction in both long-term and short-term deformations is often overlooked in previous studies. Assuming a typical friction coefficient of 0.5, achieving several cm/yr plate velocity in the model necessitates high pore fluid pressure. The long-term megathrust shear stress on the order of of 10–40 MPa is comparable to estimates from mountain height on the overriding plate (Dielforder, Hetzel, and Oncken, 2020; Lamb, 2006). The results show a stress drop of 6–12 MPa at the rupture center, and the values fall within the range of typical seismological estimates (Allmann and Shearer, 2009). In realistic scenarios, the average stress drop for an event also depends on the dimension of the ruptured area, and the frictional parameters are not uniform along plate boundaries. The heterogeneous distribution of asperities may explain the variability in earthquake rupture patterns.

Structural characteristics of the subduction system also impose important constraints on the multi-scale behavior from plate-scale geodynamics to local-scale deformation processes associated with earthquakes. Particularly, subduction parameters such as the megathrust seismogenic zone dip angle and incoming plate age regulate the balance between driving and resisting forces that govern long-term deformation. The gravitational pull exerted by colder and denser slabs has been widely recognized as a primary driver of plate motions Forsyth and Uyeda, 1975; Conrad and Lithgow-Bertelloni, 2002. The incoming plate age directly modulate the magnitude of this force by controlling slab density and thickness, while the megathrust geometry strongly influence how efficiently the vertical pull is transmitted into horizontal

plate motions Zhong, Gurnis, and Moresi, 1998; Schellart, 2004; Becker, 2006. However, these parameters simultaneously influence resisting forces such as plate bending and inter-plate friction, and the combined effects of these competing forces lead to a nonlinear dependence of plate velocities on megathrust geometry and plate age. For example, the plate velocity initially follows the approximate $\sqrt{A_i}$ scaling from the magnitude of slab pull for relatively young incoming plates, but deviates from this trend when A_i is large and the increase in resistance becomes more significant. Particularly, the bending resistance increases with the third power of the plate thickness, which itself scales approximately with $\sqrt{A_i}$, and can thus reduce plate velocities of older subducting plates. This resistance also scales with the inverse cube of the radius of curvature of the bending slab, and therefore steeper megathrust geometries produce lower plate velocities. These subduction structural characteristics also control the temperature distribution, rheological properties, and stress state within the hinge zone and the megathrust shear zone and influence the resisting forces arising in these areas Turcotte and Schubert, 2002; Alisic et al., 2012. Simultaneously, the resulting thermal structure of the megathrust governs the along-dip width of the seismogenic zone and thus the potential rupture dimensions of large earthquakes Hyndman, Yamano, and Oleskevich, 1997; Oleskevich, Hyndman, and Wang, 1999. The complex coupled effects agree with previous studies and help explain the diversity of seismic and kinematic behaviors observed among global subduction zones Heuret et al., 2012; Wirth et al., 2022.

The megathrust geometry controls the possible rupture area along the plate interface and therefore plays an important role in setting an upper bound on the magnitude of earthquakes hosted by a subduction segment. Previous studies have suggested that the giant megathrust earthquakes tend to occur in subduction segments with small dip angles and wide seismogenic zones (Lallemand and Heuret, 2017; Wirth et al., 2022), and our model results show consistency with these observations. However, the maximum earthquake size and magnitude are not determined solely by geometric and thermal constraints. Variations in frictional properties, stress drop and asperity distributions can also influence the seismic potential within a megathrust (Scholz, 2019; Kanamori and Brodsky, 2004). In addition, megathrust geometries characterized by very small or large dip angles may not persist over long distances along strike, and such geometric heterogeneity can further influence the maximum rupture dimensions attainable within a given segment (Bletery et al., 2016; Lallemand and Heuret, 2017). The final seismic moment of a specific event also depends on rupture nucleation and propagation processes. Except for the largest

events, rupture during an earthquake may not propagate across the entire permitted rupture dimensions. Frictional or geometric barriers may arrest rupture propagation, or the available energy may be insufficient for the rupture to expand to larger areas (Lay, Kanamori, Ammon, Koper, et al., 2012; Bletery et al., 2016). For many segments, earthquakes approaching the geometrically constrained magnitude may either be inhibited by propagation barriers or simply have not occurred within the limited observational record (Fig. 3.11). Consequently, while megathrust dip angle and seismogenic zone width provide an important structural limit, the observed maximum earthquake magnitudes in different subduction segments likely reflect a combination of geometric constraints, stress conditions, and frictional heterogeneity along the plate interface.

Despite insights provided by these models, several limitations should be noted when extrapolating the results to realistic subduction systems. Firstly, the computations are based on simplified geometries, while real subduction zones are inherently 3D and often involve along-strike variations in plate geometry. In realistic scenarios, plate motions are influenced by the combined effects of multiple slabs and complex plate interactions within a global plate network, which may introduce additional driving and resisting forces currently not represented in the framework. Secondly, subduction zones show rheological heterogeneity within the lithosphere and mantle, regulated by lateral variations in composition, temperature and fluid content. These heterogeneities can modify both the stress state in the bulk and the mechanical coupling along the megathrust, potentially affecting both long-term plate kinematics and coseismic rupture behavior. Future studies incorporating more realistic 3D and heterogeneous rheological structures will be important for better quantifying the influence of these factors on the coupled evolution of plate motions and megathrust earthquakes.

3.5 Conclusions

Driven by tectonic forces, the model we developed simultaneously reproduces slow background plate motion and rapid coseismic slip. In the model, a trench-normal cross-section is extended to a 2.5D domain with a Robin boundary condition that accounts for the along-strike resistance from adjacent non-ruptured segments. This approach is validated and employed to examine the relationship between the slip behavior and rupture dimensions. Coseismic slip and effective seismic moment increases with both along-strike and along-dip rupture extent. For large earthquakes, the along-dip seismogenic width is fully ruptured, and the earthquake magnitude

is dominantly influenced by the along-strike rupture length. Synthetic earthquake magnitudes derived from the model capture key features of the observed magnitude-dimension scaling relationship. This framework permits a systematic investigation into the coupled roles of different rheological and frictional parameters in modulating plate motion and coseismic slip behavior. The results show that viscosity parameters, such as the dislocation creep weakening factor and yield stress, strongly influence long-term plate velocities but have minimal impact on coseismic deformation. In contrast, shear modulus of the megathrust shear zone and the bulk upper mantle plays an important role in regulating coseismic response of the subduction zone but show negligible influence on long-term deformation. Megathrust frictional parameters exert dual controls: The interseismic friction contributes to the resistance against plate motion, while the stress drop depends on the difference between interseismic and coseismic friction governs coseismic slip. Beyond the influence of rheological properties, structural parameters of the subduction system place important constraints on both long-term and coseismic behavior. The incoming plate age and the seismogenic zone dip angle regulate the balance between driving and resisting forces in the system and show a nonlinear control on the long-term plate velocity. Simultaneously, these factors modify the thermal structure and geometry of the seismogenic zone and influence the maximum rupture dimensions and coseismic slip. The computations demonstrate the feasibility of integrating long-term geodynamics and short-term earthquake processes within a unified physical framework and reveals their interconnected dynamics. The modeling approach paves the way for future region-specific investigations with multi-scale geophysical constraints and enhances our understanding of megathrust state and seismic hazards.

Supplementary material

Text S1. Evolving boundary condition in the 2.5D model

The expected traction is the accumulation of the viscoelastic shear stress on the front wall when there is a substantial along-strike difference in the plate motion, e.g., during and after megathrust rupture events:

$$\tau^e = 2\eta_{eff}\left(\dot{\epsilon} + \frac{\check{\tau}^e}{2G\Delta t}\right), \tag{3.S1}$$

where τ^e is the expected shear traction, and $\check{\tau}^e$ is the previous shear traction. Here τ^e_{xy} depends on $\dot{\epsilon}_{xy}$, τ^e_{zy} depends on $\dot{\epsilon}_{zy}$. We ignore the displacement in the y direction, so $\tau^e_{yy} = 0$. We assume the shear strain rate accounts for the long-wavelength velocity difference between the rupture center and the distal segments that are still moving

slowly, and define $\dot{\epsilon}_{xy} = \frac{v_x^{far} - v_x}{2\lambda}$ and $\dot{\epsilon}_{zy} = \frac{v_z^{far} - v_z}{2\lambda}$. Substitution into Equation 3.S1 gives:

$$\tau^e = \eta_{eff}\left(-\frac{v - v^{far}}{\lambda} + \frac{\check{\tau}^e}{G\Delta t}\right), \tag{3.S2}$$

where τ^e_{xy} depends on $v_x - v_x^{far}$ and τ^e_{zy} depends on $v_z - v_z^{far}$. Before the rupture, the entire plate is moving at nearly the same speed so there is no significant shear tractions along strike. The shear traction history term $\frac{\check{\tau}_e}{G\Delta t}$ is negligible and only builds up when ruptures occur. We acknowledge that this term can be important in the postseismic phase. For the lithospheric plate, the viscosity is large and $\eta_{eff} \approx G\Delta t$. Hence the expected traction should be proportional to the incremental velocity and inversely proportional to an along-strike length scale. Equation 3.S2 can be reduced to Equation 3.12, which means that the elastic shear stress is dominant.

If we move the velocity-related term, $\eta_{eff}\frac{v}{L}$ in Equation 3.S2 to the left hand size, this becomes a Robin boundary condition that specifies a linear combination of velocity and stress on the boundary. Since Robin boundary conditions are not implemented in Underworld2, we developed an iterative framework as an alternative using an evolving Neumann boundary condition. For one step, the traction is imposed continuously on the front wall based on the solved velocity from the previous iteration:

$$\tau^a_{n+1} = \phi\tau^e_n + (1 - \phi)\tau^a_n, \tag{3.S3}$$

where τ^a_i is the applied traction in the i-th iteration, τ^e_i is the traction expected from the velocity field solved in the i-th iteration, and ϕ is a weighting coefficient. The coefficient ϕ smooths the spatially heterogeneous change of traction between iterations and stabilizes the update of this boundary condition, chosen from $\phi = \min(\frac{L}{L_0}, 0.5)$, where $L_0 = 10^4$ km. The iteration terminates when the misfit between the applied traction and the expected traction calculated from the resulting velocity field is below 1‰.

Text S2. Approximation of the actual rupture length

In elastic crack models where a crack in an elastic body is subjected to uniform stress changes, the relative displacements for all the crack modes follow elliptical distributions Scholz, 2019. We use these analytical solutions to approximate the slip distribution in the y direction along the plate boundary. The slip U as a function

of y is given by:

$$U = \frac{2U_0}{L}\left(\frac{L^2}{4} - y^2\right)^{\frac{1}{2}}. \tag{3.S4}$$

U_0 is the maximum slip occurring at the center of the rupture where $y = 0$, and L is the rupture length, from the center to the tip where $U = 0$.

The gradient of slip U with respect to y is:

$$\frac{\mathrm{d}U}{\mathrm{d}y} = -\frac{4U_0 y}{L(L^2 - 4y^2)^{\frac{1}{2}}}. \tag{3.S5}$$

Under the approximation that $y << L$, which is reasonable near the rupture center ($y \approx 0$), Equation 3.S5 simplifies to:

$$\frac{dU}{dy} \approx -\frac{4U_0 y}{L^2}. \tag{3.S6}$$

In the model, a Robin boundary condition is imposed at $y = D$, where D is the domain width and $D << L$. It models the slip gradient as the difference between the slip at $y = D$ and the far-field slip (negligible compared with U_0 and assumed to be zero), divided by a length scale parameter λ:

$$\left.\frac{dU}{dy}\right|_{y=D} = -\frac{4U_0 D}{L^2} \approx -\frac{U_0}{\lambda} \tag{3.S7}$$

This leads to the scaling relation between L and λ:

$$L = 2\sqrt{\lambda D}. \tag{3.S8}$$

Text S3. Spontaneous earthquake

In the imposed earthquake (IE) model shown in the main text, earthquakes are generated by directly modifying the megathrust friction from static values to dynamic ones. Alternatively, earthquakes can be triggered by spontaneous slip instability due to megathrust friction dependent on slip rates and other state variables (e.g., Dinther et al. (2013), Sobolev and Muldashev (2017), Yang et al. (2023), and Fang, Gurnis, and Lapusta (2024)). The spontaneous earthquake (SE) model is computationally more expensive and is used to validate the recurrence period inferred from the IE model approach. We apply a rate-dependent friction law from Dinther et al. (2013) in the megathrust shear zone:

$$\mu = \mu_d + \frac{\mu_s - \mu_d}{1 + \frac{V}{V_{ref}}}, \tag{3.S9}$$

where μ_s and μ_d are static and dynamic friction coefficients, V_{ref} is a reference slip velocity set to 100 cm/year, and V is the local slip velocity, defined as twice the shear zone width multiplying the second invariant of the strain rate (Dinther et al., 2013; Yang et al., 2023). The reference slip velocity V_{ref} is much larger than the plate convergence rate, which permits friction coefficients in the megathrust shear zone to approach μ_s in the inter-seismic period and μ_d during earthquakes. The seismogenic zone at a depth of 10–40 km features an unstable regime with a strong rate-weakening friction ($\mu_d < \mu_s$). The updip and downdip portions are rate-strengthening ($\mu_d > \mu_s$) and host aseismic slip.

In the SE model, we obtain the long-term plate motion and initial stress by solving the Stokes system with a large time step size of 4×10^4 years until the steady state as well, and subsequently compute the model with a reduced time step size of 5 years. The rate-dependent friction law is used throughout SE model computations. The time step size is larger than that for the IE model to avoid numerical issues for the highly nonlinear system. The first few seismic cycles correspond to the "spin-up" period and should be ignored.

When the stress drop is comparable between the IE and SE models, the resulting coseismic deformation is largely consistent. The computed coseismic displacement field is further validated by extracting megathrust slip from the IE model and applying it to the analytical Okada formulation (Okada, 1985) (Fig. 3.S1). The surface displacements show good agreement between the computational model and the analytical solution, regardless of whether a Poisson's ratio of 0.25 or 0.5 is assumed. The influence of compressibility is likely minor, as shear deformation dominates the response. The assumption of full strain release is also supported by results of the SE model, in which the recurrence time is directly computed and the permanent deformation only constitutes a small fraction of total displacement.

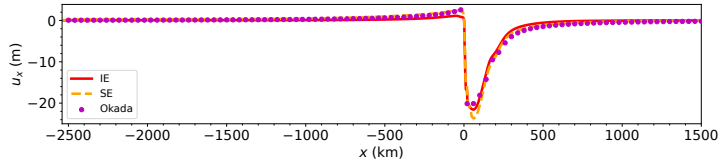

Figure 3.S1: Coseismic horizontal displacements along the surface, u_x, predicted by the IE model (red solid), SE model (orange dashed), and Okada solution (purple dotted) Okada, 1985.

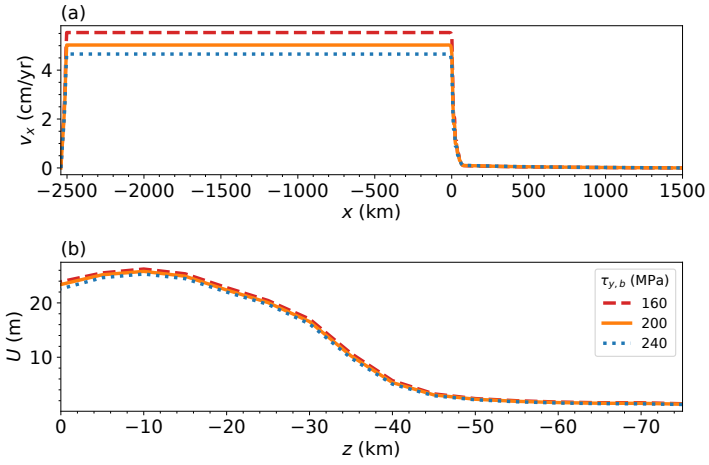

Figure 3.S2: (a) Long-term horizontal velocitiy along the surface and (b) coseismic slip along the megathrust shear zone when $\tau_{y,b}$ is varied.

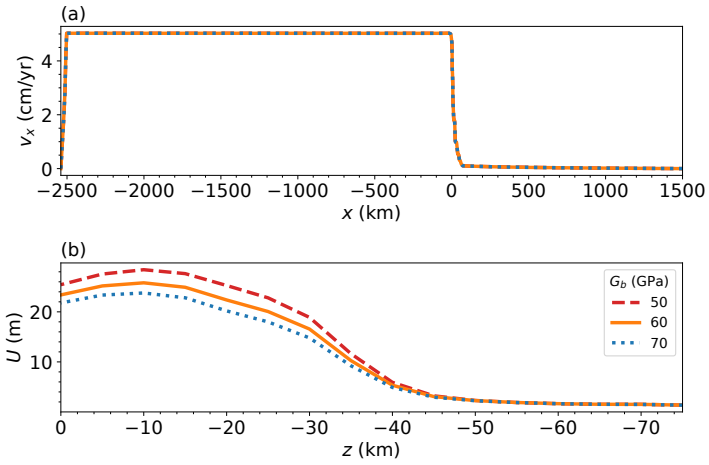

Figure 3.S3: (a) Long-term horizontal velocitiy along the surface and (b) coseismic slip along the megathrust shear zone when G_b is varied.

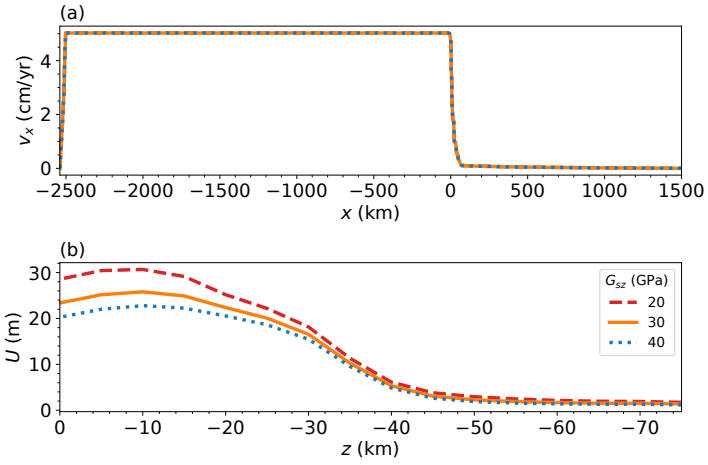

Figure 3.S4: (a) Long-term horizontal velocitiy along the surface and (b) coseismic slip along the megathrust shear zone when G_{sz} is varied.

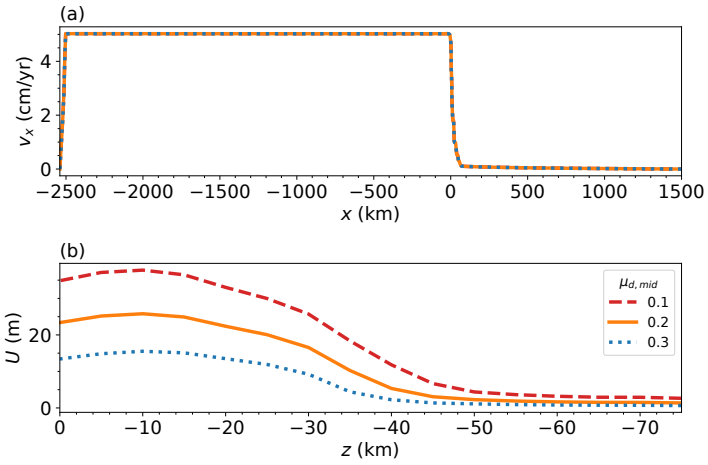

Figure 3.S5: (a) Long-term horizontal velocitiy along the surface and (b) coseismic slip along the megathrust shear zone when $\mu_{d,mid}$ is varied.

References

Alisic, Laura et al. (2012). "Multi-scale dynamics and rheology of mantle flow with plates". In: *Journal of Geophysical Research: Solid Earth* 117.B10.

Allmann, Bettina P and Peter M Shearer (2009). "Global variations of stress drop for moderate to large earthquakes". In: *Journal of Geophysical Research: Solid Earth* 114.B1.

Barbot, Sylvain, Nadia Lapusta, and Jean-Philippe Avouac (2012). "Under the hood of the earthquake machine: Toward predictive modeling of the seismic cycle". In: *Science* 336.6082, pp. 707–710.

Becker, Thorsten W (2006). "On the effect of temperature and strain-rate dependent viscosity on global mantle flow, net rotation, and plate-driving forces". In: *Geophysical Journal International* 167.2, pp. 943–957.

Becker, Thorsten W and Richard J O'Connell (2001). "Predicting plate velocities with mantle circulation models". In: *Geochemistry, Geophysics, Geosystems* 2.12.

Behr, Whitney M et al. (2022). "The effects of plate interface rheology on subduction kinematics and dynamics". In: *Geophysical Journal International* 230.2, pp. 796–812.

Bilek, Susan L and Thorne Lay (2018). "Subduction zone megathrust earthquakes". In: *Geosphere* 14.4, pp. 1468–1500.

Bletery, Quentin et al. (2016). "Mega-earthquakes rupture flat megathrusts". In: *Science* 354.6315, pp. 1027–1031.

Brocher, Thomas M (2005). "Empirical relations between elastic wavespeeds and density in the Earth's crust". In: *Bulletin of the seismological Society of America* 95.6, pp. 2081–2092.

Buffett, Bruce A (2006). "Plate force due to bending at subduction zones". In: *Journal of Geophysical Research: Solid Earth* 111.B9.

Conrad, Clinton P and Bradford H Hager (1999). "Effects of plate bending and fault strength at subduction zones on plate dynamics". In: *Journal of Geophysical Research: Solid Earth* 104.B8, pp. 17551–17571.

Conrad, Clinton P and Carolina Lithgow-Bertelloni (2002). "How mantle slabs drive plate tectonics". In: *Science* 298.5591, pp. 207–209.

Corbi, Fabio et al. (2017). "Controls of seismogenic zone width and subduction velocity on interplate seismicity: Insights from analog and numerical models". In: *Geophysical Research Letters* 44.12, pp. 6082–6091.

Dielforder, Armin, Ralf Hetzel, and Onno Oncken (2020). "Megathrust shear force controls mountain height at convergent plate margins". In: *Nature* 582.7811, pp. 225–229.

Dieterich, James H (1979). "Modeling of rock friction: 1. Experimental results and constitutive equations". In: *Journal of Geophysical Research: Solid Earth* 84.B5, pp. 2161–2168.

Dinther, Y van et al. (2013). "The seismic cycle at subduction thrusts: Insights from seismo-thermo-mechanical models". In: *Journal of Geophysical Research: Solid Earth* 118.12, pp. 6183–6202.

Fang, Jiaqi, Michael Gurnis, and Nadia Lapusta (2024). "Dynamic emergence of plate motions and great megathrust earthquakes across length and time scales". In: *Geophysical Research Letters* 51.22, e2024GL110821. DOI: 10.1029/2024GL110821.

Fang, Jiaqi, Michael Gurnis, and Rishav Mallick (2025). "Constraints on nonlinear mantle rheology from multi-scale geodetic observations of plate motion and post-seismic enhanced landward motion". In: *Earth and Planetary Science Letters* 669, p. 119566. DOI: 10.1016/j.epsl.2025.119566.

Farrington, RJ, L-N Moresi, and Fabio Antonio Capitanio (2014). "The role of viscoelasticity in subducting plates". In: *Geochemistry, Geophysics, Geosystems* 15.11, pp. 4291–4304.

Faulkner, DR et al. (2011). "Stuck in the mud? Earthquake nucleation and propagation through accretionary forearcs". In: *Geophysical Research Letters* 38.18.

Fisher, Donald M and Greg Hirth (2024). "A pressure solution flow law for the seismogenic zone: Application to Cascadia". In: *Science Advances* 10.4, eadi7279.

Forsyth, Donald and Seiya Uyeda (1975). "On the relative importance of the driving forces of plate motion". In: *Geophysical Journal International* 43.1, pp. 163–200.

Forte, AM, WR Peltier, and AM Dziewonski (1991). "Inferences of mantle viscosity from tectonic plate velocities". In: *Geophysical Research Letters* 18.9, pp. 1747–1750.

Garel, Fanny et al. (2014). "Interaction of subducted slabs with the mantle transition-zone: A regime diagram from 2-D thermo-mechanical models with a mobile trench and an overriding plate". In: *Geochemistry, Geophysics, Geosystems* 15.5, pp. 1739–1765.

Graham, Shannon E, John P Loveless, and Brendan J Meade (2018). "Global plate motions and earthquake cycle effects". In: *Geochemistry, Geophysics, Geosystems* 19.7, pp. 2032–2048.

Hager, Bradford H and Richard J O'Connell (1981). "A simple global model of plate dynamics and mantle convection". In: *Journal of Geophysical Research: Solid Earth* 86.B6, pp. 4843–4867.

Heuret, Arnauld et al. (2012). "Relation between subduction megathrust earthquakes, trench sediment thickness and upper plate strain". In: *Geophysical Research Letters* 39.5.

Hirth, Greg and D Kohlstedt (2003). “Rheology of the upper mantle and the mantle wedge: A view from the experimentalists”. In: *Geophysical monograph-american geophysical union* 138, pp. 83–106.

Hu, Jiashun et al. (2024). “Constraining Earth’s nonlinear mantle viscosity using plate-boundary resolving global inversions”. In: *Proceedings of the National Academy of Sciences* 121.28, e2318706121.

Hyndman, Roy D, Makoto Yamano, and Dan A Oleskevich (1997). “The seismogenic zone of subduction thrust faults”. In: *Island Arc* 6.3, pp. 244–260.

Jiang, Junle et al. (2022). “Community-driven code comparisons for three-dimensional dynamic modeling of sequences of earthquakes and aseismic slip”. In: *Journal of Geophysical Research: Solid Earth* 127.3, e2021JB023519.

Kanamori, Hiroo (2014). “The diversity of large earthquakes and its implications for hazard mitigation”. In: *Annual Review of Earth and Planetary Sciences* 42.1, pp. 7–26.

Kanamori, Hiroo and Don L Anderson (1975). “Theoretical basis of some empirical relations in seismology”. In: *Bulletin of the seismological society of America* 65.5, pp. 1073–1095.

Kanamori, Hiroo and Emily E Brodsky (2004). “The physics of earthquakes”. In: *Reports on progress in physics* 67.8, pp. 1429–1496.

Karato, Shun-ichiro and Patrick Wu (1993). “Rheology of the upper mantle: A synthesis”. In: *Science* 260.5109, pp. 771–778.

Lallemand, Serge and Arnauld Heuret (2017). “Subduction zones parameters”. In: *Reference module in Earth systems and environmental sciences*.

Lamb, Simon (2006). “Shear stresses on megathrusts: Implications for mountain building behind subduction zones”. In: *Journal of Geophysical Research: Solid Earth* 111.B7.

Lapusta, Nadia and Yi Liu (2009). “Three-dimensional boundary integral modeling of spontaneous earthquake sequences and aseismic slip”. In: *Journal of Geophysical Research: Solid Earth* 114.B9.

Lay, Thorne, Hiroo Kanamori, Charles J Ammon, Keith D Koper, et al. (2012). “Depth-varying rupture properties of subduction zone megathrust faults”. In: *Journal of Geophysical Research: Solid Earth* 117.B4.

Lay, Thorne, Hiroo Kanamori, Charles J Ammon, Meredith Nettles, et al. (2005). “The great Sumatra-Andaman earthquake of 26 december 2004”. In: *science* 308.5725, pp. 1127–1133.

Li, Yida and Michael Gurnis (2023). “A simple force balance model of subduction initiation”. In: *Geophysical Journal International* 232.1, pp. 128–146.

Mansour, John A et al. (Aug. 2020). *Underworld2: Python Geodynamics Modelling for Desktop, HPC and Cloud*. Software. Version v2.10.0b. DOI: 10.5281/zenodo.3975252. URL: https://doi.org/10.5281/zenodo.3975252.

Marone, Chris (1998). "Laboratory-derived friction laws and their application to seismic faulting". In: *Annual Review of Earth and Planetary Sciences* 26.1, pp. 643–696.

Moernaut, Jasper et al. (2018). "Larger earthquakes recur more periodically: New insights in the megathrust earthquake cycle from lacustrine turbidite records in south-central Chile". In: *Earth and Planetary Science Letters* 481, pp. 9–19.

Okada, Yoshimitsu (1985). "Surface deformation due to shear and tensile faults in a half-space". In: *Bull. Seismol. Soc. Am* 75.4, pp. 1135–1154.

Oleskevich, DA, RD Hyndman, and K Wang (1999). "The updip and downdip limits to great subduction earthquakes: Thermal and structural models of Cascadia, south Alaska, SW Japan, and Chile". In: *Journal of Geophysical Research: Solid Earth* 104.B7, pp. 14965–14991.

Philibosian, Belle and Aron J Meltzner (2020). "Segmentation and supercycles: A catalog of earthquake rupture patterns from the Sumatran Sunda Megathrust and other well-studied faults worldwide". In: *Quaternary Science Reviews* 241, p. 106390.

Ranalli, Giorgio (1995). *Rheology of the Earth*. Springer Science & Business Media.

Reid, HF (1910). "On mass-movements in tectonic earthquakes". In: *The California earthquake of April 18, 1906: Report of the state earthquake investigation commission*, p. 192.

Rice, James R (2006). "Heating and weakening of faults during earthquake slip". In: *Journal of Geophysical Research: Solid Earth* 111.B5.

Rudi, Johann, Michael Gurnis, and Georg Stadler (2022). "Simultaneous inference of plate boundary stresses and mantle rheology using adjoints: large-scale 2-D models". In: *Geophysical Journal International* 231.1, pp. 597–614.

Ruff, Larry J and Hiroo Kanamori (1980). "Seismicity and the subduction process". In: *Physics of the Earth and Planetary interiors* 23.3, pp. 240–252.

Schellart, WP (2004). "Kinematics of subduction and subduction-induced flow in the upper mantle". In: *Journal of Geophysical Research: Solid Earth* 109.B7.

Scholz, Christopher H (1982). "Scaling laws for large earthquakes: consequences for physical models". In: *Bulletin of the Seismological Society of America* 72.1, pp. 1–14.

– (2019). *The Mechanics of Earthquakes and Faulting*. Cambridge University Press.

Scholz, Christopher H and Jaime Campos (2012). "The seismic coupling of subduction zones revisited". In: *Journal of Geophysical Research: Solid Earth* 117.B5.

Sobolev, Stephan V and Iskander A Muldashev (2017). "Modeling seismic cycles of great megathrust earthquakes across the scales with focus at postseismic phase". In: *Geochemistry, Geophysics, Geosystems* 18.12, pp. 4387–4408.

Stadler, Georg et al. (2010). "The dynamics of plate tectonics and mantle flow: From local to global scales". In: *Science* 329.5995, pp. 1033–1038.

Sun, Tianhaozhe, Kelin Wang, and Jiangheng He (2024). "Geodetic signature of a weak lithosphere-asthenosphere boundary in postseismic deformation of large subduction earthquakes". In: *Earth and Planetary Science Letters* 630, p. 118619.

Thingbaijam, Kiran Kumar S, P Martin Mai, and Katsuichiro Goda (2017). "New empirical earthquake source-scaling laws". In: *Bulletin of the Seismological Society of America* 107.5, pp. 2225–2246.

Tregoning, Paul et al. (2013). "A decade of horizontal deformation from great earthquakes". In: *Journal of Geophysical Research: Solid Earth* 118.5, pp. 2371–2381.

Turcotte, Donald L and Gerald Schubert (2002). *Geodynamics*. Cambridge university press.

Wang, Kelin and Susan L Bilek (2014). "Invited review paper: Fault creep caused by subduction of rough seafloor relief". In: *Tectonophysics* 610, pp. 1–24.

Wang, Kelin, Yan Hu, and Jiangheng He (2012). "Deformation cycles of subduction earthquakes in a viscoelastic Earth". In: *Nature* 484.7394, pp. 327–332.

Wang, Min and Zheng-Kang Shen (2020). "Present-day crustal deformation of continental China derived from GPS and its tectonic implications". In: *Journal of Geophysical Research: Solid Earth* 125.2, e2019JB018774.

Wirth, Erin A et al. (2022). "The occurrence and hazards of great subduction zone earthquakes". In: *Nature Reviews Earth & Environment* 3.2, pp. 125–140.

Wu, Benjun et al. (2008). "Reconciling strong slab pull and weak plate bending: The plate motion constraint on the strength of mantle slabs". In: *Earth and Planetary Science Letters* 272.1-2, pp. 412–421.

Yang, Haibin et al. (2023). "Numerical Modeling of Earthquake Cycles Based On Navier-Stokes Equations With Viscoelastic-Plasticity Rheology". In: *Geochemistry, Geophysics, Geosystems* 24.9, e2023GC010872.

Zhong, Shijie and Michael Gurnis (1995). "Mantle convection with plates and mobile, faulted plate margins". In: *Science* 267.5199, pp. 838–843.

Zhong, Shijie, Michael Gurnis, and Louis Moresi (1998). "Role of faults, nonlinear rheology, and viscosity structure in generating plates from instantaneous mantle flow models". In: *Journal of Geophysical Research: Solid Earth* 103.B7, pp. 15255–15268.

Chapter 4

CONSTRAINTS ON NONLINEAR MANTLE RHEOLOGY FROM MULTI-SCALE GEODETIC OBSERVATIONS OF PLATE MOTION AND POST-SEISMIC ENHANCED LANDWARD MOTION

Fang, Jiaqi, Michael Gurnis, and Rishav Mallick (2025). "Constraints on nonlinear mantle rheology from multi-scale geodetic observations of plate motion and post-seismic enhanced landward motion". In: *Earth and Planetary Science Letters* 669, p. 119566. DOI: 10.1016/j.epsl.2025.119566.

Abstract

Plate motions and post-seismic deformation are surface expressions of Earth's nonlinear dynamics shaped by a visco-elasto-plastic rheology. A particularly exciting avenue of investigation lies in the development of numerical models that can self-consistently resolve these processes across spatial and temporal scales. We formulate a three-dimensional model of the Chilean subduction zone that incorporates buoyancy forces, nonlinear rheology, shear modulus variability and friction on the megathrust. When dislocation creep parameters are varied, computations produce the $\approx$ 7 cm/year motion of the Nazca Plate but different vertical viscosity profiles in the upper mantle. The model predicts enhanced landward motion (ELM) in the non-ruptured segment on the overriding plate adjacent to the 2010 Maule earthquake (M_w = 8.8), with amplitudes inversely related to the asthenosphere viscosity. Our preferred model shows a pre-seismic viscosity of 5–9 $\times 10^{18}$ Pa·s in the asthenosphere and $\sim 10^{21}$ Pa·s close to the 660 km interface, and is able to reproduce the $\sim$ 5 mm/year ELM observed geodetically. The range of permissible nonlinear rheological parameters is wide when constrained by the long-term motion of the Nazca Plate alone, but becomes well posed when post-seismic observations are simultaneously considered. The model reconciles experimentally-constrained dislocation creep parameters, long-term plate velocities and far-field post-seismic deformation and advances our understanding of nonlinear mantle rheology.

4.1 Introduction

Tectonic plates on Earth's surface move at a steady velocity of several centimeters per year in the inter-seismic period, which is intermittently interrupted by rapid slip in great earthquakes and post-seismic deformation following these large events. These multi-scale processes reflect a visco-elasto-plastic rheology of the solid Earth and carry valuable information about the depth-varying structure (Wang, Hu, and He, 2012). On long time scales, plate motions result from the force balance between the driving slab pull and resistance from the underlying mantle, the bending in subduction zones and the frictional plate interface (Conrad and Hager, 1999; Alisic et al., 2012; Behr et al., 2022; Li and Gurnis, 2023). Viscous flow in the upper mantle provides an important resisting force, and its nonlinear strain-rate-weakening viscosity caused by dislocation creep plays a crucial role in enabling plate mobility (Solomatov and Moresi, 1997; Zhong, Gurnis, and Moresi, 1998).

The nonlinear mantle rheology depends on temperature, pressure and strain rate, and the range of constitutive parameters is primarily constrained by laboratory experiments (Karato and Wu, 1993; Ranalli, 1995; Hirth and Kohlstedt, 2003). While concerns have been raised regarding the applicability of these experimentally-derived values to geological processes under much lower strain rates, parameters of the flow laws can alternatively be inferred from current plate motions with robust inversion techniques (Rudi, Gurnis, and Stadler, 2022; Hu, Rudi, et al., 2024). The inversion outcomes have deepened our understanding of Earth's rheological properties, although they are subject to trade-offs between rheological parameters and viscosity structures at different depths (Forte, Peltier, and Dziewonski, 1991; King, 1995; Hu, Rudi, et al., 2024). Other geophysical observations modulated by viscoelastic processes can also provide useful constraints on the mantle rheology, such as the gravitational field (Hager, 1984; Mao and Zhong, 2021), post-glacial rebound (Mitrovica and Forte, 2004; Han et al., 2024) and post-seismic deformation (Hu, Bürgmann, et al., 2016; Freed et al., 2017; Marsman et al., 2025). These studies recover effective viscosities over different spatial and temporal scales in Earth's interior (Cathles, 1975; Wang, Hu, and He, 2012; Lau et al., 2021), and reconciling them with a single, scale-independent set of parameters remains an open question.

Great earthquakes at subduction zone megathrust faults cause the largest perturbation to long-term plate motions. The rapid rupture is typically followed by post-seismic deformation characterized by strong seaward motions onshore of the

ruptured segment, which are controlled by viscoelastic relaxation in the mantle but complicated by afterslip on the megathrust (Perfettini and Avouac, 2004; Sun, Wang, Iinuma, et al., 2014; Bedford et al., 2016; Barbot, 2018; Köhne, Mallick, and Simons, 2025). In the neighboring non-ruptured segment, inland geodetic measurements have recorded enhanced landward motion (ELM) following several megathrust earthquakes (Heki and Mitsui, 2013; Melnick et al., 2017; Yuzariyadi and Heki, 2021): Landward velocities on the compressed overriding plate increase beyond the pre-existing inter-seismic landward motion due to fault locking. These velocity changes can persist over years and their amplitude and extent are correlated with the earthquake's moment and along-strike size. While enhanced plate coupling (Loveless, 2017; Melnick et al., 2017), plate bending (D'Acquisto, Herman, et al., 2023) or plate rotation (Corbi et al., 2022) failed to alone explain the full ELM patterns with a general model setup, others attribute the ELM to the acceleration of the incoming plate after a great earthquake, which imposes a significant horizontal force on the overriding plate (Heki and Mitsui, 2013; Sun, Wang, and He, 2024). In models that reproduce the overall characteristics of ELM, Sun, Wang, and He, 2024 proposed the existence of a weak ($\sim 10^{17}$ Pa·s) and narrow ($\sim$ 10 km) lithosphere-asthenosphere boundary (LAB) that leads to faster deformation within the incoming plate by decoupling it from the underlying mantle. This model provides crucial insight that the ELM in non-ruptured segments of the plate boundary is primarily sensitive to the viscosity structure at shallow depth, although it ignores the nonlinear mantle dynamics controlled by the thermal structure. Critically, the influence of a persistent, thin, and weak LAB on the cm/year long-term plate motion over a broader length scale is not considered.

We developed a three-dimensional cross-scale subduction model that treats the short-term ELM adjacent to the ruptured plate boundary self-consistently with long-term whole-plate kinematics and constrains the upper mantle viscosity structure with both geophysical observations. The model is tailored to subduction in central Chile and predicts the $\approx$ 7 cm/year motion of the subducting Nazca Plate. We examine computations with different viscosity structures that maintain the long-term plate velocity. ELM signals emerge in areas 500–1000 km away from the epicenter in the along-strike direction after an M_w = 8.8 earthquake is imposed, and the amplitude of ELM is inversely correlated with the asthenosphere viscosity. When the pre-seismic viscosity is 5–9 $\times 10^{18}$ Pa·s in the asthenosphere and increases to $\sim 10^{21}$ Pa·s in the deeper part of the upper mantle, the model predicts $\sim$ 5 mm/year ELM that matches GNSS observations. Incorporating both post-seismic deformation observations and

current plate motions as constraints can narrow the range of permissible nonlinear rheological parameters and significantly improve estimates of mantle viscosities.

4.2 Method

Model setup

The Nazca Plate is subducting beneath the South America Plate at a velocity of 6–8 cm/year (DeMets, Gordon, and Argus, 2010; Altamimi et al., 2017; Jarrin et al., 2023), and the plate boundary offshore Chile hosts destructive megathrust earthquakes. Major events include the 1960 Valdivia earthquake (M_w = 9.5) and the 2010 Maule earthquake (M_w = 8.8) (Ruiz and Madariaga, 2018). The improved availability of GNSS measurements allows us to detect clear ELM signals after the 2010 event (Fig. 4.1), which persisted until another major earthquake in the region of interest (the 2015 Illapel earthquake, M_w = 8.3) (Ruiz and Madariaga, 2018). The relatively small size of the Nazca Plate and the simple, generally straight plate boundary near the epicenter make this region ideal for integrating whole-plate kinematics with ELM.

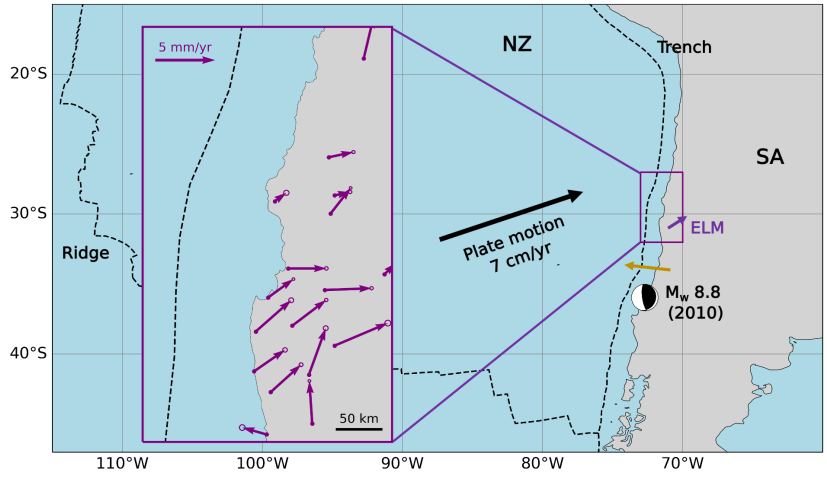

Figure 4.1: A map of the Chilean subduction zone with two types of geodetic observations: the long-time motion of the Nazca Plate and the enhanced landward motion (ELM) in the adjacent segment after the 2010 Maule earthquake. Purple arrows in the zoom-in plot show differences between the post-seismic and pre-seismic GNSS velocities, measured by Melnick et al., 2017. NZ and SA refer to the Nazca Plate (incoming) and South America Plate (overriding), respectively.

We set up a subduction model in a three-dimensional Cartesian domain with 7580 km in the trench-normal direction, x, 2000 km in the along-strike direction, y, and 800 km in the vertical direction, z (Fig. 4.2a). The model contains the entire

incoming plate from ridge to trench, which is separated from the overriding plate by the megathrust approximated by a 12-km-thick shear zone. The slab interface is interpolated from the Slab2 model (Hayes et al., 2018) along a trench-perpendicular profile at 36°S, and a temperature structure is established based on thermal diffusion (see Text S1 and Fig. 4.S1). We investigate the first-order rheological controls on the multi-scale plate deformation and ignore the along-strike variability of slab geometry. The mesh consists of 1024 (x) × 256 (y) × 128 (z) linear elements, with the element size refined to 2.2 km near the megathrust. This grid resolution is sufficient to ensure a well-resolved shear zone and numerically reliable results, as confirmed by convergence tests. The domain boundaries are free-slip, and the negative buoyancy of the slab drives deformation. Since the deformation in the model is much smaller than the element size, we assume infinitesimal strain and neglect changes in mesh geometry over time.

The computations are performed using the open-source finite-element software Underworld2 (Mansour et al., 2020), which solves the continuity and momentum equations for incompressible materials. Underworld2 has been adapted to short-timescale processes with Maxwell viscoelastic and visco-elasto-plastic rheology (Moresi, Dufour, and Mühlhaus, 2002; Farrington, Moresi, and Capitanio, 2014; Yang et al., 2023; Fang, Gurnis, and Lapusta, 2024). Similar computational methods have also been implemented with other Stokes solvers and extensively used for studying earthquake-related problems (e.g., Dinther, Gerya, Dalguer, Mai, et al., 2013; Sobolev and Muldashev, 2017; Oryan and Buck, 2020).

Rheology

We model deformation as a composite of viscous creep and elastic displacement. The effective viscosity is dominated by dislocation creep in the upper mantle above 660 km and diffusion creep in the lower mantle (Karato and Wu, 1993; Ranalli, 1995). The dislocation and diffusion creep viscosities (η_{disl} and η_{diff}) are parametrized in a unified functional representation as:

$$\eta_{disl/diff} = \omega A^{-\frac{1}{n}} \dot{\epsilon}_{II}^{\frac{1-n}{n}} \exp\left(\frac{E + pV}{nRT}\right), \tag{4.1}$$

where $\eta_{disl/diff}$ denotes η_{disl} or η_{diff}, ω is a weakness factor that we will systematically vary in computations, A is a prefactor, n is the stress exponent (3.5 for dislocation creep and 1 for diffusion creep), R is the gas constant, E is the activation energy, V is the activation volume, $\dot{\epsilon}_{II}$ is the second invariant of the strain rate tensor, p is the pressure, and T is the temperature (see more details in Text S2).

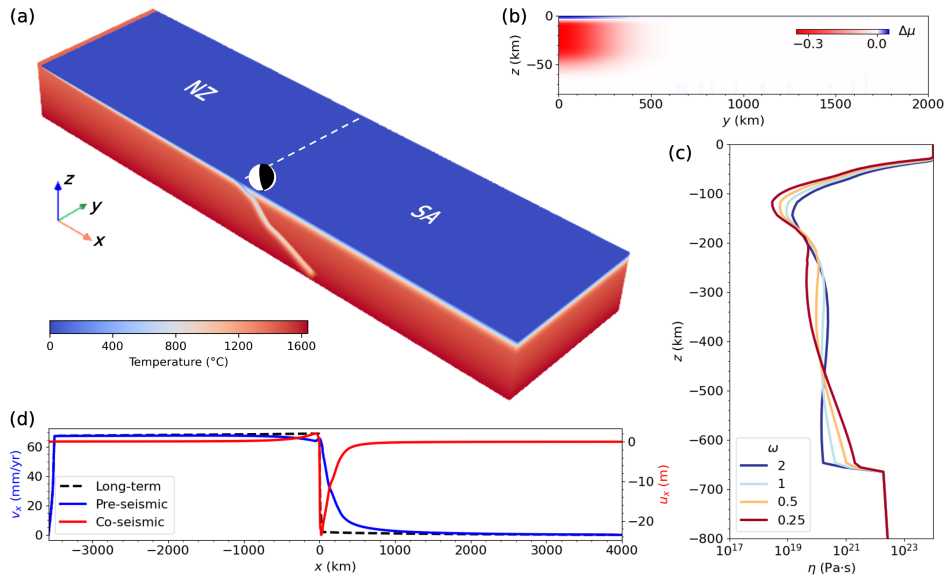

Figure 4.2: (a) Model setup with the temperature field. The model domain is 7580 km (x) × 2000 km (y) × 800 km (z). The white dashed line shows the location of the trench (x = 0 km and z = 0 km), and the focal mechanism shows the location of the earthquake epicenter (in the plane y = 0 km). (b) The imposed co-seismic friction change in the megathrust shear zone. The horizontal axis is the along-strike distance, and the vertical axis is the vertical depth. (c) Vertical viscosity profiles at the rupture center, averaged over x = 0–500 km at the pre-seismic stage. With a smaller weak factor ω (and a larger activation volume V), the viscosity η decreases at shallow depth and increases at deep depth. (d) The surface horizontal velocity v_x along a trench-perpendicular profile at the rupture center (y = 0 km), from the long-timescale computation (black dashed line) at the pre-seismic stage (blue solid line). The co-seismic displacements u_x along the same profile are shown in the red solid line. The velocities and co-seismic displacements are for ω = 1 but are similar for other cases with different mantle viscosity profiles (Fig. 4.S3).

Values of dislocation and diffusion creep parameters are listed in Table 4.S1 in the Supplementary Material. We assume a uniform olivine rheology in the upper mantle to maintain a simple model that captures primary controls on geodetic observations. Although the prefactor A is based on values for dry olivine in Karato and Wu, 1993, the weakness factor ω effectively modifies the rheology and partly accounts for the presence of fluids (Hirth and Kohlstedt, 2003; Behr et al., 2022). For the megathrust shear zone, we adopt the wet quartzite dislocation creep rheology in Ranalli, 1995 and ignore diffusion creep, following previous subduction models (e.g., Dinther, Gerya, Dalguer, Mai, et al., 2013; Sobolev and Muldashev, 2017).

The shear modulus is 20 GPa for the wet quartzite material within the megathrust

shear zone, 60 GPa for the upper mantle, and 120 GPa for the lower mantle below 660 km. Near the megathrust shear zone, we consider realistic spatial variations in shear modulus – a low-rigidity overriding plate (40 GPa for x < 400 km and z > -80 km) and a high-rigidity incoming plate (80 GPa for x > -100 km and z > -80 km), following the structure resolved by the inversion in Puel et al., 2024 (Fig. 4.S2). Shear modulus variations further away from the megathrust have negligible influence on either long-term plate motion or post-seismic deformation and therefore are not included in the model.

In addition, the second invariant of the stress tensor τ_{II} is limited by a yield stress determined by the Drucker-Prager criterion:

$$\tau_y = C + \mu\bar{\sigma}, \tag{4.2}$$

where C is the cohesion (100 MPa for the bulk and 10 MPa within the megathrust), μ is the friction coefficient (0.6 for the bulk and initially set to 0.5 within the megathrust), and $\bar{\sigma}$ is the effective normal stress. Assuming materials are non-dilatant, we adopt a non-associated plastic flow law, in which the plastic flow potential is set to τ_{II} (Dinther, Gerya, Dalguer, Corbi, et al., 2013). While the effective normal stress equals lithostatic pressure in the bulk, it is set to 30 MPa with a linear transition to 0 in the shallow 20 km in the megathrust shear zone, to approximate fluid overpressure (Lamb, 2006; Saffer and Tobin, 2011). Consequently, the megathrust shear zone has a substantially lower yield stress than the surrounding bulk, as well as lower viscosity and shear modulus due to the wet quartzite composition.

For each computation, we carefully choose pairs of the weakness factor ω and the activation volume V in the dislocation creep law that respectively adjust viscosities at shallow and deep depth and maintain the overall plate velocity of $\approx$ 7 cm/year (Fig. 4.2d). Specifically, this can be achieved by decreasing ω while simultaneously increasing V, which effectively lowers the viscosity in the shallow asthenosphere layer but strengthens the bottom part of the upper mantle, and vice versa. The values are within a realistic range from laboratory experiments (Karato and Wu, 1993; Ranalli, 1995; Hirth and Kohlstedt, 2003; Dixon and Durham, 2018). The pre-seismic viscosity profiles for each computation (parameterized in terms of the weakness factor ω = 0.25, 0.5, 1, 2) are shown in Fig. 4.2c.

Cross-timescale scheme

We first solve the Stokes system with a long time step size of 4×10^4 years until a steady state is reached to obtain the viscously dominated long-term plate motion

and initial stress. Subsequently, the model is transitioned to short-timescale computations with a time step size of 1 year. (1) Pre-seismic stage: We slightly increase the friction coefficient to 0.55 in the megathrust to create a critical pre-seismic state from the long-term average one. (2) Co-seismic stage: The megathrust friction coefficient is partially dropped to generate an earthquake event, as discussed below. (3) Post-seismic stage: We run the computation for 5 years after the earthquake, which corresponds to the period before the 2015 Illapel earthquake. We do not intend to model the entire seismic cycle, which needs to be spun up to cycle invariance (Mallick, Lambert, and Meade, 2022).

The co-seismic friction change in the megathrust shear zone is shown in Fig. 4.2b. To minimize the computational cost, the domain represents one side of a symmetric rupture, and the earthquake is imposed by reducing the friction to 0.2 in the seismogenic zone (z = -45 to -5 km, with temperatures between 150 and 350 °C) at the rupture center at y = 0. The friction reduction decreases as a Gaussian function with a characteristic length of 200 km in the along-strike direction, and the segment far away from the rupture center experiences no friction change. A Gaussian-shape smoothing factor dependent on y controls the along-strike rupture length. There is a concurrent increase in the friction coefficient in the updip portion with temperatures $<$ 100 °C to approximate the velocity-strengthening effect and a linear transition from 100 and 150 °C, with the along-strike Gaussian smooth factor applied as well. The maximum updip friction coefficient is 0.6 at y = 0 co-seismically. In the downdip direction, although the friction reduction extends to z = -45 km before gradually tapering to zero, the actual maximum depth of the co-seismic stress drop zone is $\approx$ 40 km (Fig. 4.S3), because stresses are dominantly limited by the viscous strength instead of friction in the deeper portion with higher temperatures, and increase during the earthquake due to nonlinear viscosities (Hyndman, Yamano, and Oleskevich, 1997). The friction is immediately restored to pre-seismic values after the earthquake. Parameters are chosen such that the earthquake size and magnitude are comparable to the 2010 Maule earthquake but we only aim to capture the net effects and long-wavelength behavior.

4.3 Results

We select a set of dislocation creep parameters such that all computations produce a consistent long-term velocity of $\approx$ 7 cm/year for the incoming plate (Fig. 4.2d) but different upper mantle viscosity profiles (Fig. 4.2c). In each computation, an asthenosphere layer forms beneath the cold lithosphere, in which the viscosity is

1×10^{19} Pa·s for ω = 2 and 3×10^{18} Pa·s for ω = 0.25 before the earthquake. In the deeper upper mantle, viscosity increases to 10^{20}–10^{21} Pa·s because of the higher lithostatic pressure, and the trade-off between this viscosity gradient and the asthenosphere viscosity maintains a similar plate velocity for each case.

At the pre-seismic stage, surface velocities on both the incoming and overriding plates show horizontal in-plane compression (Fig. 4.2d), consistent with behavior revealed by previous seismic cycle models (Fang, Gurnis, and Lapusta, 2024). Landward velocities of 2–3 cm/year are observed 100–200 km away from the trench on the overriding plate, which is caused by compressional forces from the incoming plate and agrees with pre-seismic deformation rates measured in central Chile (Melnick et al., 2017). On the incoming plate, areas near the trench are 1 cm/year slower than the average plate velocity. The pre-seismic behavior is consistent for cases with different values of ω, which demonstrates viscosity profiles constrained solely by plate motions can be non-unique. The elastically dominated co-seismic deformation is nearly identical for different ω as well (Fig. 4.S4), since changes in mantle viscosity structures do not directly affect stress conditions within the megathrust.

When the earthquake is imposed, surface velocities quickly flip from pre-seismic compression to tension in the ruptured segment: The subducting incoming plate accelerates substantially near the trench with displacements of 3 m, and the overriding plate rebounds seaward up to 25 m (Fig. 4.2d). The key source parameters, an average stress drop of 4 MPa and effective seismic moment of 2.3×10^{22} N·m ($M_w \approx$ 8.8), are comparable to values reported for the 2010 Maule earthquake by previous studies, although the megathrust slip is slightly higher due to a heterogeneous shear modulus structure (e.g., Delouis, Nocquet, and Vallée, 2010; Lay et al., 2010; Pollitz et al., 2011). The dynamic strain-rate-weakening activated by co-seismic displacements in the ruptured segment can reduce viscosities of the asthenosphere beneath the accelerated incoming plate by up to 80% (Fig. 4.3). In the subsequent period, the reduced asthenosphere viscosity partially recovers but remains 30–50% lower than the pre-seismic value. The viscosity changes induced by the earthquake decay in both trench-normal and trench-parallel directions from the rupture center, and vanish in areas > 1000 km away (Fig. 4.3).

Even with consistent co-seismic stress perturbations and displacements, different mantle viscosity profiles lead to diverse post-seismic responses to the earthquake (Fig. 4.4). We define the section with $y \leq 400$ km as the near-field and $y > 400$ km as the far-field. All of these cases show similar near-field deformation patterns after the

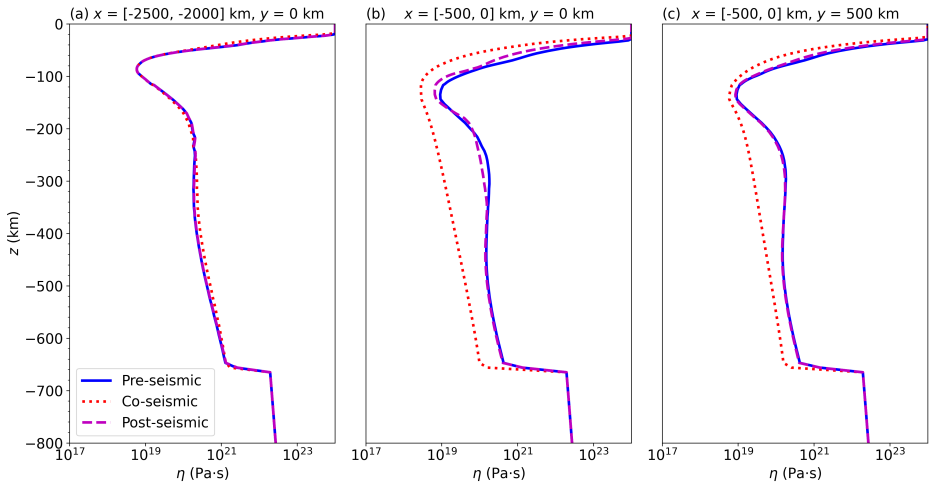

Figure 4.3: Viscosity profiles in different regions of the incoming plate for ω = 1: (a) Averaged over x = [-2500, -2000] km, y = 0 km, within the ruptured segment and far from the trench; (b) x = [-500, 0] km, y = 0 km, within the ruptured segment and near the trench; (c) x = [-500, 0] km, y = 500 km, within the non-ruptured segment and near the trench.

earthquake: the accelerated incoming plate continues moving landward and most inland areas on the overriding plate undergo seaward rebound, although the velocity changes increase as the asthenosphere viscosity decreases. When the asthenosphere viscosity is high (1.5×10^{19} Pa·s, $\omega = 2$), the relative velocity changes in the far-field section are minimal (Fig. 4.4a). In contrast, with a relatively weak asthenosphere (ω = 0.25, 0.5 and 1), ELM emerges in far-field areas near the trench ($y > 400$ km, $x <$ 400 km) on the overriding plate, while the corresponding section on the incoming plate accelerates substantially due to a smaller asthenosphere resistance (Fig. 4.4b–d). The deformation is further amplified by the dynamic reduction in average asthenosphere viscosity beneath the incoming plate in the ruptured segment, from 3.0×10^{18} to 1.3×10^{18} Pa·s for ω = 0.25, from 5.4×10^{18} to 3.1×10^{18} Pa·s for ω = 0.5, and from 9.1×10^{18} to 6.6×10^{18} Pa·s for ω = 1 (Fig. 4.3). In areas further away from the rupture center, the co-seismic and post-seismic strain rate changes are much smaller and the viscosity perturbations are negligible (Fig. 4.3). Additionally, the far-field post-seismic deformation shows a broad divergent pattern with considerable trench-parallel motion away from the rupture center. The ELM signals persist with gradually reduced amplitudes along both the north (increasing y) and east (increasing x) direction, and can eventually reverse to seaward velocity changes in inland areas. These ELM predictions qualitatively match GNSS observations (Melnick et al.,

2017; Yuzariyadi and Heki, 2021) and suggest the crucial role of a relatively weak asthenosphere in producing ELM.

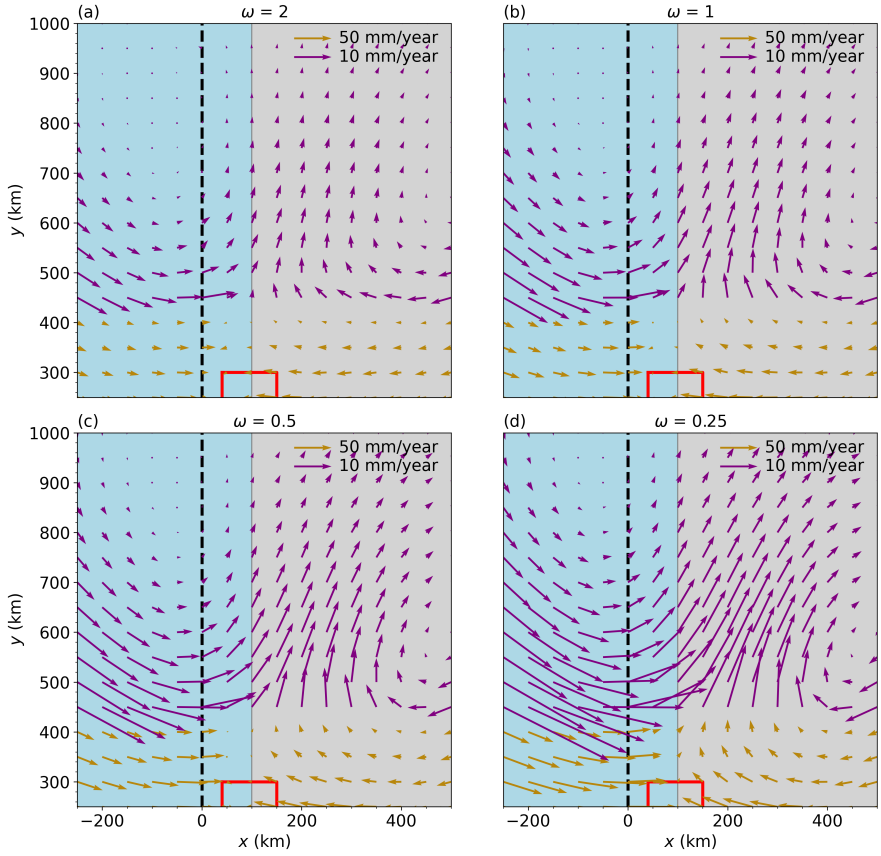

Figure 4.4: Map view of post-seismic surface velocity changes for cases with different mantle viscosity profiles. The post-seismic velocities are averaged over 5 years following the earthquake. Velocity changes in the near-field section ($y \leq 400$ km) and the far-field section ($y > 400$ km) are plotted with different scales.

The predicted ELM amplitudes can be compared with GNSS velocity measurements to constrain the viscosity profile of the underlying mantle. In the along-strike (north-south) direction, ELM was observed in a wide range of distances (500–1000 km) from the epicenter after the 2010 Maule earthquake (Melnick et al., 2017; Yuzariyadi and Heki, 2021), but thereafter was disrupted by the 2015 Illapel earthquake (M_w = 8.3). During the period between these two earthquakes, the landward velocity increase relative to the pre-2010 deformation rate peaked in the y = 550–650 km section at ≈ 5 mm/year (Melnick et al., 2017) (Fig. 4.5). Most GNSS stations that recorded ELM are located within a narrow distance range from the trench (x = 100–200 km), and the data coverage is insufficient for resolving systematic variations in

the trench-normal (west-east) direction, which may be influenced by local material heterogeneity or data noise. We therefore focus on capturing the long-wavelength ELM patterns in the along-strike direction, rather than fitting the sparse observations point by point. The computations with ω = 0.5 and 1 produce far-field post-seismic deformation fields that show good agreement with key characteristics of observations (Fig. 4.5a). The results indicate the viscosity before the earthquake is 5–9 $\times 10^{18}$ Pa·s in the asthenosphere immediately below the lithospheric plate and $\sim 10^{21}$ Pa·s in the deeper part close to the 660 km interface (Fig. 4.5b). The asthenosphere viscosity can be reduced to 3–7 $\times 10^{18}$ Pa·s post-seismically beneath the ruptured segment of the incoming plate, where strain rates remain high (Fig. 4.5b). Computations with higher or lower asthenosphere viscosities fail to account for the amplitude and extent of ELM. With an even weaker asthenosphere (ω = 0.25), the maximum landward velocity change is broadly overestimated, and vice versa. Other viscosity profiles can yield ELM patterns that agree reasonably well with observations, but they fail to reproduce the $\approx$ 7 cm/year motion of the incoming plate (see Text S3 and Figs. 4.S5, 4.S6). While considering only one type of observation can lead to non-unique solutions, combining both plate motion and ELM notably reduces trade-offs and tightens constraints on the nonlinear rheology in the upper mantle.

We conducted additional computations to investigate the influence of the earthquake magnitude and lateral variations in shear modulus in the subduction zone. If the friction decrease in the seismogenic zone (z = -45 to -5 km is reduced by 30% (the friction at y = 0 dropped to 0.3 instead of 0.2), there is a commensurate decrease in the average stress drop from 4 to 3 MPa and seismic moment from 2.3×10^{22} to 1.4×10^{22} N·m. In this scenario, ELM still appears but amplitudes are systematically lower for each viscosity profile (Figs. 5c, d). The results indicate that a smaller earthquake stress drop in the model may lead to a lower asthenosphere viscosity estimate. We also explored the model behavior with a shear modulus of 60 GPa throughout the bulk upper mantle. The high-rigidity block in the incoming plate and the low-rigidity block in the overriding plate is removed, and the shear modulus of the shear zone is still 20 GPa. The plate motion is dominated by viscous behavior and remains largely unchanged. When the same earthquake is imposed (the friction at y = 0 dropped to 0.2), the predicted ELM is also broadly smaller than those from computations with the shear modulus variations but with a similar viscosity profile (Figs. 5e, f). ELM signals can be further underestimated with a large ω. Many post-seismic deformation studies use a homogeneous shear modulus structure, but such an assumption can cause underestimation of the asthenosphere

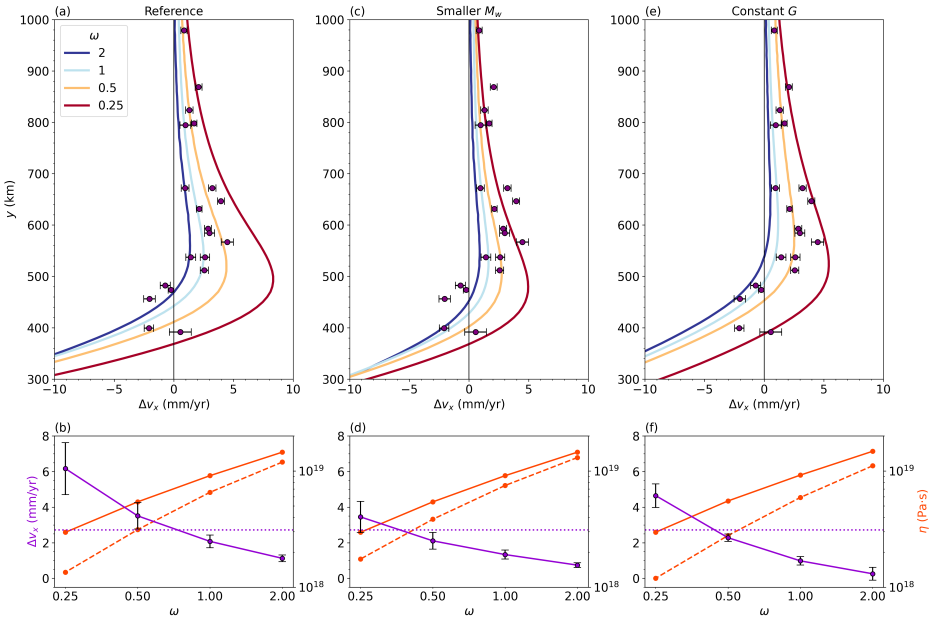

Figure 4.5: (a) Predicted horizontal velocity changes along trench-parallel profiles for computations with different mantle viscosity profiles (solid lines) and observed ELM at local GNSS stations (dots with error bars) during the 5-year post-seismic period. (b) The average ELM in the y = 500–700 km section measured by Melnick et al., 2017 (dotted purple) and predicted by different computations (solid purple), and the minimum viscosity in the asthenosphere pre-seismically (solid orange) and post-seismically (dashed orange). (c, d) Results from computations with a smaller earthquake. (e, f) Results for computations without the lateral spatial variation in shear modulus.

viscosity in this model when the co-seismic stress drop is conserved. These tests confirm the robustness of the model and highlight that accurate estimation of mantle viscosity relies on well-constrained earthquake source properties and shear modulus structures. The rigidity heterogeneity can be reliably resolved by seismic techniques, but is often neglected in studies that attempt to estimate viscoelastic parameters using geodetic data, which can bias deformation predictions and consequently the inferred viscosity profile.

4.4 Discussion

Combining the long-term plate velocity with ELM following a great earthquake improves the uniqueness of inferred mantle viscosity structure, as the long-term signal reflects broader mantle dynamics while ELM provides heightened sensitivity to shallow mantle viscosity. The model matching both observations supports the existence of a low-viscosity layer beneath the lithospheric plate. Similar to Sun,

Wang, and He, 2024, we attribute the ELM to the abrupt change in the plate force balance induced by great earthquakes (Fig. 4.S7). In the non-ruptured segment of the overriding plate, we expect no significant temporal variations in the inter-plate friction and asthenosphere shear stresses, and the post-seismic deformation is predominantly modulated by the competition between the stronger horizontal push and the shear force from the seaward-rebounding ruptured segment. A basal weak layer with lower viscosity results in faster deformation within the incoming plate and hence a more profound horizontal force that modifies force balance and produces ELM on the coupled overriding plate. The computations predict a broad increase in surface velocities of the incoming plate that extends into the non-ruptured segment (Fig. 4.4), which is further amplified by the dynamic viscosity reduction in the asthenosphere beneath the ruptured segment. The emergence of ELM requires an increased horizontal force acting on the overriding plate in an adjacent coupled segment, but that does not necessarily imply enhanced locking, as suggested by some previous studies (e.g., Loveless, 2017; Melnick et al., 2017).

The model naturally generates a low-viscosity layer at a depth of 50–150 km beneath the lithospheric plate with experimentally-constrained olivine dislocation creep parameters uniformly in the upper mantle (Karato and Wu, 1993). The viscosity increases significantly with depth to compensate for low viscosity at shallow depth and permit a long-term plate velocity of several cm/year. This viscosity contrast arises due to the competition between thermal activation and pressure dependence of viscous creep (E and V terms in Eq. 1), and is enhanced by nonlinear strain-rate weakening. The depth-varying viscosity structure shows consistency with seismic constraints (e.g., Lin et al., 2016; Becker, 2017), as well as profiles independently inferred from other geophysical observations such as glacial isostatic adjustment and geoid data (e.g., Mitrovica and Forte, 2004; Mao and Zhong, 2021), although trade-offs may exist between the viscosity and thickness of the asthenosphere. Our estimate of the asthenosphere viscosity ($\sim 10^{18}$ Pa·s) is higher than that from the generic LAB model in Sun, Wang, and He, 2024 ($\sim 10^{17}$ Pa·s for a similar ELM amplitude), because the weakness is averaged over a larger depth range and the nonlinear strain-rate-weakening can dynamically reduce viscosities during the post-seismic period. While the results reflect a low average viscosity within the asthenosphere, they do not exclude the possibility of a persistent thinner layer with additional weakness regulated by local heterogeneities in composition, fluid content, melt fraction or grain size (Ranalli, 1995; Hirth and Kohlstedt, 2003; Dixon, Dixon, et al., 2004), which can be constrained by independent seismic and geochemical

observations. We acknowledge that complications in the thermal and rheological structure in other areas (e.g., the "cold nose" and fluid release processes in the mantle wedge, as discussed in Text S1) may also influence detailed viscosity variations at a local scale.

We have demonstrated that the variability of shear modulus in space also influences amplitudes of post-seismic deformation, including the ELM amplitude. Seismic, geodetic, and geological observations indicate that the shear modulus is higher for the subducting oceanic lithosphere and lower for the overriding plate that hosts weak sediments and is modified by magmatic processes (Stern, 2002; Sagiya and Meneses-Gutierrez, 2022). The effects of such a lateral bimaterial contrast on fault slip models have been investigated (Ma and Beroza, 2008; Williams and Wallace, 2015; Hashima et al., 2016; Ragon and Simons, 2023), and the heterogeneity is further illuminated by inversion from co-seismic slip of the 2011 Tohoku-oki earthquake (Puel et al., 2024). A high-rigidity incoming plate allows slab acceleration to propagate over a larger spatial scale along the plate boundary and applies a stronger push on the coupled overriding plate in non-ruptured segments. Simultaneously, the low rigidity of the overriding plate reduces the shear force between segments, favoring the ELM as well. The limited offshore observations and trade-offs between slip distribution and material properties pose a challenge in accurately quantifying the extent and amplitude of the shear modulus variation (Puel et al., 2024). ELM in our computations is robust despite uncertainties in the shear modulus variations, but additional data will help refine the shear modulus structure and improve our viscosity estimates. Such spatial variations in elastic properties can also be incorporated in other post-seismic studies for two reasons: (1) Elastic properties can be independently constrained using seismological observations from earthquakes with smaller magnitudes occurring locally and globally; (2) The elastic problem is linear and there exist computational frameworks that can handle arbitrary material heterogeneity (Mallick, Lambert, and Meade, 2022).

Post-seismic deformation in the ruptured segment has been used to infer mantle viscosity as well (e.g., Hu, Bürgmann, et al., 2016; Freed et al., 2017; Marsman et al., 2025). Viscosity inferred in near-field areas needs to be interpreted with caution, as they can vary at different stages of a seismic cycle. The mantle viscosity is nonlinear and can be substantially reduced during co-seismic and post-seismic stages (Wang, Hu, and He, 2012; Barbot, 2018; Agata et al., 2019). Models with shorter time steps or transient behavior can show even lower viscosities reduced by several orders of

magnitude immediately after a great earthquake (Sobolev and Muldashev, 2017). Without additional constraints such as long-term plate motions or data from multiple earthquakes, recovering nonlinear rheological parameters solely from post-seismic geodetic observations is subject to non-uniqueness (Mallick, Lambert, and Meade, 2022; Mallick and Simons, 2025). Our computations are able to produce seaward near-field deformation with long-wavelength features reasonably consistent with GNSS time series (Melnick et al., 2017). However, unlike the creep-like long-term motion and far-field deformation, the faster near-field deformation also depends on the initial stress states and pre-seismic coupling, detailed distribution of slip and transient rheology. Integrating the full pattern of post-seismic deformation requires careful distinction between contributions from afterslip on the megathrust and bulk viscoelastic processes in different areas (e.g., the mantle wedge and the underlying asthenosphere) (Bedford et al., 2016; Barbot, 2018; Sun, Wang, and He, 2024). Megathrust rupture zone heals after the earthquake, and it has been shown that relocking or continued slip on the fault can also significantly influence near-field post-seismic deformation (Govers et al., 2018; D'Acquisto and Govers, 2023). While these complexities are beyond the scope of this study, our tests indicate that deformation in the non-ruptured segments is unlikely to be highly sensitive to such details within the ruptured segment (Figs. 4.S8, 4.S9), as they are not dominant factors in the force balance.

Despite a simplified model setup, we have established a framework for constraining mantle viscosity structures using multi-scale geodetic observations in regions where megathrust earthquakes occurred. Clear ELM signals have been observed following other sufficiently large megathrust earthquakes, e.g., the 2003 Tokachi-oki earthquake (M_w = 8.3), the 2011 Tohoku-oki earthquake (M_w = 9.1), the 2014 Iquique earthquake (M_w = 8.2), and the 2015 Illapel earthquake (M_w = 8.3) (Heki and Mitsui, 2013; Yuzariyadi and Heki, 2021). The ELM amplitude generally increases for larger events, which may be activated by the strongly weakened asthenosphere. While progressing toward more accurate, location-specific viscosity estimates in subduction zones is promising, there are several limitations of the current model. We did not consider the compressibility of mantle and the vertical motion on the surface due to limitations in available software capacity. Their influence is likely minor because we focus on the slow, creep-like long-term motion and far-field post-seismic deformation. Along-strike geometrical complexities such as the curved plate boundaries, as well as the interference between multiple earthquakes in the same region, may also modulate ELM locally. For example, a large portion of the

apparent ELM following the 2015 Illapel earthquake results from the decay of the seaward post-seismic slip of the 2010 Maule earthquake that ruptured that segment 5 years earlier, which can be observed from GNSS time series from Melnick et al., 2017. Advances in software and computational resources in the near future will enable us to more comprehensively resolve spatial and temporal complexities of plate motions and post-seismic deformation.

4.5 Conclusions

The cross-scale approach we developed reconciles olivine viscosity parameters derived from laboratory experiments, the long-term velocity of the Nazca Plate, and far-field post-seismic deformation after a great megathrust earthquake in the Chilean subduction zone. We explored different upper mantle viscosity profiles, and our preferred model simultaneously predicts the $\approx$ 7 cm/year motion of the subducting Nazca Plate and ELM up to 5 mm/year at along-strike distances of 500–1000 km from the rupture center, consistent with geodetic observations. The results suggest a pre-seismic viscosity of 5–9 $\times 10^{18}$ Pa·s in the asthenosphere layer at 100 km depth and $\sim$ 10^{21} Pa·s at 660 km depth. The asthenosphere viscosity can be dynamically reduced by 30–50% at the post-seismic stage. The broad increase in deformation rates within and below the incoming plate after a megathrust earthquake leads to the emergence of ELM on the overriding plate in adjacent coupled segments. This acceleration requires a relatively low-viscosity asthenosphere layer below the lithospheric plate and is further amplified by the viscosity reduction due to nonlinear strain-rate-weakening in the upper mantle. We have also demonstrated the importance of reliably-constrained co-seismic stress drop and shear modulus structure in subduction zones in the prediction of ELM and inference of mantle viscosity. By taking multi-scale geodetic observations as constraints, we are able to eliminate the trade-offs between viscosities at different depths that arise when only long-term plate velocities are used and obtain more accurate estimates of the nonlinear mantle rheological parameters.

Supplementary material

Text S1. Thermal structure

The thermal structure in the model is pre-defined following the workflow described in Text S2 of Fang, Gurnis, and Lapusta (2024). Temperatures within and beneath the incoming plate from the ridge to the trench are calculated using a half-space cooling model assuming a plate velocity of 7 cm/year (consistent with the actual plate

velocity), a plate age of 50 million years at the trench, a thermal diffusivity of 10^{-6} m^2/s, and a mantle potential temperature of 1700 K. Temperature profiles for the overriding plate and the underlying mantle are calculated based on half-space cooling at a cooling age of 80 million years. The depth of the slab interface is determined by interpolating the Slab2 model (Hayes et al., 2018) along a trench-normal profile at 36 °S. For each profile perpendicular to the slab interface, temperatures are calculated assuming a 1D thermal diffusion starting from the reference profile before subduction, i.e., the vertical temperature profile of the incoming plate at the trench at an age of 50 million years. The diffusion time is equal to the along-dip distance divided by the plate velocity of 7 cm/year. Linear smoothing is applied in the buffer zone surrounding the slab, which is twice the width of the zone with temperatures below 1630 K. An adiabatic temperature gradient of 0.3 °SC/km is added (Behr et al., 2022). The code for building the temperature field is available on Zenodo (see Data Availability section of Fang, Gurnis, and Mallick (2025)).

The geometry and thermal thickness of the incoming plate and the slab are largely consistent with those used in previous studies (e.g., Keken (2003), Dinther, Gerya, Dalguer, Mai, et al. (2013), and Sobolev and Muldashev (2017)). The thermal structure we established for the mantle wedge is simplified in that it does not account for the cooling near the slab interface, resulting in the absence of the "cold nose". We also note that it is the viscosity jointly controlled by the thermal structure and rheological properties that ultimately governs the model behavior. The mantle wedge is also subject to dehydration and fluid release processes, which can reduce the local viscosity and counteract the effects of low temperature (Billen and Gurnis, 2001; Hirth and Kohlstedt, 2003; Keken, 2003). The combined effects and detailed viscosity variations remain uncertain (Keken and Wilson, 2023). Our model focuses on the influence of asthenosphere viscosity beneath the incoming plate and we simplify the complication in this aspect.

Text S2. Dislocation and diffusion creep laws

Viscosities in the bulk upper mantle are governed by a composite creep law with dislocation and diffusion creep:

$$\eta = \left(\frac{1}{\eta_{disl}} + \frac{1}{\eta_{diff}} \right)^{-1} \tag{4.S1}$$

in which η_{disl} and η_{diff} are given by Eq. 1 in the main text. In the lower mantle below 660 km depth, viscosities are only controlled by diffusion creep and have minimal influence on the model behavior. Parameters for the bulk upper mantle,

shear zone and lower mantle are adapted from values for dry olivine in Karato and Wu (1993), wet quartzite in Ranalli (1995) and lower mantle material in Behr et al. (2022), respectively, which are listed in Table 1. The activation volume for dislocation creep in the bulk upper mantle is 7.8 $cm^3 \cdot mol^{-1}$1 for a weakness factor ω = 2, 10.6 $cm^3 \cdot mol^{-1}$ for ω = 1, 13.4 $cm^3 \cdot mol^{-1}$ for ω = 0.5 and 16.1 $cm^3 \cdot mol^{-1}$ for ω = 0.25. Computations with each pair of the weakness factor and activation volume produce a consistent plate velocity of 7 cm/year (Fig. 4.S1).

Table 4.S1: Dislocation and diffusion creep parameters.

Quantity	Symbol	Unit	Bulk value	Shear zone value	Lower mantle value
Dislocation creep					
Exponent	n	—	3.5	2.3	—
Prefactor	A	$Pa^{-n} \cdot s^{-1}$	2.73×10^{-15}	3.13×10^{-17}	
Activation energy	E	$kJ \cdot mol^{-1}$	540	154	—
Activation volume	V	$cm^3 \cdot mol^{-1}$	7.8–16.1	10	—
Weakness factor	ω	—	0.25–2	1	—
Diffusion creep					
Exponent	n	—	1.0	—	1.0
Prefactor	A	$Pa^{-n} \cdot s^{-1}$	1.40×10^{-11}	—	5.80×10^{-13}
Activation energy	E	$kJ \cdot mol^{-1}$	300	—	300
Activation volume	V	$cm^3 \cdot mol^{-1}$	6	—	3
Weakness factor	ω	—	1	—	1

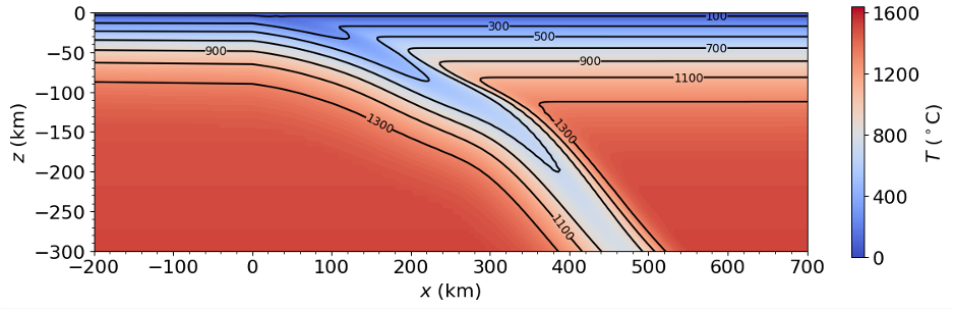

Figure 4.S1: Thermal structure zoomed in near the megathrust.

Text S3. Additional computations predicting similar enhanced landward motion (ELM) but different plate motions

We computed the model with alternative pairs of the weakness factor ω and the activation volume V: (1) ω = 1.55 and V = 7.8 $cm^3 \cdot mol^{-1}$; (2) ω = 0.63 and V = 16.1 $cm^3 \cdot mol^{-1}$. These two cases can produce enhanced landward motion (ELM) similar to that in the reference case with ω = 1 and V = 13.4 $cm^3 \cdot mol^{-1}$ but fail

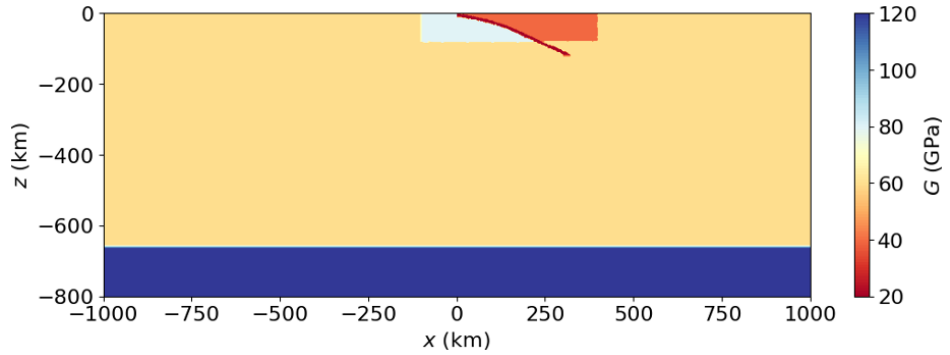

Figure 4.S2: Shear modulus structure used in the reference model in the section with x = [-1000, 1000] km. Outside this region, the shear modulus is 60 GPa in the upper mantle and 120 GPa in the lower mantle.

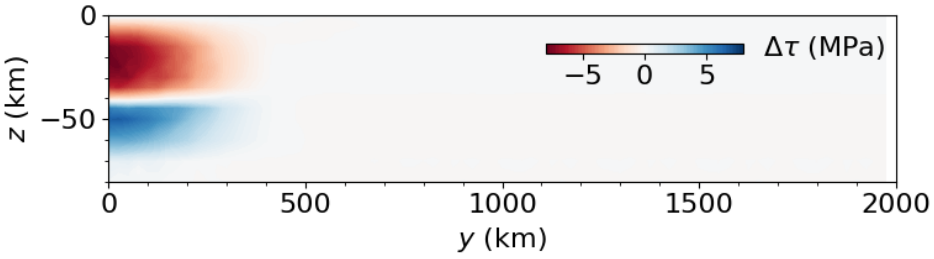

Figure 4.S3: Co-seismic stress changes in the megathrust shear zone. The horizontal axis is the along-strike distance, and the vertical axis is the vertical depth.

to match the plate velocity of 7 cm/year (Fig. S5). The results confirm that plate motion is controlled by viscosities throughout the entire upper mantle, while the far-field plate motion is primarily sensitive to viscosities in the shallow layer. The relationship between the weakness factor ω and the activation volume V for similar ELM differs from that required for the 7 cm/year motion of the incoming plate (Fig. S6). Combining both observations provides tighter constraints on the parameter space.

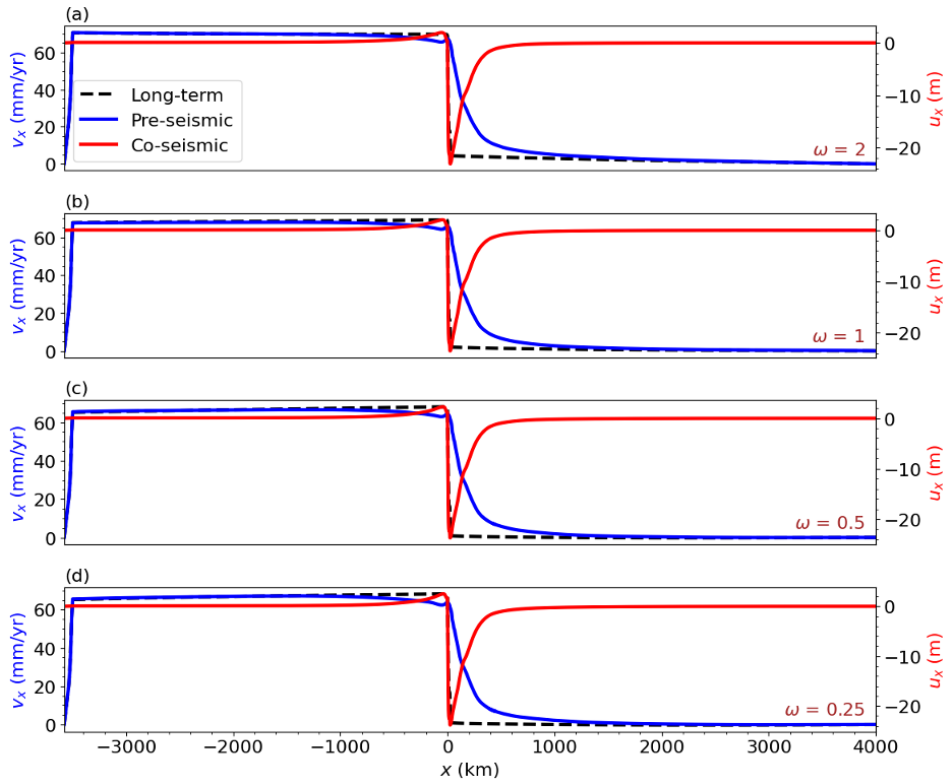

Figure 4.S4: For different weakness factors ω, the surface horizontal velocity v_x along a trench-perpendicular profile at the rupture center (y = 0 km), from the long-timescale computation (black dashed line) at the pre-seismic stage (blue solid line), and the co-seismic displacements u_x along the same profile are shown in the red solid line, akin to Fig. 4.2d.

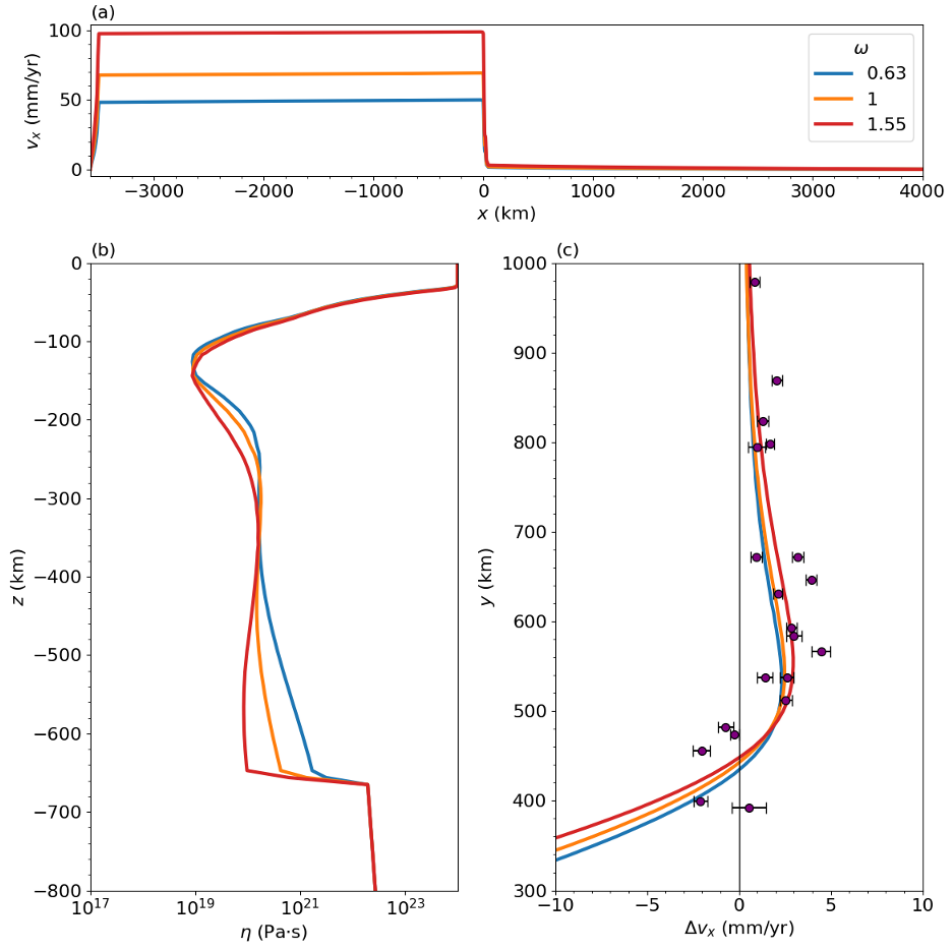

Figure 4.S5: Computations with different pairs of the weakness factor ω and the activation volume V that can produce similar enhanced landward motion (ELM) patterns: (a) The surface horizontal velocity v_x along a trench-perpendicular profile at the rupture center (y = 0 km), from the long-timescale computation, akin to the black dashed line in Fig. 4.2d; (b) Viscosity profiles averaged over x = [-500, 0] km, y = 0 km, akin to the blue solid line in Fig. 4.3b; (c) Predicted horizontal velocity changes along trench-parallel profiles (solid lines) and observed ELM at local GNSS stations (dots with error bars) during the 5-year post-seismic period, akin to Fig. 4.5a.

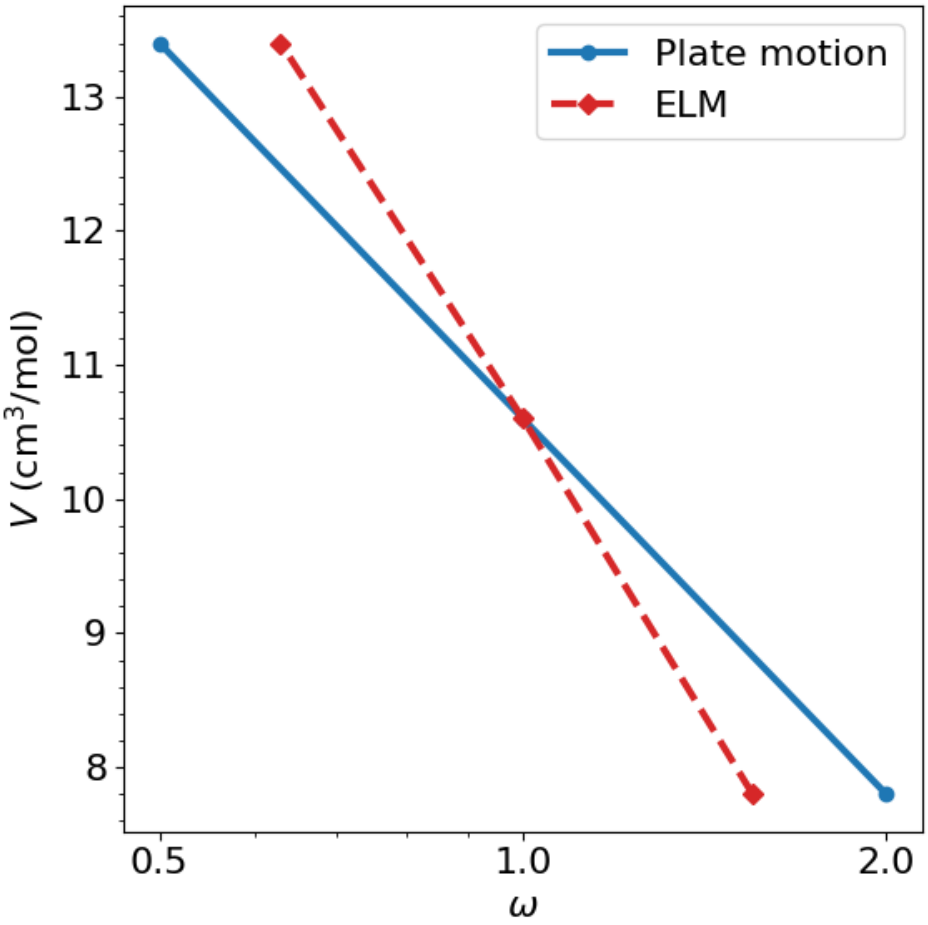

Figure 4.S6: Values of the weakness factor ω and the activation volume V required for similar ELM (red dashed) and the 7 cm/year motion of the incoming plate (blue solid). Combining both observations provides tighter constraints on the parameter space.

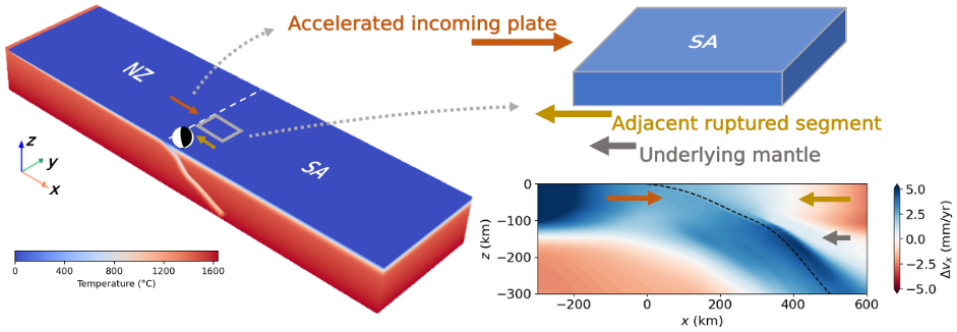

Figure 4.S7: The force balance in the adjacent segment. The post-seismic deformation in the non-ruptured segment is modulated by the horizontal push from the accelerated incoming plate, the shear force from the seaward-rebounding ruptured segment and the underlying mantle. The bottom right plot shows changes in horizontal velocities near the megathrust in the segment (y = 500–700 km) at the post-seismic stage. The incoming plate experiences substantially faster deformation and provides the dominant force that produces ELM.

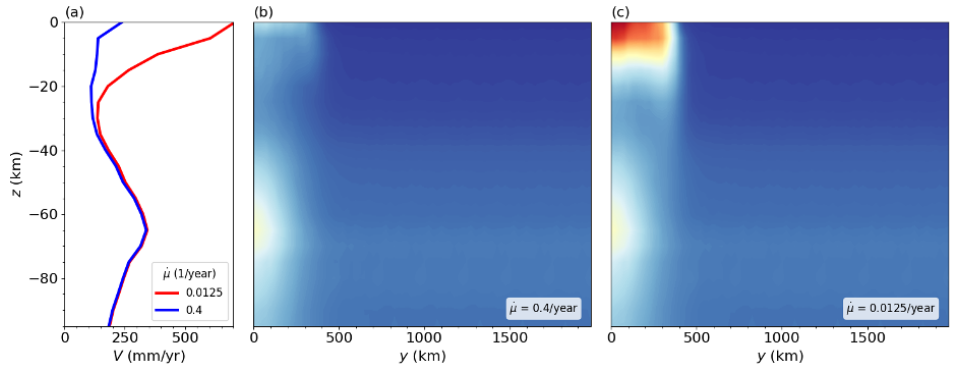

Figure 4.S8: (a) Average post-seismic slip velocity in the megathrust shear zone at the rupture center. (b, c) Distribution of average post-seismic slip velocity in the megathrust for different rates of friction increase. The computations use $\omega = 1$ and $V = 13.4$ cm^3·mol^{-1}, and the slip velocity is measured in the first year after the earthquake.

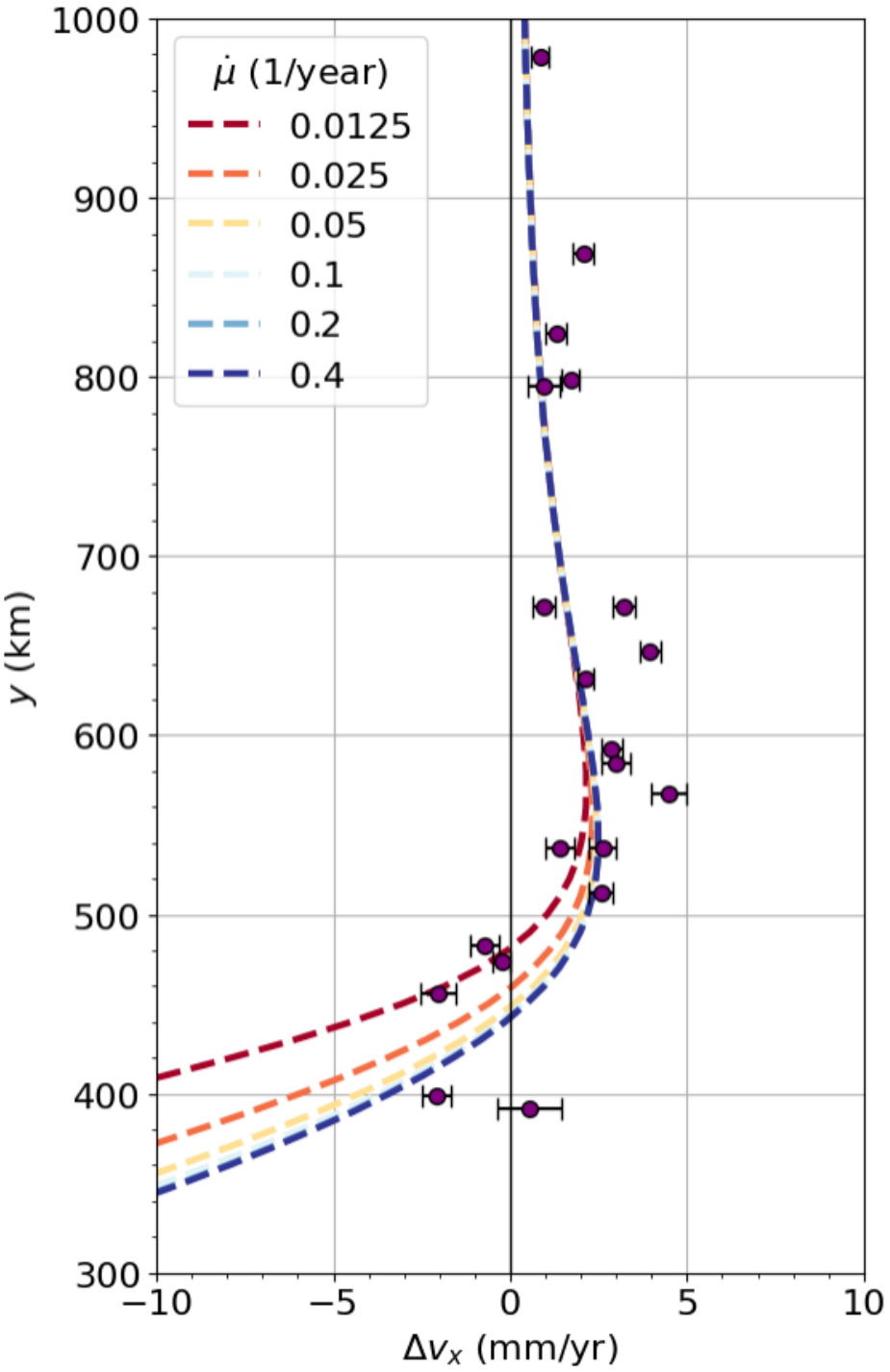

Figure 4.S9: Predicted horizontal velocity changes along trench-parallel profiles with different rates of friction increase (dashed lines) and observed ELM at local GNSS stations (dots with error bars) during the 5-year post-seismic period, akin to Fig. 4.5a. The computations use $\omega = 1$ and $V = 13.4$ cm^3·mol^{-1}. The results show far-field post-seismic deformation in adjacent segments where plates remain coupled is largely insensitive to the fault healing and continued slip in the rupture zone, unless the rupture zone remains substantially weakened.

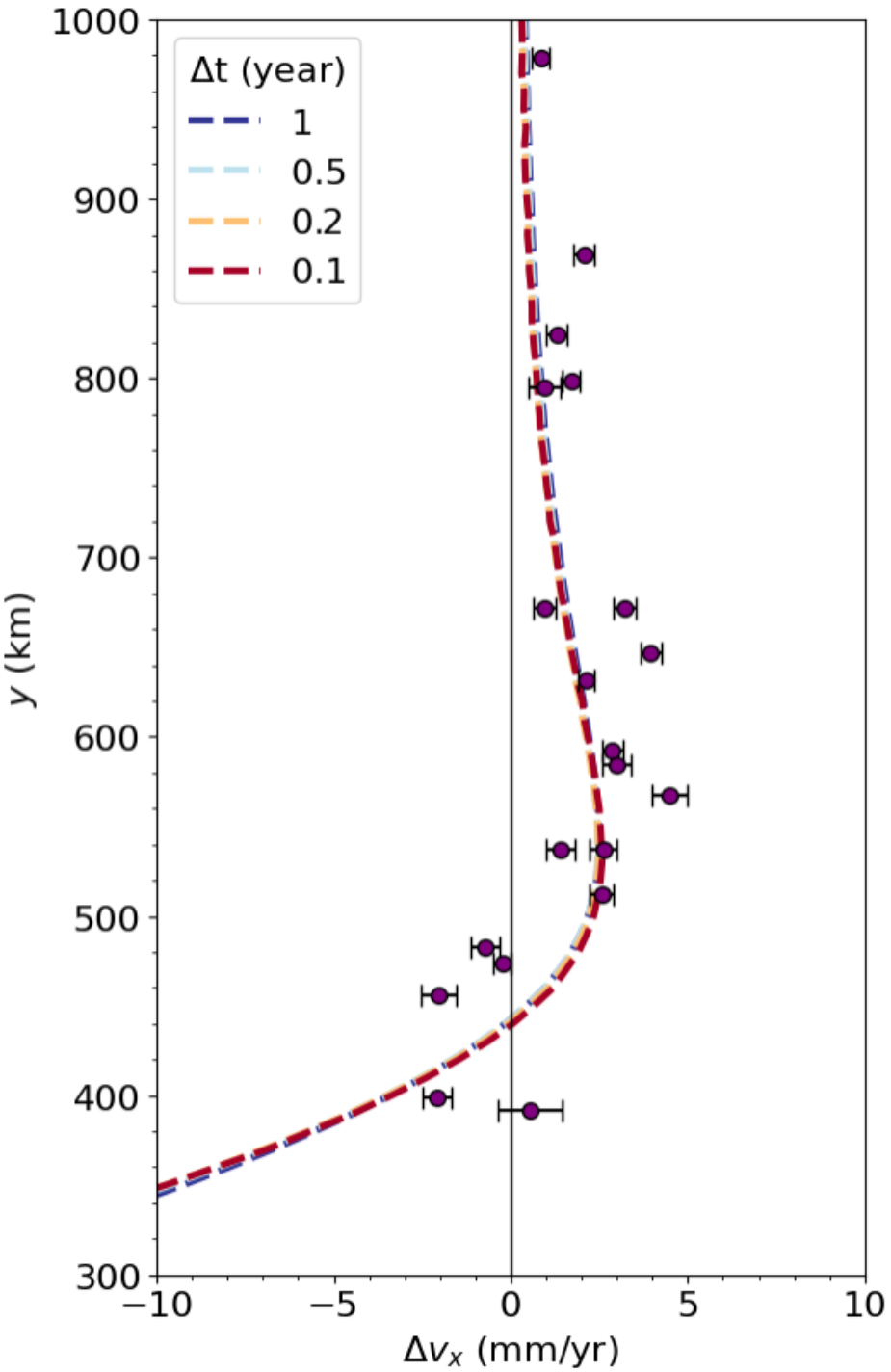

Figure 4.S10: Predicted horizontal velocity changes along trench-parallel profiles with different computational time steps (dashed lines) and observed ELM at local GNSS stations (dots with error bars) during the 5-year post-seismic period, akin to Fig. 4.5a. The computations use $\omega = 1$ and $V = 13.4$ cm^3·mol^{-1}. The consistency between predictions for different time step sizes confirms the robustness of the model.

References

Agata, Ryoichiro et al. (2019). "Rapid mantle flow with power-law creep explains deformation after the 2011 Tohoku mega-quake". In: *Nature Communications* 10.1, p. 1385.

Alisic, Laura et al. (2012). "Multi-scale dynamics and rheology of mantle flow with plates". In: *Journal of Geophysical Research: Solid Earth* 117.B10.

Altamimi, Zuheir et al. (2017). "ITRF2014 plate motion model". In: *Geophysical Journal International* 209.3, pp. 1906–1912.

Barbot, Sylvain (2018). "Asthenosphere flow modulated by megathrust earthquake cycles". In: *Geophysical Research Letters* 45.12, pp. 6018–6031.

Becker, Thorsten W (2017). "Superweak asthenosphere in light of upper mantle seismic anisotropy". In: *Geochemistry, Geophysics, Geosystems* 18.5, pp. 1986–2003.

Bedford, Jonathan et al. (2016). "Separating rapid relocking, afterslip, and viscoelastic relaxation: An application of the postseismic straightening method to the Maule 2010 cGPS". In: *Journal of Geophysical Research: Solid Earth* 121.10, pp. 7618–7638.

Behr, Whitney M et al. (2022). "The effects of plate interface rheology on subduction kinematics and dynamics". In: *Geophysical Journal International* 230.2, pp. 796–812.

Billen, Magali I and Michael Gurnis (2001). "A low viscosity wedge in subduction zones". In: *Earth and Planetary Science Letters* 193.1-2, pp. 227–236.

Cathles, Lawrence M (1975). *Viscosity of the Earth's Mantle*. Princeton University Press.

Conrad, Clinton P and Bradford H Hager (1999). "Effects of plate bending and fault strength at subduction zones on plate dynamics". In: *Journal of Geophysical Research: Solid Earth* 104.B8, pp. 17551–17571.

Corbi, F et al. (2022). "Probing the seismic cycle timing with coseismic twisting of subduction margins". In: *Nature Communications* 13.1, p. 1911.

D'Acquisto, Mario and Rob Govers (2023). "Offshore landward motion shortly after a subduction earthquake implies rapid relocking of the shallow megathrust". In: *Geophysical Research Letters* 50.1, e2022GL101638.

D'Acquisto, Mario, MW Herman, et al. (2023). "Can Plate Bending Explain the Observed Faster Landward Motion of Lateral Regions of the Subduction Zone After Major Megathrust Earthquakes?" In: *Journal of Geophysical Research: Solid Earth* 128.3, e2022JB025431.

Delouis, Bertrand, Jean-Mathieu Nocquet, and Martin Vallée (2010). "Slip distribution of the February 27, 2010 Mw= 8.8 Maule earthquake, central Chile, from static and high-rate GPS, InSAR, and broadband teleseismic data". In: *Geophysical Research Letters* 37.17.

DeMets, Charles, Richard G Gordon, and Donald F Argus (2010). "Geologically current plate motions". In: *Geophysical journal international* 181.1, pp. 1–80.

Dinther, Y van, TV Gerya, LA Dalguer, Paul Martin Mai, et al. (2013). "The seismic cycle at subduction thrusts: Insights from seismo-thermo-mechanical models". In: *Journal of Geophysical Research: Solid Earth* 118.12, pp. 6183–6202.

Dinther, Y van, TV Gerya, Luis A Dalguer, Fabio Corbi, et al. (2013). "The seismic cycle at subduction thrusts: 2. Dynamic implications of geodynamic simulations validated with laboratory models". In: *Journal of Geophysical Research: Solid Earth* 118.4, pp. 1502–1525.

Dixon, Jacqueline E, Timothy H Dixon, et al. (2004). "Lateral variation in upper mantle viscosity: role of water". In: *Earth and Planetary Science Letters* 222.2, pp. 451–467.

Dixon, Nathaniel A and William B Durham (2018). "Measurement of activation volume for creep of dry olivine at upper-mantle conditions". In: *Journal of Geophysical Research: Solid Earth* 123.10, pp. 8459–8473.

Fang, Jiaqi, Michael Gurnis, and Nadia Lapusta (2024). "Dynamic emergence of plate motions and great megathrust earthquakes across length and time scales". In: *Geophysical Research Letters* 51.22, e2024GL110821. DOI: 10.1029/2024GL110821.

Fang, Jiaqi, Michael Gurnis, and Rishav Mallick (2025). "Constraints on nonlinear mantle rheology from multi-scale geodetic observations of plate motion and postseismic enhanced landward motion". In: *Earth and Planetary Science Letters* 669, p. 119566. DOI: 10.1016/j.epsl.2025.119566.

Farrington, RJ, L-N Moresi, and Fabio Antonio Capitanio (2014). "The role of viscoelasticity in subducting plates". In: *Geochemistry, Geophysics, Geosystems* 15.11, pp. 4291–4304.

Forte, AM, WR Peltier, and AM Dziewonski (1991). "Inferences of mantle viscosity from tectonic plate velocities". In: *Geophysical Research Letters* 18.9, pp. 1747–1750.

Freed, Andrew M et al. (2017). "Resolving depth-dependent subduction zone viscosity and afterslip from postseismic displacements following the 2011 Tohoku-oki, Japan earthquake". In: *Earth and Planetary Science Letters* 459, pp. 279–290.

Govers, R et al. (2018). "The geodetic signature of the earthquake cycle at subduction zones: Model constraints on the deep processes". In: *Reviews of Geophysics* 56.1, pp. 6–49.

Hager, Bradford H (1984). “Subducted slabs and the geoid: Constraints on mantle rheology and flow”. In: *Journal of Geophysical Research: Solid Earth* 89.B7, pp. 6003–6015.

Han, Shunjie et al. (2024). “The persisting conundrum of mantle viscosity inferred from mantle convection and glacial isostatic adjustment processes”. In: *Earth and Planetary Science Letters* 648, p. 119069.

Hashima, Akinori et al. (2016). “Coseismic deformation due to the 2011 Tohoku-oki earthquake: influence of 3-D elastic structure around Japan”. In: *Earth, Planets and Space* 68, pp. 1–15.

Hayes, Gavin P et al. (2018). “Slab2, a comprehensive subduction zone geometry model”. In: *Science* 362.6410, pp. 58–61.

Heki, Kosuke and Yuta Mitsui (2013). “Accelerated pacific plate subduction following interplate thrust earthquakes at the Japan trench”. In: *Earth and Planetary Science Letters* 363, pp. 44–49.

Hirth, Greg and D Kohlstedt (2003). “Rheology of the upper mantle and the mantle wedge: A view from the experimentalists”. In: *Geophysical monograph-american geophysical union* 138, pp. 83–106.

Hu, Jiashun, Johann Rudi, et al. (2024). “Constraining Earth’s nonlinear mantle viscosity using plate-boundary resolving global inversions”. In: *Proceedings of the National Academy of Sciences* 121.28, e2318706121.

Hu, Yan, Roland Bürgmann, et al. (2016). “Asthenosphere rheology inferred from observations of the 2012 Indian Ocean earthquake”. In: *Nature* 538.7625, pp. 368–372.

Hyndman, Roy D, Makoto Yamano, and Dan A Oleskevich (1997). “The seismogenic zone of subduction thrust faults”. In: *Island Arc* 6.3, pp. 244–260.

Jarrin, Paul et al. (2023). “Current motion and deformation of the Nazca Plate: new constraints from GPS measurements”. In: *Geophysical Journal International* 232.2, pp. 842–863.

Karato, Shun-ichiro and Patrick Wu (1993). “Rheology of the upper mantle: A synthesis”. In: *Science* 260.5109, pp. 771–778.

Keken, Peter E van (2003). “The structure and dynamics of the mantle wedge”. In: *Earth and planetary science letters* 215.3-4, pp. 323–338.

Keken, Peter E van and Cian R Wilson (2023). “An introductory review of the thermal structure of subduction zones: III—Comparison between models and observations”. In: *Progress in Earth and Planetary Science* 10.1, p. 57.

King, Scott D (1995). “The viscosity structure of the mantle”. In: *Reviews of Geophysics* 33.S1, pp. 11–17.

Köhne, Tobias, Rishav Mallick, and Mark Simons (2025). "Probabilistic estimation of rheological properties in subduction zones using sequences of earthquakes and aseismic slip". In: *Earth, Planets and Space* 77.1, p. 3.

Lamb, Simon (2006). "Shear stresses on megathrusts: Implications for mountain building behind subduction zones". In: *Journal of Geophysical Research: Solid Earth* 111.B7.

Lau, Harriet CP et al. (2021). "Frequency dependent mantle viscoelasticity via the complex viscosity: Cases from Antarctica". In: *Journal of Geophysical Research: Solid Earth* 126.11, e2021JB022622.

Lay, T et al. (2010). "Teleseismic inversion for rupture process of the 27 February 2010 Chile (Mw 8.8) earthquake". In: *Geophysical Research Letters* 37.13.

Li, Yida and Michael Gurnis (2023). "A simple force balance model of subduction initiation". In: *Geophysical Journal International* 232.1, pp. 128–146.

Lin, Pei-Ying Patty et al. (2016). "High-resolution seismic constraints on flow dynamics in the oceanic asthenosphere". In: *Nature* 535.7613, pp. 538–541.

Loveless, John P (2017). "Super-interseismic periods: Redefining earthquake recurrence". In: *Geophysical Research Letters* 44.3, pp. 1329–1332.

Ma, Shuo and Gregory C Beroza (2008). "Rupture dynamics on a bimaterial interface for dipping faults". In: *Bulletin of the Seismological Society of America* 98.4, pp. 1642–1658.

Mallick, Rishav, Valere Lambert, and Brendan Meade (2022). "On the choice and implications of rheologies that maintain kinematic and dynamic consistency over the entire earthquake cycle". In: *Journal of Geophysical Research: Solid Earth* 127.9, e2022JB024683.

Mallick, Rishav and Mark Simons (2025). "Limits on inferring an effective lithospheric rheology from geodetic observations of the earthquake cycle". In: *Earth, Planets and Space* 77.1, pp. 1–15.

Mansour, John A et al. (Aug. 2020). *Underworld2: Python Geodynamics Modelling for Desktop, HPC and Cloud*. Software. Version v2.10.0b. DOI: 10.5281/zenodo.3975252. URL: https://doi.org/10.5281/zenodo.3975252.

Mao, Wei and Shijie Zhong (2021). "Constraints on mantle viscosity from intermediate-wavelength geoid anomalies in mantle convection models with plate motion history". In: *Journal of Geophysical Research: Solid Earth* 126.4, e2020JB021561.

Marsman, CP et al. (2025). "Unraveling processes and rheology of the Tohoku earthquake cycle using bayesian inference". In: *Journal of Geophysical Research: Solid Earth* 130.5, e2024JB029665.

Melnick, Daniel et al. (2017). "The super-interseismic phase of the megathrust earthquake cycle in Chile". In: *Geophysical Research Letters* 44.2, pp. 784–791.

Mitrovica, JX and AM Forte (2004). "A new inference of mantle viscosity based upon joint inversion of convection and glacial isostatic adjustment data". In: *Earth and Planetary Science Letters* 225.1-2, pp. 177–189.

Moresi, Louis, Frédéric Dufour, and H-B Mühlhaus (2002). "Mantle convection modeling with viscoelastic/brittle lithosphere: Numerical methodology and plate tectonic modeling". In: *Pure and applied Geophysics* 159, pp. 2335–2356.

Oryan, Bar and W Roger Buck (2020). "Larger tsunamis from megathrust earthquakes where slab dip is reduced". In: *Nature Geoscience* 13.4, pp. 319–324.

Perfettini, H and J-P Avouac (2004). "Postseismic relaxation driven by brittle creep: A possible mechanism to reconcile geodetic measurements and the decay rate of aftershocks, application to the Chi-Chi earthquake, Taiwan". In: *Journal of Geophysical Research: Solid Earth* 109.B2.

Pollitz, Fred F et al. (2011). "Coseismic slip distribution of the February 27, 2010 Mw 8.8 Maule, Chile earthquake". In: *Geophysical Research Letters* 38.9.

Puel, Simone et al. (2024). "Volcanic arc rigidity variations illuminated by coseismic deformation of the 2011 Tohoku-oki M9". In: *Science Advances* 10.23, eadl4264.

Ragon, Théa and Mark Simons (2023). "A secondary zone of uplift measured after megathrust earthquakes: Caused by early downdip afterslip?" In: *Geophysical Research Letters* 50.7, e2022GL101510.

Ranalli, Giorgio (1995). *Rheology of the Earth*. Springer Science & Business Media.

Rudi, Johann, Michael Gurnis, and Georg Stadler (2022). "Simultaneous inference of plate boundary stresses and mantle rheology using adjoints: large-scale 2-D models". In: *Geophysical Journal International* 231.1, pp. 597–614.

Ruiz, Sergio and Raúl Madariaga (2018). "Historical and recent large megathrust earthquakes in Chile". In: *Tectonophysics* 733, pp. 37–56.

Saffer, Demian M and Harold J Tobin (2011). "Hydrogeology and mechanics of subduction zone forearcs: Fluid flow and pore pressure". In: *Annual Review of Earth and Planetary Sciences* 39, pp. 157–186.

Sagiya, Takeshi and Angela Meneses-Gutierrez (2022). "Geodetic and geological deformation of the Island arc in Northeast Japan revealed by the 2011 Tohoku earthquake". In: *Annual Review of Earth and Planetary Sciences* 50.1, pp. 345–368.

Sobolev, Stephan V and Iskander A Muldashev (2017). "Modeling seismic cycles of great megathrust earthquakes across the scales with focus at postseismic phase". In: *Geochemistry, Geophysics, Geosystems* 18.12, pp. 4387–4408.

Solomatov, VS and L-N Moresi (1997). "Three regimes of mantle convection with non-Newtonian viscosity and stagnant lid convection on the terrestrial planets". In: *Geophysical Research Letters* 24.15, pp. 1907–1910.

Stern, Robert J (2002). “Subduction zones”. In: *Reviews of geophysics* 40.4, pp. 3–1.

Sun, Tianhaozhe, Kelin Wang, and Jiangheng He (2024). “Geodetic signature of a weak lithosphere-asthenosphere boundary in postseismic deformation of large subduction earthquakes”. In: *Earth and Planetary Science Letters* 630, p. 118619.

Sun, Tianhaozhe, Kelin Wang, Takeshi Iinuma, et al. (2014). “Prevalence of viscoelastic relaxation after the 2011 Tohoku-oki earthquake”. In: *Nature* 514.7520, pp. 84–87.

Wang, Kelin, Yan Hu, and Jiangheng He (2012). “Deformation cycles of subduction earthquakes in a viscoelastic Earth”. In: *Nature* 484.7394, pp. 327–332.

Williams, Charles A and Laura M Wallace (2015). “Effects of material property variations on slip estimates for subduction interface slow-slip events”. In: *Geophysical Research Letters* 42.4, pp. 1113–1121.

Yang, Haibin et al. (2023). “Numerical Modeling of Earthquake Cycles Based On Navier-Stokes Equations With Viscoelastic-Plasticity Rheology”. In: *Geochemistry, Geophysics, Geosystems* 24.9, e2023GC010872.

Yuzariyadi, Mohammad and Kosuke Heki (2021). “Enhancement of interplate coupling in adjacent segments after recent megathrust earthquakes”. In: *Tectonophysics* 801, p. 228719.

Zhong, Shijie, Michael Gurnis, and Louis Moresi (1998). “Role of faults, nonlinear rheology, and viscosity structure in generating plates from instantaneous mantle flow models”. In: *Journal of Geophysical Research: Solid Earth* 103.B7, pp. 15255–15268.

Chapter 5

ADVANCED COMPUTATIONAL MODELS OF PLATE MOTIONS AND GREAT MEGATHRUST EARTHQUAKES

5.1 Introduction

Deformation of Earth's surface encompasses a wide spectrum of steady and transient processes, ranging from slow background plate motions to rapid earthquake-related perturbations. Long-term geodetic measurements and geological reconstructions reveal a coherent pattern of quasi-rigid plates moving at several centimeters per year and separated by narrow zones of intense deformation at plate boundaries (DeMets, Gordon, and Argus, 2010; Argus, Gordon, and DeMets, 2011; Kreemer, Blewitt, and Klein, 2014). In contrast, geodetic time series capture short-term temporal variations across seismic cycles, including coseismic and postseismic deformation (Pollitz, 1992; Perfettini and Avouac, 2004; Ozawa et al., 2011; Wang, Hu, and He, 2012; Sun, Wang, Iinuma, et al., 2014). Particularly, great earthquakes at subduction zone megathrust faults produce the largest perturbations to the background surface velocities and stress fields. Although these perturbations decay over time, they can persist in a broad region for years to decades during the postseismic period and complicate the interpretation of geodetic data (Wang, Hu, and He, 2012; Freed et al., 2017). Consequently, surface deformation recorded by geodetic instruments represents a combination of long-term plate motions and time-dependent signals arising from earthquake processes.

Both the long-term and short-term deformations are shaped by Earth's internal structures and carry valuable information about the underlying rheological structure and state of stress. Plate motions are dominated by a viscoplastic rheology and reflect the large-scale force balance between the driving slab pull and resistance from the underlying mantle, the subduction zone plate bending and the frictional plate interface (Zhong, Gurnis, and Moresi, 1998; Conrad and Hager, 1999; Alisic et al., 2012; Behr et al., 2022; Li and Gurnis, 2023). In these regions, dislocation creep and plastic yielding lead to a nonlinear rheology plays an important role in enabling plate mobility and regulating the long-term velocity (Solomatov and Moresi, 1997; Zhong, Gurnis, and Moresi, 1998; Conrad and Hager, 1999). On shorter timescales, postseismic deformation is controlled by relocking and afterslip

on the fault as well as viscoelastic relaxation within the surrounding lithosphere and mantle (Pollitz, 1992; Marone, Scholtz, and Bilham, 1991; Perfettini and Avouac, 2004; Wang, Hu, and He, 2012). Together with elastic properties, the viscosity structure in the subduction system strongly influence the spatiotemporal variations of postseismic signals (Bedford et al., 2016; Barbot and Fialko, 2010; Puel et al., 2024; Sun, Wang, and He, 2024; Köhne, Mallick, and Simons, 2025). While the viscosity parameters are primarily constrained by laboratory experiments (Karato and Wu, 1993; Ranalli, 1995; Hirth and Kohlstedt, 2003), they can also be inferred from current plate motions (Rudi, Gurnis, and Stadler, 2022; Hu, Rudi, et al., 2024) or postseismic deformation (Hu, Bürgmann, et al., 2016; Freed et al., 2017; Marsman et al., 2025).

The same rheological properties also regulate the surface topography and vertical motions across long and short timescales. Long-wavelength topography is regulated by isostatic compensation associated with variations in crustal thickness and density structure (Artemieva and Mooney, 2001; Laske et al., 2013), as well as dynamic support from mantle flow (Hager et al., 1985; Hoggard et al., 2017). In subduction zones, slab buoyancy, basal viscous shear, plate bending and inter-plate friction together influence the topography of outer rise, trench and mountain belts on the overriding plate (Zhong and Gurnis, 1994; Lamb, 2006; Dielforder, Hetzel, and Oncken, 2020). Surface topography evolves over seismic cycles, and these transient vertical motions can reach significant amplitudes during the coseismic and postseismic periods (Ozawa et al., 2011). The regional uplift and subsidence patterns following great earthquakes provide important constraints on the ongoing viscoelatic processes within the solid Earth (Luo et al., 2025).

Building upon recent advances in cross-scale modeling approaches (Dinther et al., 2013; Sobolev and Muldashev, 2017; Yang et al., 2023; Fang, Gurnis, and Lapusta, 2024; Fang, Gurnis, and Mallick, 2025) and computational algorithms (Rudi, Malossi, et al., 2015; Rudi, Shih, and Stadler, 2020; Hu, Rudi, et al., 2024; Zheng et al., 2025), we implement a global-scale model that resolves the dynamics of background plate motions and their temporal variations following a giant earthquakes in Japan. Incorporating realistic plate geometry and thermal structure, the model spans the entire globe while achieving high resolution along plate boundaries to accurately capture localized deformation.

We also show a proof-of-concept model with a true free surface that couples plate motions, surface topography, stress field and their spatiotemporal evolution associ-

ated with great earthquakes. This implementation further advances the cross-scale modeling framework and shows potential for reconciling multi-modal observations to constrain Earth's structures.

5.2 Governing equations and rheology

Both the background and transient deformations in this system are governed by the conservation of mass and momentum under the Boussinesq approximation:

$$\nabla \cdot v = 0, \tag{5.1}$$

$$\nabla \cdot \tau - \nabla p = \mathrm{Ra} T e_r, \tag{5.2}$$

where v is velocity, p is pressure, τ is the deviatoric stress tensor, Ra is the Rayleigh number, T is temperature, and e_r is the unit vector in the radial direction.

The background mantle flow and plate motions are dominated by a viscoplastic rheology, with a constitutive relationship given by:

$$\tau = 2\eta_{vp}\dot{\varepsilon}, \tag{5.3}$$

where η_{vp} is the effective viscosity in the viscoplastic system and $\dot{\varepsilon} = \frac{1}{2}[\nabla v + (\nabla v)^T]$ is the strain rate. The viscoplastic effective viscosity η_{vp} is given by:

$$\eta_{vp} = \omega \min\left\{\eta, \frac{\tau_y}{2\dot{\varepsilon}_{II}}\right\}, \tag{5.4}$$

such that $\tau_{II} \leq \tau_y$, where ω is a location-dependent weakness factor, η is the viscosity, τ_y is the yield strength, $\dot{\varepsilon}_{II}$ is the second invariant of the strain rate tensor, and τ_{II} is the second invariant of the deviatoric stress tensor. The weakness $\omega \in (0, 1)$ along global plate interfaces and is equal to 1 otherwise. This factor represents extra weakening within plate boundaries and varies in different segments. The viscosity η depends on temperature and strain rate:

$$\eta = \min\left\{A^{-\frac{1}{n}} \dot{\epsilon}_{II}^{\frac{1-n}{n}} \exp\left(\frac{E + PV}{nRT}\right), \eta_{max}\right\}. \tag{5.5}$$

where A is a prefactor, n is the stress exponent, R is the gas constant, E is the activation energy, V is the activation volume, P is approximated by the lithostatic stress, and η_{max} is the maximum viscosity.

The coseismic and postseismic deformation involves visco-elastic-plastic processes, and the medium is approximated by the Maxwell viscoelastic material. The relationship between the deviatoric stress and strain rate is given by:

$$\tau = 2\eta_{vep}\dot{\varepsilon}_{ve}, \tag{5.6}$$

where η_{vep} is the effective viscosity in the visco-elasto-plastic system, $\dot{\varepsilon}_{ve} = \dot{\varepsilon} + \check{\tau}/(2\mu\Delta t)$, $\check{\tau}$ is the previous deviatoric stress, μ is the shear modulus, and Δt is the time step size (Moresi, Dufour, and Mühlhaus, 2002). An initial stress field is fed into $\check{\tau}$ at the beginning of visco-elasto-plastic computations, and subsequently $\check{\tau}$ is updated by taking the stress field at the previous step. The visco-elasto-plastic effective viscosity is given by:

$$\eta_{vep} = \omega \min \left\{ \eta_{ve}, \frac{\tau_y}{2(\dot{\varepsilon}_{ve})_{II}} \right\}, \tag{5.7}$$

where $\eta_{ve} = \eta\mu\Delta t/(\eta + \mu\Delta t)$ is the effective viscosity in a viscoelastic system without plastic yielding, η also follows Eq. 5.5, and $(\dot{\varepsilon}_{ve})_{II}$ is the second invariant of $\dot{\varepsilon}_{ve}$. This formulation is consistent with Eq. 5.4 for large time step sizes.

5.3 Global model of plate motions and the Tohoku-oki earthquake

The global model is computed in a spherical shell domain with a depth range from Earth's surface down to the core-mantle boundary. The governing equations 5.1 and 5.2 are solved with free-slip boundary conditions such that all the deformations are driven by internal forces. The temperature field T is adopted from Hu, Rudi, et al. (2024), which considers slab geometry from the Slab2 model (Hayes et al., 2018), half-space cooling with plate ages constrained by magnetic anomalies (Müller et al., 2008) and lower mantle structure converted from seismic tomography (Simmons et al., 2012). The values of viscosity parameters are constrained by laboratory experiments (Karato and Wu, 1993) and are listed in Table 5.1. The viscosity is highly nonlinear in the upper mantle due to dislocation creep ($n = 3.5$) and is regulated by diffusion creep in the lower mantle ($n = 1$).

Table 5.1: Viscosity parameters in the global model.

Quantity	Symbol	Unit	Upper mantle value	Lower mantle value
Exponent	n	—	3.5	1.0
Prefactor	A	$\mathrm{Pa}^{-n}\cdot\mathrm{s}^{-1}$	2.73×10^{-15}	3.33×10^{-14}
Activation energy	E	$\mathrm{kJ}\cdot\mathrm{mol}^{-1}$	540	300
Activation volume	V	$\mathrm{cm}^3\cdot\mathrm{mol}^{-1}$	6	0

We begin with computing background plate motions with the viscoplastic rheology (Eq. 5.3). The instantaneous solve is followed by short-timescale computations with the visco-elasto-plastic rheology (Eq. 5.6) and a time step size of 1 year, with the initial stress $\check{\tau}$ provided by the viscoplastic solution. The yield strength within megathrust shear zones is slightly increased to represent a critical preseismic

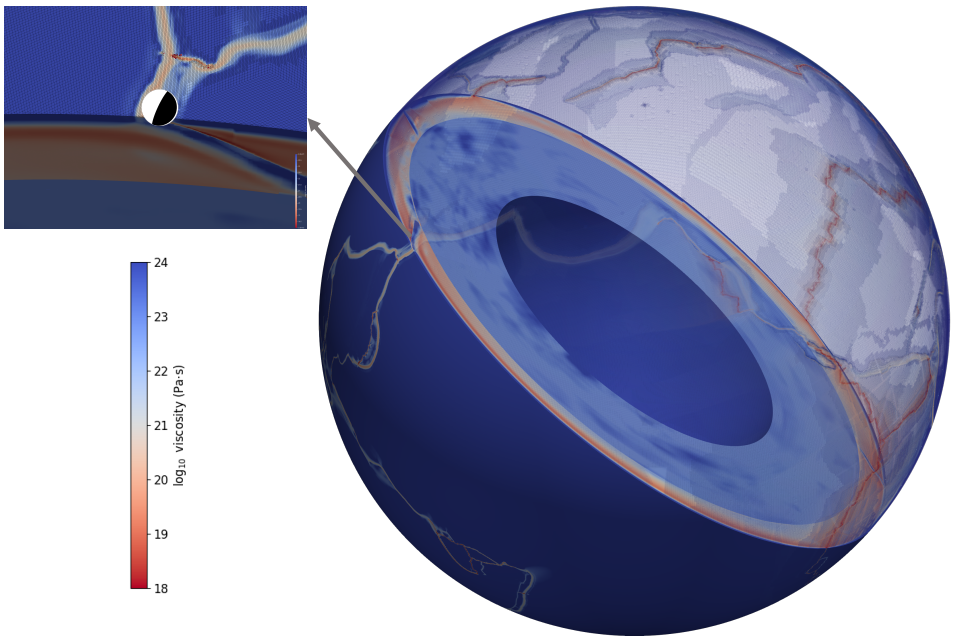

Figure 5.1: Setup of the global-scale model showing the viscosity field on cross-section through the Tohoku-oki. The inset highlights the plate boundary region resolved at a high resolution.

state. The short-timescale computations run from 2010 to 2013, and we aim to investigate the influence of the 2011 Tohoku-oki earthquake ($M_w = 9.1$). The earthquake is generated by partially reducing the yield strength within the corresponding megathrust segment, with the stress drop distribution constrained by previous studies and recorded coseismic deformation. Immediately after the earthquake, the yield strength in the ruptured zone is restored to the preseismic value, and the model naturally accounts for both afterslip within the megathrust and viscoelastic relaxation within the surrounding lithosphere and mantle. Since the deformation in the model is small compared with the minimum element size, we adopt the infinitesimal strain approximation and neglect changes in mesh geometry over time. We obtain continuous predictions of global plate motions in the 4-year period, which are jointly modulated by geodynamic underpinnings and giant earthquake perturbations.

The computations are completed using the highly scalable finite-element code *Rhea* (Rudi, Malossi, et al., 2015). The adaptive mesh refinement (AMR) dynamically adjusts mesh resolution and achieve a 1-km resolution near plate interfaces, where computational efforts are most needed. Coarser meshes are maintaned elsewhere to optimize the efficiency without compromising accuracy. The model domain contains over 30 million elements and 800 million degrees of freedom, and the

computational load is distributed across 8192 processor cores by the parallel solver. Newton's methods are employed to solve the nonlinear viscoplastic and visco-elasto-plastic problems (see Rudi, Shih, and Stadler (2020) and Text S1), which allows for faster convergence.

With a realistic thermal structure and laboratory constrained rheological parameters, the viscoplastic computation predicts long-term plate motions consistent with NNR-MORVEL56 observations (Argus, Gordon, and DeMets, 2011) (Fig. 5.2). The model reproduces key features of global plate kinematics, including the directions and magnitudes of plate velocities, which reflects a large-scale force balance modulated by the nonlinear rheology of the lithosphere and mantle. The viscosity structure (Fig. 5.1) shows agreement with estimates from other independent studies (e.g., Mitrovica and Forte (2004) and Mao and Zhong (2021)). The relative importance of resistance from the mantle flow and subduction zone plate interface varies systematically with the plate size and lead to different sensitivities of plate velocities to rheological properties. Motions of large plates, such as the Pacific Plate and Indo-Australian Plate, are dominantly controlled by the interaction of viscous mantle flow with driving forces from multiple slabs around the plate. Their large areas relative to boundary lengths allows stresses to be effectively transmitted across the plate interior and reduces the importance of strength of a single plate boundary segment. In contrast, small plates with high boundary-to-area ratios, such as the Nazca Plate and Cocos Plate, are strongly influenced by resistance distributed along their boundaries, particularly the Peru-Chile Trench and Middle America Trench respectively, and geometric constraints imposed by neighboring plates. We adjust the viscosity parameters as well as plate boundary weakness factors to fit velocities of different plates, with a focus on those related to the 2011 Tohoku-oki earthquake (M_w = 9.1).

When an M_w = 9.1 earthquake is imposed in the Tohoku-oki region, the model generates large coseismic displacements up to 50 m, with localized deformation near the epicenter and broad far-field signals transmitted over thousands of kilometers (Fig. 5.3). The coseismic response is characterized by strong opposing motions between the incoming and overriding plates that decay rapidly with the distance to the rupture zone. More gradual deformation and stress redistribution occur during the subsequent postseismic period. Postseismic deformation remains largely concentrated in near-field regions but are spatially smoother, where both afterslip on the fault and viscoelastic relaxation in the bulk contribute to the observed plate ve-

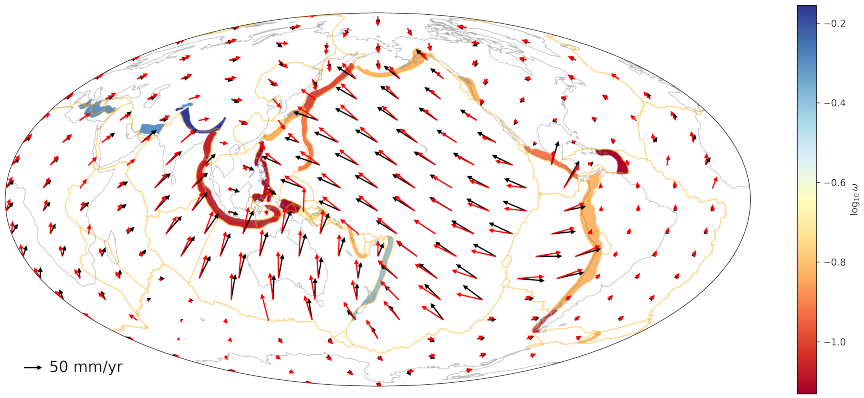

Figure 5.2: The predicted long-term plate motions (red arrows) compared with data calculated from NNR-MORVEL56 (Argus, Gordon, and DeMets, 2011). The background color represents the logarithmic weakness factors $\log_{10}\omega$ within major convergent plate boundaries.

locity variations. The regional deformation patterns show considerable consistency with geodetic records, including prominent oceanward motions across Honshu immediately onshore of the rupture zone, as well as the enhanced landward motion (ELM) emerging in Hokkaido. Additional spatial complexity arises from the along-strike variability in plate boundary geometry and its branching at triple junctions. These results highlight the structural and rheological controls that jointly shape the spatiotemporal evolution of deformation following great megathrust earthquakes.

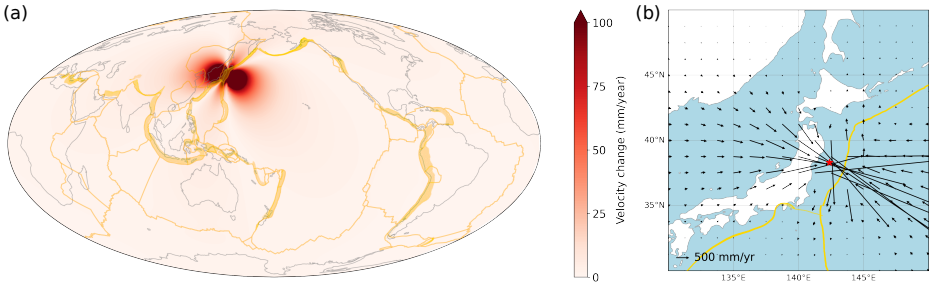

Figure 5.3: Coseismic surface velocity changes (a) across the Earth and (b) near the epicenter of the Tohoku-oki earthquake.

5.4 Proof-of-concept cross-section model with a true surface

The model domain consists of a thin box cut from a spherical shell covering a trench-normal cross-section including the entire incoming plate from ridge to trench (Fig. 5.5a). The top boundary is treated as a free surface with zero normal and shear stress, while all the other domain boundaries are free slip. The slab geometry is

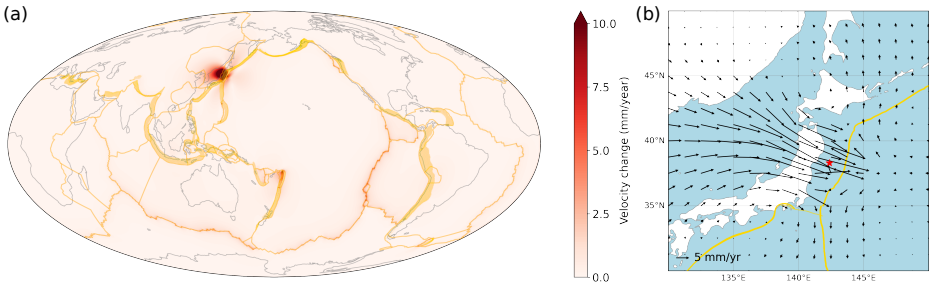

Figure 5.4: Surface velocity changes (a) across the Earth and (b) near the epicenter of the Tohoku-oki earthquake during a 1-year postseismic period.

interpolated from the Slab2 model at 36°S in the Chilean Subduction Zone.

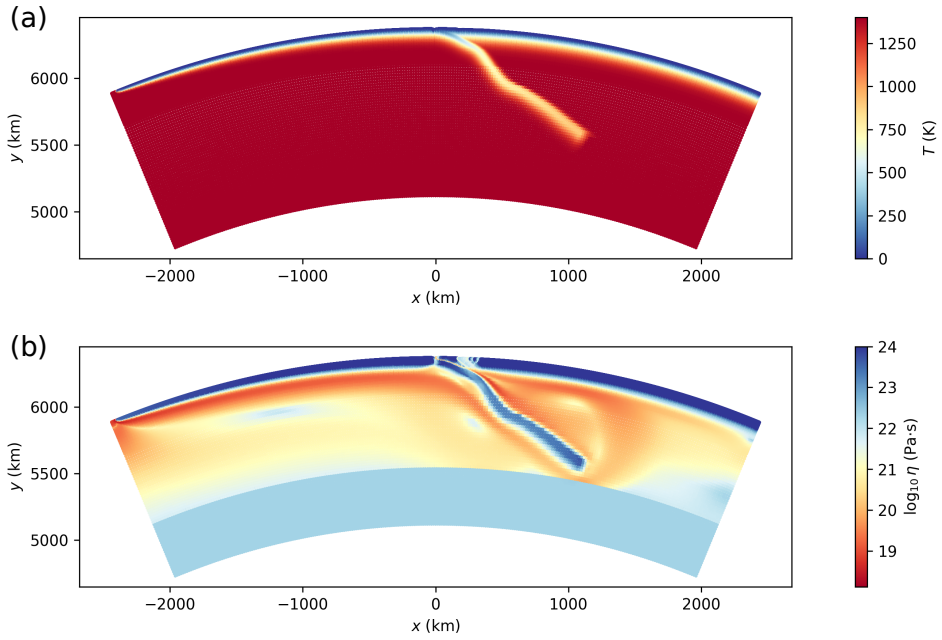

Figure 5.5: (a) Temperature (T) and (b) resulting viscosity (η) in the cross-section model.

The model is implemented and computed using the scalable finite-element code *Rhea* (Rudi, Malossi, et al., 2015). To ensure long-term vertical force balance, an additional preliminary viscoplastic solve is carried out with a free-slip top boundary to construct an initial surface topography. The resulting surface normal stresses are converted into vertical displacements, which are used to slightly deform the mesh. Subsequent computations are initialized on this updated mesh, and the workflow follows that described for the global model. An instantaneous viscoplastic solve is performed to obtain the background plate motions and stress, followed by visco-

elasto-plastic solves for their perturbations from great megathrust earthquakes. The values of viscosity parameters are listed in Table 5.2.

Table 5.2: Viscosity parameters in the global model.

Quantity	Symbol	Unit	Upper mantle value	Lower mantle value
Exponent	n	—	3.5	1.0
Prefactor	A	$\mathrm{Pa}^{-n}\cdot\mathrm{s}^{-1}$	2.73×10^{-15}	7.69×10^{-14}
Activation energy	E	$\mathrm{kJ}\cdot\mathrm{mol}^{-1}$	540	300
Activation volume	V	$\mathrm{cm}^3\cdot\mathrm{mol}^{-1}$	6.25	0

The preliminary viscoplastic solution yields a horizontal plate velocity of 3.5 cm/yr (Fig. 5.6a) and a corresponding distribution of normal stresses along the free-slip top boundary. These normal stresses are converted into surface topography shown in Fig. 5.6b. The topography gradually decreases away from the ridge due to the cooling and subsidence of the seafloor, while substantial complexities develop near the plate boundary due to the subduction process. A distinct outer rise is observed where the incoming plate bends down into the trench. Incorporating this topography into the model permits vertical force balance on the surface. When the top boundary is a free surface, vertical velocities are effectively eliminated, and the plate maintains a consistent plate velocity of 3.5 cm/year (Fig. 5.6c).

The temporal evolution of surface velocities resolved by the visco-elasto-plastic solves is shown in Fig. 5.7. Prior to the earthquake, the horizontal velocity is relatively uniform at 3–3.5 cm/yr across the incoming plate, consistent with the steady plate velocity. A slight reduction in velocity is observed near the trench, where interseismic compression leads to a local decrease of a few mm/yr and also causes weak landward motion on the overriding plate. The small vertical velocity indicates near-equilibrium conditions in the interseismic period. During the earthquake, the surface velocity field is dominated by a sharp and localized perturbation near the trench, while the vertical component shows a prominent peak corresponding to strong uplift near the trench on the overriding plate, which transitions to subsidence further inland. These rapid deformations highlight the abrupt release of elastic strain energy and are broadly consistent with observations from great megathrust earthquakes (e.g., Ozawa et al., 2011; Vigny et al., 2011). At the postseismic stage, both the incoming and overriding plates gradually slow down as the system evolves toward a new equilibrium state. However, the horizontal velocity remains higher than interseismic values over a broad region on the incoming plate, indicating the long-lasting influence of stress perturbations. The overriding plate is characterized

by opposing horizontal motions between the near-trench and inland areas and vertical motions showing alternating uplift and subsidence signals, which decay with time. Both deformation patterns resemble those observed following giant earthquakes and are commonly interpreted as signatures of postseismic viscoelastic relaxation (Sun, Wang, Iinuma, et al., 2014; Luo et al., 2025). The modeled spatiotemporal evolution of surface deformation shows the transition from localized coseismic slip to more distributed postseismic processes and demonstrates that our approach can be used to reconcile observations of plate motions, surface topography and off-megathrust stress state across seismic cycles.

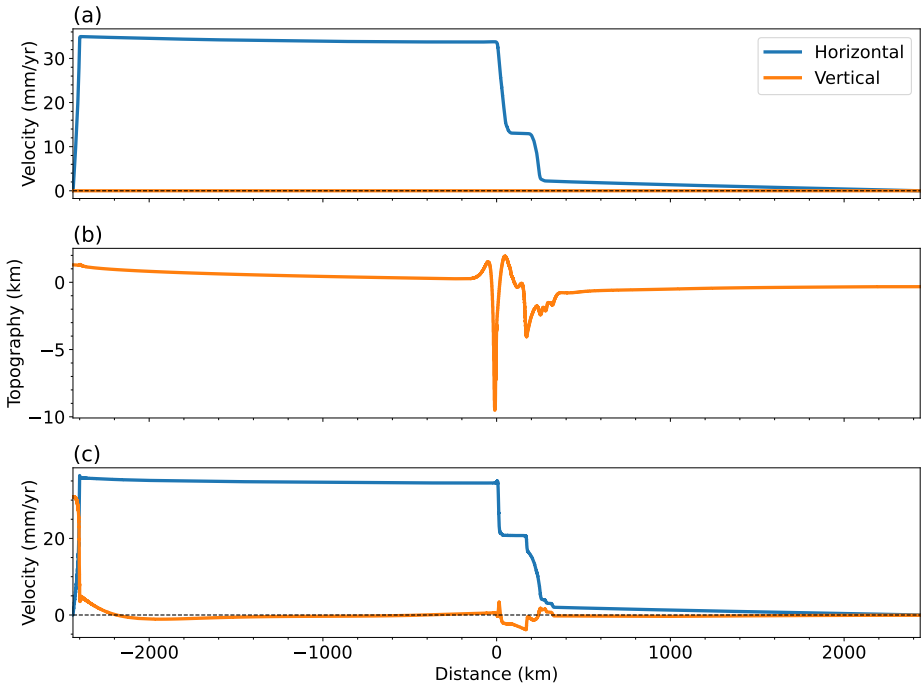

Figure 5.6: (a) Surface velocities computed by the preliminary viscoplastic solve with a free-slip top boundary. (b) The surface topography converted from normal stresses along the free-slip top boundary. (c) Surface velocities computed by the viscoplastic solve with a free surface.

Supplementary material

Newton's method for visco-elasto-plastic problems

We adapt the standard Newton's method to nonlinear systems governed by Eqs. 5.1, 5.2 and 5.6. The solver starts with an initial guess (v_0, p_0) for velocity and pressure. Given an iterate (v_{k-1}, p_{k-1}), the solver computes the Newton update $(\tilde{v}, \tilde{p})$ as the

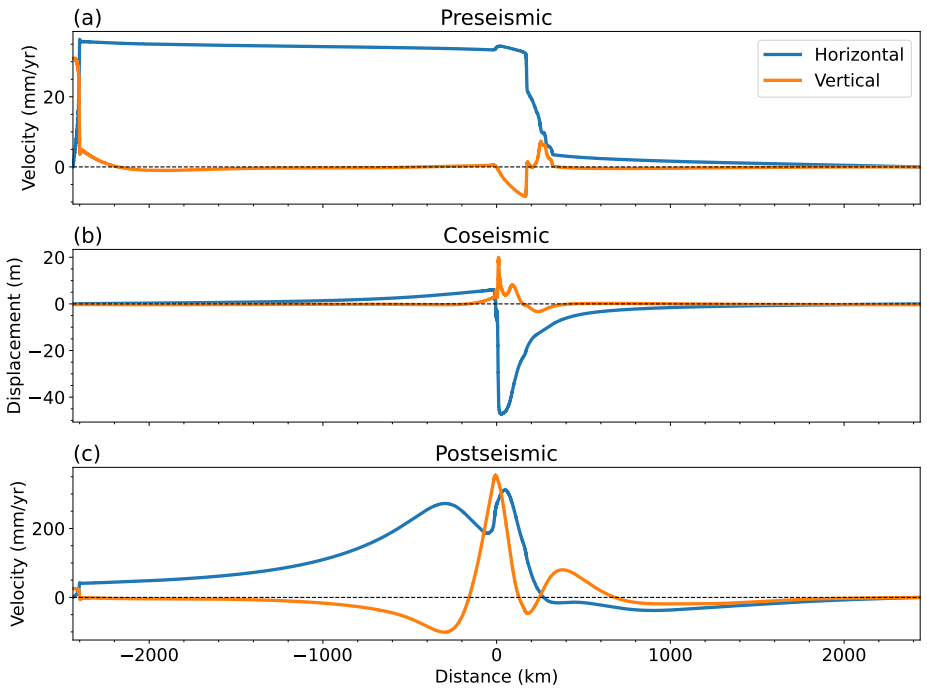

Figure 5.7: Surface velocities (a) 1 year before the earthquake, (b) during the earthquake and (c) 1 year after the earthquake.

solution to:

$$\nabla \cdot \tilde{v} = r^p_{k-1}, \tag{5.S1}$$

$$\nabla \cdot \left[2\eta_{vep} \left(\mathbb{I} - \mathcal{X}\psi \frac{\dot{\varepsilon}(v_{k-1}) \otimes \dot{\varepsilon}_{ve}(v_{k-1})}{(\dot{\varepsilon}(v_{k-1}))_{II} (\dot{\varepsilon}_{ve}(v_{k-1}))_{II}} \right) \dot{\varepsilon}(\tilde{v}) \right] - \nabla \tilde{p} = r^v_{k-1}, \tag{5.S2}$$

where $\mathcal{X}$ is the indicator function for non-yielding $\tau_{II} < \tau_y$, r^v_{k-1} and r^p_{k-1} are nonlinear residuals of the momentum (Eqs. 5.2) and mass (Eq. 5.1) conservation equations, and the coefficient ψ is given by:

$$\psi = \frac{n-1}{n} \frac{\eta_{ve}}{\eta^2} \frac{(\dot{\varepsilon}_{ve}(v_{k-1}))_{II}}{(\dot{\varepsilon}(v_{k-1}))_{II}}. \tag{5.S3}$$

Subsequently, the next iterate (v_k, p_k) is obtained with step length $\alpha \leq 1$:

$$v_k = v_{k-1} + \alpha \tilde{v}, \tag{5.S4}$$

$$p_k = p_{k-1} + \alpha \tilde{p}, \tag{5.S5}$$

and the nonlinear iteration continues until the nonlinear residual falls below the tolerance.

References

Alisic, Laura et al. (2012). "Multi-scale dynamics and rheology of mantle flow with plates". In: *Journal of Geophysical Research: Solid Earth* 117.B10.

Argus, Donald F, Richard G Gordon, and Charles DeMets (2011). "Geologically current motion of 56 plates relative to the no-net-rotation reference frame". In: *Geochemistry, Geophysics, Geosystems* 12.11.

Artemieva, Irina M and Walter D Mooney (2001). "Thermal thickness and evolution of Precambrian lithosphere: A global study". In: *Journal of Geophysical Research: Solid Earth* 106.B8, pp. 16387–16414.

Barbot, Sylvain and Yuri Fialko (2010). "A unified continuum representation of post-seismic relaxation mechanisms: semi-analytic models of afterslip, poroelastic rebound and viscoelastic flow". In: *Geophysical Journal International* 182.3, pp. 1124–1140.

Bedford, Jonathan et al. (2016). "Separating rapid relocking, afterslip, and viscoelastic relaxation: An application of the postseismic straightening method to the Maule 2010 cGPS". In: *Journal of Geophysical Research: Solid Earth* 121.10, pp. 7618–7638.

Behr, Whitney M et al. (2022). "The effects of plate interface rheology on subduction kinematics and dynamics". In: *Geophysical Journal International* 230.2, pp. 796–812.

Conrad, Clinton P and Bradford H Hager (1999). "Effects of plate bending and fault strength at subduction zones on plate dynamics". In: *Journal of Geophysical Research: Solid Earth* 104.B8, pp. 17551–17571.

DeMets, Charles, Richard G Gordon, and Donald F Argus (2010). "Geologically current plate motions". In: *Geophysical journal international* 181.1, pp. 1–80.

Dielforder, Armin, Ralf Hetzel, and Onno Oncken (2020). "Megathrust shear force controls mountain height at convergent plate margins". In: *Nature* 582.7811, pp. 225–229.

Dinther, Y van et al. (2013). "The seismic cycle at subduction thrusts: Insights from seismo-thermo-mechanical models". In: *Journal of Geophysical Research: Solid Earth* 118.12, pp. 6183–6202.

Fang, Jiaqi, Michael Gurnis, and Nadia Lapusta (2024). "Dynamic emergence of plate motions and great megathrust earthquakes across length and time scales". In: *Geophysical Research Letters* 51.22, e2024GL110821. DOI: 10.1029/2024GL110821.

Fang, Jiaqi, Michael Gurnis, and Rishav Mallick (2025). "Constraints on nonlinear mantle rheology from multi-scale geodetic observations of plate motion and post-seismic enhanced landward motion". In: *Earth and Planetary Science Letters* 669, p. 119566. DOI: 10.1016/j.epsl.2025.119566.

Freed, Andrew M et al. (2017). "Resolving depth-dependent subduction zone viscosity and afterslip from postseismic displacements following the 2011 Tohoku-oki, Japan earthquake". In: *Earth and Planetary Science Letters* 459, pp. 279–290.

Hager, Bradford H et al. (1985). "Lower mantle heterogeneity, dynamic topography and the geoid". In: *Nature* 313.6003, pp. 541–545.

Hayes, Gavin P et al. (2018). "Slab2, a comprehensive subduction zone geometry model". In: *Science* 362.6410, pp. 58–61.

Hirth, Greg and D Kohlstedt (2003). "Rheology of the upper mantle and the mantle wedge: A view from the experimentalists". In: *Geophysical monograph-american geophysical union* 138, pp. 83–106.

Hoggard, Mark J et al. (2017). "Oceanic residual depth measurements, the plate cooling model, and global dynamic topography". In: *Journal of Geophysical Research: Solid Earth* 122.3, pp. 2328–2372.

Hu, Jiashun, Johann Rudi, et al. (2024). "Constraining Earth's nonlinear mantle viscosity using plate-boundary resolving global inversions". In: *Proceedings of the National Academy of Sciences* 121.28, e2318706121.

Hu, Yan, Roland Bürgmann, et al. (2016). "Asthenosphere rheology inferred from observations of the 2012 Indian Ocean earthquake". In: *Nature* 538.7625, pp. 368–372.

Karato, Shun-ichiro and Patrick Wu (1993). "Rheology of the upper mantle: A synthesis". In: *Science* 260.5109, pp. 771–778.

Köhne, Tobias, Rishav Mallick, and Mark Simons (2025). "Probabilistic estimation of rheological properties in subduction zones using sequences of earthquakes and aseismic slip". In: *Earth, Planets and Space* 77.1, p. 3.

Kreemer, Corné, Geoffrey Blewitt, and Elliot C Klein (2014). "A geodetic plate motion and Global Strain Rate Model". In: *Geochemistry, Geophysics, Geosystems* 15.10, pp. 3849–3889.

Lamb, Simon (2006). "Shear stresses on megathrusts: Implications for mountain building behind subduction zones". In: *Journal of Geophysical Research: Solid Earth* 111.B7.

Laske, Gabi et al. (2013). "Update on CRUST1. 0—A 1-degree global model of Earth's crust". In: *Geophysical research abstracts*. Vol. 15. 15, p. 2658.

Li, Yida and Michael Gurnis (2023). "A simple force balance model of subduction initiation". In: *Geophysical Journal International* 232.1, pp. 128–146.

Luo, Haipeng et al. (2025). "Interseismic secondary zone of subsidence during earthquake cycles in subduction zones". In: *Nature Geoscience* 18.10, pp. 1027–1033.

Mao, Wei and Shijie Zhong (2021). "Constraints on mantle viscosity from intermediate-wavelength geoid anomalies in mantle convection models with plate motion history". In: *Journal of Geophysical Research: Solid Earth* 126.4, e2020JB021561.

Marone, Chris J, CH Scholtz, and Roger Bilham (1991). "On the mechanics of earthquake afterslip". In: *Journal of Geophysical Research: Solid Earth* 96.B5, pp. 8441–8452.

Marsman, CP et al. (2025). "Unraveling processes and rheology of the Tohoku earthquake cycle using bayesian inference". In: *Journal of Geophysical Research: Solid Earth* 130.5, e2024JB029665.

Mitrovica, JX and AM Forte (2004). "A new inference of mantle viscosity based upon joint inversion of convection and glacial isostatic adjustment data". In: *Earth and Planetary Science Letters* 225.1-2, pp. 177–189.

Moresi, Louis, Frédéric Dufour, and H-B Mühlhaus (2002). "Mantle convection modeling with viscoelastic/brittle lithosphere: Numerical methodology and plate tectonic modeling". In: *Pure and applied Geophysics* 159, pp. 2335–2356.

Müller, R Dietmar et al. (2008). "Age, spreading rates, and spreading asymmetry of the world's ocean crust". In: *Geochemistry, Geophysics, Geosystems* 9.4.

Ozawa, Shinzaburo et al. (2011). "Coseismic and postseismic slip of the 2011 magnitude-9 Tohoku-Oki earthquake". In: *Nature* 475.7356, pp. 373–376.

Perfettini, H and J-P Avouac (2004). "Postseismic relaxation driven by brittle creep: A possible mechanism to reconcile geodetic measurements and the decay rate of aftershocks, application to the Chi-Chi earthquake, Taiwan". In: *Journal of Geophysical Research: Solid Earth* 109.B2.

Pollitz, Fred F (1992). "Postseismic relaxation theory on the spherical earth". In: *Bulletin of the Seismological Society of America* 82.1, pp. 422–453.

Puel, Simone et al. (2024). "Volcanic arc rigidity variations illuminated by coseismic deformation of the 2011 Tohoku-oki M9". In: *Science Advances* 10.23, eadl4264.

Ranalli, Giorgio (1995). *Rheology of the Earth*. Springer Science & Business Media.

Rudi, Johann, Michael Gurnis, and Georg Stadler (2022). "Simultaneous inference of plate boundary stresses and mantle rheology using adjoints: large-scale 2-D models". In: *Geophysical Journal International* 231.1, pp. 597–614.

Rudi, Johann, A Cristiano I Malossi, et al. (2015). "An extreme-scale implicit solver for complex PDEs: Highly heterogeneous flow in earth's mantle". In: *Proceedings of the international conference for high performance computing, networking, storage and analysis*, pp. 1–12.

Rudi, Johann, Yu-hsuan Shih, and Georg Stadler (2020). "Advanced Newton methods for geodynamical models of Stokes flow with viscoplastic rheologies". In: *Geochemistry, Geophysics, Geosystems* 21.9, e2020GC009059.

Simmons, Nathan A et al. (2012). “LLNL-G3Dv3: Global P wave tomography model for improved regional and teleseismic travel time prediction”. In: *Journal of Geophysical Research: Solid Earth* 117.B10.

Sobolev, Stephan V and Iskander A Muldashev (2017). “Modeling seismic cycles of great megathrust earthquakes across the scales with focus at postseismic phase”. In: *Geochemistry, Geophysics, Geosystems* 18.12, pp. 4387–4408.

Solomatov, VS and L-N Moresi (1997). “Three regimes of mantle convection with non-Newtonian viscosity and stagnant lid convection on the terrestrial planets”. In: *Geophysical Research Letters* 24.15, pp. 1907–1910.

Sun, Tianhaozhe, Kelin Wang, and Jiangheng He (2024). “Geodetic signature of a weak lithosphere-asthenosphere boundary in postseismic deformation of large subduction earthquakes”. In: *Earth and Planetary Science Letters* 630, p. 118619.

Sun, Tianhaozhe, Kelin Wang, Takeshi Iinuma, et al. (2014). “Prevalence of viscoelastic relaxation after the 2011 Tohoku-oki earthquake”. In: *Nature* 514.7520, pp. 84–87.

Vigny, Ch et al. (2011). “The 2010 M w 8.8 Maule megathrust earthquake of central Chile, monitored by GPS”. In: *Science* 332.6036, pp. 1417–1421.

Wang, Kelin, Yan Hu, and Jiangheng He (2012). “Deformation cycles of subduction earthquakes in a viscoelastic Earth”. In: *Nature* 484.7394, pp. 327–332.

Yang, Haibin et al. (2023). “Numerical Modeling of Earthquake Cycles Based On Navier-Stokes Equations With Viscoelastic-Plasticity Rheology”. In: *Geochemistry, Geophysics, Geosystems* 24.9, e2023GC010872.

Zheng, Qunfan et al. (2025). “Ongoing India–Eurasia collision predominantly driven by Sumatra–Java slab pull”. In: *Nature Geoscience* 18.9, pp. 909–915.

Zhong, Shijie and Michael Gurnis (1994). “Controls on trench topography from dynamic models of subducted slabs”. In: *Journal of Geophysical Research: Solid Earth* 99.B8, pp. 15683–15695.

Zhong, Shijie, Michael Gurnis, and Louis Moresi (1998). “Role of faults, nonlinear rheology, and viscosity structure in generating plates from instantaneous mantle flow models”. In: *Journal of Geophysical Research: Solid Earth* 103.B7, pp. 15255–15268.

Chapter 6

CONCLUSIONS AND FUTURE OUTLOOK

This thesis presents a unified cross-scale modeling framework that bridges the length and time scale gap between plate motions, great megathrust earthquakes and their broader geophysical manifestations. The models self-consistently integrate these steady and transient processes with a nonlinear visco-elasto-plastic rheology and provide insight into their coupled dynamics. Across a suite of computational models ranging from idealized subduction systems to realistic regional and global configurations, the results highlight the intrinsic physical connection and long-lasting interaction between tectonic forces and earthquake processes. This work demonstrates the potential of advanced physics-based modeling approaches for understanding diverse geophysical observations and placing quantitative constraints on Earth's internal structures.

Chapter 2 develops a generic subduction model that simultaneously resolves long-term plate kinematics and transient deformation over megathrust seismic cycles. The emrgence of both the quasi-steady plate motions and episodic rupture events is a consequence of the interaction between tectonic forces and the nonlinear visco-elasto-plastic rheology. The reference model achieves a plate velocity of ≈ 5 cm/yr, asthenosphere viscosity of $\approx 10^{19}$ Pa·s and coseismic slip up to ≈ 10 m repeating every several hundread years. We also formulate a 2.5-dimensional approach to account for along-strike slip variations and reveal the critical role of along-strike resistance in modulating magnitudes of rupture events.

Chapter 3 systematically investigates the influence of rupture dimensions, rheological properties and subduction characteristics on the plate velocity and coseismic slip. We find that while along-strike and along-dip rupture sizes jointly control magnitudes of smaller events, the along-strike rupture length dominantly control magnitudes of the largest events as the along-dip seismogenic width is fully ruptured. The viscosity parameters mainly influence long-term plate velocities, and the elastic properties strongly influence coseismic response of the system. Megathrust friction, the incoming plate age and the seismogenic zone dip angle plays dual roles in regulating both long-term and short-term deformation behavior.

Chapter 4 applies the cross-scale modeling framework to a realistic three-dimensional

model of the Chilean Subduction Zone. With experimentally constrained dislocation creep parameters, the model successfully reproduces the long-term motion of the Nazca Plate and the postseismic deformation following the 2010 Maule earthquake (M_w = 8.8). By jointly fitting the ≈ 7 cm/yr motion of the Nazca Plate and enhanced landward motion (ELM) up to ~ 5 mm/yr, we find best-fit rheological parameters and show a pre-seismic viscosity profile that increases from 5–9 $\times 10^{18}$ Pa·s in the asthenosphere to ~ 10^{21} Pa·s close to the 660 km interface. This analysis combining multi-scale geodetic observations significantly reduces the non-uniqueness in the inferred mantle viscosity structure,

Chapter 5 shows two advanced computational models of plate motions and great earthquakes. The first half develops a margin-resolving global model of plate motions and great earthquakes based on a realistic thermal structure with the highly scalable code *Rhea* and adaptive mesh refinement (AMR). The model integrates background plate motions with transient perturbations from a great earthquakes in Japan and generates spatiotemporal patterns consistent with geodetic measurements. We demonstrate that the plate geometry and nonlinear visco-elasto-plastic rheology jointly modulate global plate motions across time scales. The second half introduces a model that incorporates a true free surface and investigates the coupled evolution of plate motions, surface topography and stress fields across seismic cycles. A proof-of-concept model is implemented to demonstrate the potential for reconciling multi-scale, multi-modal observations and advancing our understanding of their structural and rheological controls.

A key limitation of the current models is that they do not explicitly resolve the dynamic rupture processes. The computations do not fully capture the nucleation, propagation and arrest of rupture, and therefore cannot reveal the dependence of rupture extent and stress drop on the complex fault geometry and evolving stress conditions. This limitation arises primarily for two reasons. Firstly, the rupture events are represented using simplified frictional parameterizations within a quasi-static framework and inertial effects during the short timescales of earthquake rupture are ignored. Secondly, although adaptive mesh refinement enables kilometer-scale resolution in large-scale models, the effective width of the megathrust shear zone remains larger than that of natural fault zones. As a result, the models likely smooth stress concentrations and slip localization near the plate interface. In addition, the models assume an incompressible medium for the solid Earth and neglects volumetric deformation. While incompressibility is a reasonable approximation for

long-timescale deformation processes, it may influence the amplitude and spatial distribution of geodetic signals, particularly during rapid coseismic rupture.

Future work will aim to overcome these limitations and further bridge gaps between multi-scale deformations within the solid Earth. Incorporating inertia effects, adaptive timestepping, more realistic friction laws such as rate-and-state friction and compressibility will allow for modeling rupture propagation and stress transfer across seismic cycles, which is central to understanding the relationship between them and plate tectonics. Continued advances in nonlinear solvers and computational infrastructure will permit the integration of mantle flow, plate motions, dynamic rupture and seismic cycles in realistic 3D models. Another important direction is to assimilate geodetic measurements, earthquake waveforms, seismicity catalogs, stress orientations, surface topography and many other diverse geophysical observations in the model. Integrating these multi-modal, multi-scale observations within the physics-based modeling framework will ultimately improve our understanding of the slow and fast deformation processes as well as the underlying visco-elasto-plastic rheological structure that governs their coupled dynamics.